

COMSAT

Technical Review

Volume 12 Number 2, Fall 1982

Advisory Board Joseph V. Charyk
William W. Hagerty
John V. Harrington
John L. McLucas

Editorial Board Pier L. Bargellini, Chairman
Ali E. Atia
S. J. Campanella
William L. Cook
C. Dorian
H. W. Flieger
Jorge C. Fuenzalida
William J. Getsinger
R. W. Kreutel
Robert K. Kwan
James B. Potts
Akos G. Revesz
George R. Welti

Editorial Staff Daniel N. Crampton
MANAGING EDITOR
Margaret B. Jacocks
Pearl Coleman
Robert C. Heitman
Barbara J. Wassell
TECHNICAL EDITORS
Edgar Bolen
PRODUCTION
Shirley T. Cofield
CIRCULATION

COMSAT TECHNICAL REVIEW is published twice a year by Communications Satellite Corporation (COMSAT). Subscriptions, which include the two issues published within a calendar year, are: one year, \$10 U.S.; two years, \$15; three years, \$20; single copies, \$7; article reprints, \$1.50. Air mail delivery is available at an additional cost of \$10 per year. Make checks payable to COMSAT and address to Treasurer's Office, Communications Satellite Corporation, 950 L'Enfant Plaza, S.W., Washington, D.C. 20024, U.S.A.

Note that subscription prices reflect an increase, but all subscriptions already received at the previous rate will be honored without additional charge.

© COMMUNICATIONS SATELLITE CORPORATION 1982
COMSAT IS A TRADE MARK AND SERVICE MARK
OF THE COMMUNICATIONS SATELLITE CORPORATION

COMSAT TECHNICAL REVIEW

Volume 12 Number 2, Fall 1982

- 251 BEAM SCANNING IN THE OFFSET GREGORIAN ANTENNA
V. Krichevsky and D. F. DiFonzo
- 271 DEPOLARIZATION OF 19-GHZ SIGNALS **P. Kumar**
- 295 OPTIMUM ORBITAL LOCATION OF A COMMUNICATIONS SATELLITE
A. Sinha
- 319 CANCELLATION OF ACOUSTIC FEEDBACK **O. Horna**
- 335 HARDWARE SIMULATION FACILITY FOR 120-MBIT/S QPSK/TDMA SYSTEM
C. Burwell and S. Gover
- 371 EXPERIMENTAL EVALUATION OF THRESHOLD DETECTION WITH ESTIMATED SEQUENCE PERFORMANCE
D. Chakraborty and J. Kappes
- 399 CTR NOTES
4-GHZ HIGH-EFFICIENCY BROADBAND FET POWER AMPLIFIERS
S. Chou and C. Chang 399
SUMMARY OF INTELSAT VI COMMUNICATIONS PERFORMANCE SPECIFICATIONS
A. Ghais, J. Martin, D. Arnstein and M. Lewis 413
- 431 TRANSLATIONS OF ABSTRACTS
FRENCH 431 SPANISH 435



Beam scanning in the offset Gregorian antenna*

V. KRICHIEVSKY AND D. F. DIFONZO

(Manuscript received August 10, 1982)

Abstract

This paper describes analytical solutions for the constant beam direction feed loci (CBDFL) and optimum feed position locus (OFPL) for the offset Gregorian antenna. A "transmit mode" analysis is used to trace rays outward from the feed to an ellipsoidal subreflector whose rim boundary is specified at the outset. Rays are then traced to the main reflector whose rim boundary can be determined after the contributions from all feed positions have been taken into account. The intersection of the constant beam direction feed loci and optimum feed position locus defines the optimum feed positions. The canonical form of the optimum feed position locus was found to be an ellipsoid for the cases investigated.

The solutions described are in the form of analytic expressions and are therefore computationally more efficient than other methods such as matching of focal region fields or visual examination of the graphical traces of rays in the focal region. Computer analysis of beam scanning for several typical offset Gregorian configurations confirms that this method yields the best feed positions in terms of gain, pattern symmetry, and null depth. The results permit the assessment of this type of antenna for communications satellites and multiple-beam earth station applications.

*This paper is based upon work performed at COMSAT Laboratories under the sponsorship of the International Telecommunications Satellite Organization (INTELSAT).

Introduction

The optical and packaging characteristics of dual offset reflectors with multiple feeds may be preferable to those of single offset paraboloids for application as multiple-beam communications satellite and earth station antennas which require microwave optics that can produce scanned beams of high quality over a relatively large field of view. For example, the INTELSAT 4- and 6-GHz hemi-zone antennas must form multiple shaped beams over the earth's $\pm 9^\circ$ field of view as seen from geosynchronous orbit. These satellites have used the single offset paraboloid, which has evolved over the past decade from the INTELSAT IV-A 1.34-m aperture containing 34 feeds to the INTELSAT VI 3.2-m aperture containing approximately 150 feeds. For the substantially larger aperture that will be required by future systems, the single paraboloid optics may be limited by scan aberrations. Simply using longer focal lengths to compensate for these aberrations may result in large feed arrays and unwieldy geometries [1].

While the folded geometry and additional degree of freedom afforded by the subreflector may make offset dual reflectors attractive candidates for multiple-beam applications, a proper comparison of beam scanning qualities requires knowledge of the optimum feed position in the focal region to produce a beam scanned in a given direction.

This paper concerns the optimum feed locus for beam scanning in the offset Gregorian antenna. Earlier work on offset Gregorian geometries [2], [3] demonstrated that the beam scanning properties of this antenna are poorer than that of the equivalent paraboloid.

The method of analysis in this paper is similar to that employed in References 4 and 5. A "transmit mode" analysis is used to trace rays outward from a point in the focal region toward the subreflector whose rim boundary is specified at the outset of the problem. Rays are traced onward to the main reflector whose rim boundary is not specified until all relevant rays from all feed positions of interest have been taken into account. This procedure yields analytic solutions for the constant beam direction feed loci and optimum feed position locus, where the subreflector is constrained and the main reflector size may be chosen to minimize main reflector spillover. Related analyses have been performed for the offset Cassegrain antenna [2], [3].

In a separate publication, the optimum feed position has been presented using a "receive mode" analysis in which an incoming off axis plane wave is assumed to be incident on a main reflector paraboloid whose rim boundary is fixed, e.g., for a circular projected aperture. Rays

are then traced via the subreflector to the focal region [6]. In that analysis, the subreflector rim boundary is determined after all beam directions have been taken into account to minimize subreflector spillover.

Solution method

As in the case of a Cassegrain antenna, the solution consists of two steps: finding the loci of constant beam direction and finding the optimum feed position locus. The intersection of the two loci is the optimum feed position for a beam direction that is specified *a priori*.

The geometry of the Gregorian antenna configuration under investigation is shown in Figure 1. The paraboloidal main reflector and the ellipsoidal subreflector have a common focal point, F_1 . The origin of the Cartesian coordinates is located at the second focal point of the ellipsoid, F_2 . The axis of the subreflector axis makes an angle θ_3 with the z -axis of the main reflector, and the boundary of the subreflector is formed by the intersection of the ellipsoidal surface and the cone having its vertex at the origin. The cone axis forms angle θ_1 with the z -axis, and θ_2 is the half-angle of the cone. The projection of the contour of the subreflector on the

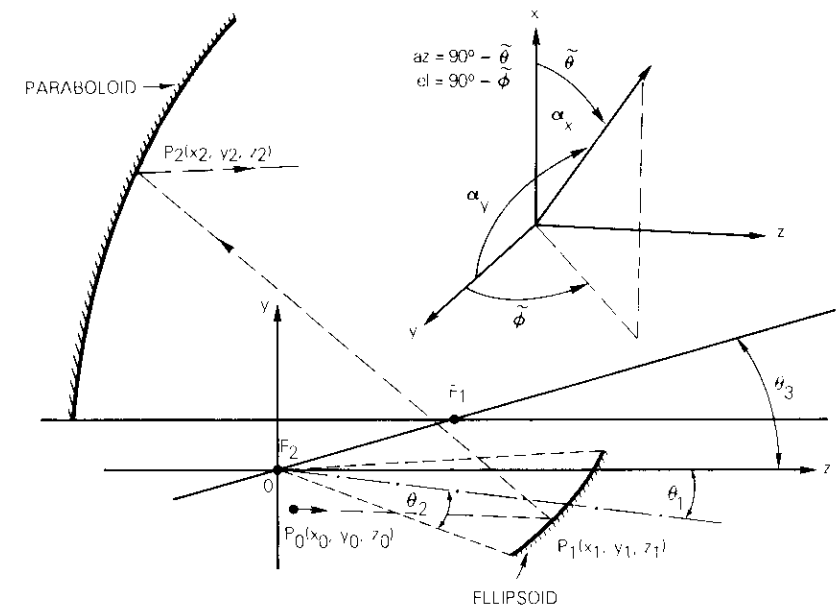


Figure 1. Antenna Geometry

xy-plane is an ellipse defined by:

$$x^2 + \xi(y - y_c)^2 = R^2 \tag{1}$$

where

$$y_c = F_i \frac{(1 - \epsilon^2)}{\epsilon} \cdot \frac{\{-\cos \theta_2 \sin|\theta_1| + \epsilon [\sin (|\theta_1| + \theta_3) \cos \theta_1 - \cos^2 \theta_2 \sin \theta_3]\}}{D_+ D_-}$$

$$\xi = \frac{D_+ D_-}{[\cos \theta_1 - \epsilon \cos \theta_2 \cos \theta_3]^2}$$

$$R^2 = \frac{F_i^2 (1 - \epsilon^2)^2 \sin^2 \theta_2}{\epsilon^2 D_+ D_-}$$

$$D_{\pm} = 1 - \epsilon \cos (|\theta_1| \pm \theta_2 + \theta_3)$$

$$\epsilon = \frac{F_i}{a}$$

F_i = half the distance between focal points of the ellipsoid

a = main ellipsoid semi-axis.

The point source is located in the vicinity of focus F_2 . The extent of the main reflector is determined at the end of the procedure by assuming that all rays reflected by the subreflector are to be intercepted by the main reflector.

Constant beam direction feed loci, first iteration

With a feed location denoted as $P_0(x_0, y_0, z_0)$, an arbitrary ray (denoted by μ) is radiated by the feed and hits the subreflector at point $P_1(x_1, y_1, z_1)$. The direction of this ray is given by the unit vector

$$\hat{S}_i = \frac{\hat{x}(x_1 - x_0) + \hat{y}(y_1 - y_0) + \hat{z}(z_1 - z_0)}{L_1} \tag{2}$$

where

$$L_1 = \sqrt{(x_1 - x_0)^2 + (y_1 - y_0)^2 + (z_1 - z_0)^2} \tag{3}$$

In accordance with Snell's law, the direction of the ray reflected by the

subreflector is defined by the unit vector

$$\hat{S}_r = \hat{S}_i - 2(\hat{S}_i \cdot \hat{N})\hat{N} \tag{4}$$

where $\hat{S}_r = \{S_{rx}, S_{ry}, S_{rz}\}$ and \hat{N} represents the unit normal to the subreflector at point P_1 . If $F(x, y, z) = 0$ is the equation of the subreflector,

$$\hat{N} = \frac{\frac{\partial F}{\partial x} \hat{x} + \frac{\partial F}{\partial y} \hat{y} + \frac{\partial F}{\partial z} \hat{z}}{\sqrt{\left(\frac{\partial F}{\partial x}\right)^2 + \left(\frac{\partial F}{\partial y}\right)^2 + \left(\frac{\partial F}{\partial z}\right)^2}} \tag{5}$$

The ray is reflected by the main surface at the point $P_2(x_2, y_2, z_2)$. The distance between P_1 and P_2 is

$$L_2 = \frac{-V_2 + \sqrt{V_2^2 - V_1 V_3}}{V_1} \tag{6}$$

where $V_1 = S_{rx}^2 + S_{ry}^2$ (7)

$$V_2 = x_1 S_{rx} + (y_1 - 2F_i \sin \theta_3) S_{ry} - 2F_p S_{rz} \tag{8}$$

$$V_3 = x_1^2 + (y_1 - 2F_i \sin \theta_3)^2 - 4F_p (F_p + z_1 - 2F_i \cos \theta_3) \tag{9}$$

F_p = focal length of the main reflector.

The unit vector \hat{G}_r along the ray reflected by the main reflector at the point $P_2(x_2, y_2, z_2)$ has components

$$G_{rx} = S_{rx} + 2\eta \frac{x_2}{\Delta_2} \tag{10}$$

$$G_{ry} = S_{ry} + 2\eta \frac{(y_2 - 2F_i \sin \theta_3)}{\Delta_2} \tag{11}$$

$$G_{rz} = S_{rz} - \frac{4\eta}{\Delta_2} F_p \tag{12}$$

where $\eta = \frac{1}{\Delta_2} \{-x_2 S_{rx} - (y_2 - 2F_i \sin \theta_3) S_{ry} + 2F_p S_{rz}\}$ (13)

$$\Delta_2 = \sqrt{x_2^2 + (y_2 - 2F_i \sin \theta_3)^2 + 4F_p^2} \tag{14}$$

$$x_2 = L_2 S_{rx} + x_1 \tag{15a}$$

$$y_2 = L_2 S_{ry} + y_1 \tag{15b}$$

$$z_2 = L_2 S_{rz} + z_1 \tag{15c}$$

After reflection on the main surface, the μ -ray direction can be rewritten in vector form as a function of the feed position, the reflection point on the subreflector, and the antenna parameters:

$$\hat{G}_r^{(\mu)} = \hat{G}_r^{(\mu)}(P_0, P_1, F_p, F_s, \varepsilon, \theta_1, \theta_2, \theta_3) \tag{16}$$

For a small feed displacement from the focus, a series expansion can be written as

$$\hat{G}_r^{(\mu)} = \sum_{k=0}^2 \sum_{n=0}^k \sum_{m=0}^{k-n} \vec{T}_{k,n,m}^{(\mu)} x_0^{k-n-m} y_0^m z_0^n \tag{17}$$

with coefficients

$$\vec{T}_{k,n,m}^{(\mu)} = C \frac{\partial^{(k)} \hat{G}_r^{(\mu)}}{\partial x_0^{(k-n-m)} \partial y_0^{(m)} \partial z_0^{(n)}} \Big|_{x_0 = y_0 = z_0 = 0} \tag{18}$$

$$\vec{T}_{k,n,m}^{(\mu)} = (T_{k,n,m}^{(x),(\mu)}, T_{k,n,m}^{(y),(\mu)}, T_{k,n,m}^{(z),(\mu)})$$

and $C = 0.5$ for $k = 2$ and $n = m = 0$ or $n = 2, m = 0$, or $n = 0, m = 2$. For all other values of indices, C equals 1.

For the optics approximation, an infinite number of rays are radiated by the point source located at an arbitrary point P_0 . After reflection on the main reflector, every ray has a different direction determined by a vector $\hat{G}_r^{(\mu)}$, and the average value of the ray directions is defined by

$$\bar{\hat{G}}_r = \lim_{l \rightarrow \infty} \left\{ \frac{1}{l} \sum_{\mu=1}^l \hat{G}_r^{(\mu)} \right\} \tag{19}$$

Note that $G_{rx}^{(\mu)}, G_{ry}^{(\mu)}, G_{rz}^{(\mu)}$ are cosine functions of the angles formed by the μ -ray with x, y, z Cartesian coordinate axes after reflection on the main reflector:

$$\left[G_{rx}^{(\mu)} \right]^2 + \left[G_{ry}^{(\mu)} \right]^2 + \left[G_{rz}^{(\mu)} \right]^2 = 1 \tag{20}$$

If the source is located at the focal point, F_2 , the rays reflected from the paraboloid have the same direction, parallel to the z -axis, *i.e.*, for any μ -ray

$$\vec{T}_{0,0,0}^{(\mu)} = \{0, 0, 1\} \tag{21}$$

Substituting the expression for $\hat{G}_r^{(\mu)}$ from equation (17) into equation (19), changing the order of summation and considering the relationship shown in equation (20), and assuming that both reflectors are symmetrical about the yz -plane yield

$$\bar{G}_{rx} = x_0(A_1 + A_2 y_0 + A_3 z_0) \equiv f_1^r(x_0, y_0, z_0) \tag{22}$$

$$\begin{aligned} \bar{G}_{ry} &= B_1 y_0 + B_2 z_0 + B_3 x_0^2 + B_4 y_0^2 + B_5 z_0^2 + B_6 y_0 z_0 \\ &\equiv f_2^r(x_0, y_0, z_0) \end{aligned} \tag{23}$$

where, for instance,

$$A_1 = \lim_{l \rightarrow \infty} \left\{ \frac{1}{l} \sum_{\mu=1}^l T_{1,0,0}^{(x),(\mu)} \right\} \tag{24}$$

For a small feed displacement from the focus, equations (22) and (23) define the beam direction as a function of the feed position. After inverting the system of equations (22) and (23), the feed position as a function of the beam direction can be obtained in an explicit form for the projections of the CBDFL on the yz - and xz -planes.

$$y_0 = y_0(z_0, \bar{G}_{rx}, \bar{G}_{ry}) \tag{25}$$

$$x_0 = x_0(z_0, \bar{G}_{rx}, \bar{G}_{ry}) \tag{26}$$

During previous calculations, the beam direction was determined by cosine functions of angles α_x and α_y between the vector-defined direction of the beam and x - and y -axes. For practical purposes, it is more common to define the beam direction by the two angles $\bar{\theta}$ and $\bar{\varphi}$, which are illustrated in Figure 1 and defined by

$$\bar{\theta} = \alpha_x, \bar{\varphi} = \cos^{-1} \left(\frac{\cos \alpha_y}{\cos \alpha_x} \right) \tag{27}$$

Optimum feed position locus

To find the optimum feed position locus, a function for minimization should be derived:

$$J = \lim_{l \rightarrow \infty} \left[\frac{1}{l} \sum_{\mu=1}^l [(G_{rx}^{(\mu)} - \bar{G}_{rx})^2 + (G_{ry}^{(\mu)} - \bar{G}_{ry})^2] \right] \quad (28)$$

J is essentially a positive function for all parameters. The coordinates of the optimum feed position should minimize the J -function and also satisfy conditions (22) and (23). Therefore, the OFPL is derived using the conditional extremum of the function:

$$T = J + \lambda[-\bar{G}_{rx} + f_1'(x_0, y_0, z_0)] + \nu[-\bar{G}_{ry} + f_2'(x_0, y_0, z_0)] \quad (29)$$

where λ, ν are Lagrangian indefinite coefficients. Taking the partial derivatives with respect to x_0, y_0, z_0 and setting them equal to zero introduces a 3-equation system with two unknown coefficients, λ and ν :

$$\begin{aligned} \frac{\partial T(x_0, y_0, z_0, \lambda, \nu)}{\partial x_0} &= 0 \\ \frac{\partial T(x_0, y_0, z_0, \lambda, \nu)}{\partial y_0} &= 0 \\ \frac{\partial T(x_0, y_0, z_0, \lambda, \nu)}{\partial z_0} &= 0 \end{aligned} \quad (30)$$

Elimination of the Lagrangian coefficients from the system of equations (30) results in an equation of the second order for the OFPL:

$$d_x x_0^2 + \sum_{m=1}^2 \sum_{k=0}^m d_{m,k} y_0^{m-k} z_0^k = 0 \quad (31)$$

where the coefficients $d_x, d_{m,k}$ are presented in Appendix A. The OFPL is symmetrical about the yz -plane and extends through the focal point.

Canonical form of the optimum feed position locus

To derive the canonical form of the OFPL, the new coordinate system x', y', z' is introduced, where the x' -axis is coincident with the x -axis and the y' - and z' -axes form an angle ψ with the y - and z -axes, respectively. The old

coordinates are expressed in terms of the new coordinates as follows:

$$\begin{aligned} x_0 &= x'_0 \\ y_0 &= z'_0 \sin \psi + y'_0 \cos \psi \\ z_0 &= z'_0 \cos \psi - y'_0 \sin \psi \end{aligned} \quad (32)$$

After equations (32) are substituted into equation (31), the value of ψ which sets the coefficient in terms of $y'_0 z'_0$ equal 0 is chosen:

$$\psi = 0.5 \tan^{-1} \left[\frac{d_{2,1}}{d_{2,2} - d_{2,0}} \right]$$

The equation of the OFPL in the new coordinate system becomes

$$\frac{x_0'^2}{Q_x} + \frac{(y'_0 - y'_{0c})^2}{Q_y} + \frac{(z'_0 - z'_{0c})^2}{Q_z} = 1$$

where

$$Q_x = \frac{Q_0}{d_x}, \quad Q_y = \frac{Q_0}{g_3}, \quad Q_z = \frac{Q_0}{g_4}$$

$$y'_{0c} = -\frac{g_1}{2g_3} z'_{0c} = -\frac{g_2}{2g_4}$$

$$Q_0 = 0.25 \left(\frac{g_1^2}{g_3} + \frac{g_2^2}{g_4} \right)$$

$$\begin{bmatrix} g_1 \\ g_2 \end{bmatrix} = \cos \psi \begin{bmatrix} d_{1,0} \\ d_{1,1} \end{bmatrix} + \sin \psi \begin{bmatrix} -d_{1,1} \\ d_{1,0} \end{bmatrix}$$

$$\begin{bmatrix} g_3 \\ g_4 \end{bmatrix} = \cos^2 \psi \begin{bmatrix} d_{2,0} \\ d_{2,2} \end{bmatrix} + \sin^2 \psi \begin{bmatrix} d_{2,2} \\ d_{2,0} \end{bmatrix} + 0.5 \sin(2\psi) \begin{bmatrix} -1 \\ 1 \end{bmatrix}$$

For all sets of parameters studied, $Q_x, Q_y,$ and Q_z were positive; therefore, it can be concluded that the OFPL is an ellipsoid.

Constant beam direction feed loci, second iteration step

In the first iteration step the CBDFL were found as a result of the series expansion of the $\bar{G}_r^{(\mu)}$ at the focal point. To obtain a more accurate definition, it is necessary to find the projection of the optimum feed position

(OFP) obtained from the first iteration step on the antenna symmetry yz -plane. Denoting that point as $a(0, \xi, \eta)$ and writing the series expansion of the $\bar{G}_r^{(n)}$ at that point yields

$$\bar{G}_{rx} = x_0(A_1^{II} + A_2^{II}y_{0\xi} + A_3^{II}z_{0\eta}) \equiv f_1^{II}(x_0, y_{0\xi}, z_{0\eta})$$

$$\begin{aligned} \bar{G}_{ry} &= B_0^{II} + B_1^{II}y_{0\xi} + B_2^{II}z_{0\eta} + B_3^{II}x_0^2 + B_4^{II}y_{0\xi}^2 + B_5^{II}z_{0\eta}^2 + B_6^{II}y_{0\xi}z_{0\eta} \\ &\equiv f_2^{II}(x_0, y_{0\xi}, z_{0\eta}) \end{aligned}$$

Then the projection of the CBDFL on the xz - and yz -plane may be written as

$$x_0^{II} = x_0^{II}(z_0 - \eta, \bar{G}_{rx}, \bar{G}_{ry})$$

$$y_0^{II} = y_0^{II}(z_0 - \eta, \bar{G}_{rx}, \bar{G}_{ry}) + \xi$$

Numerical examples

To illustrate numerically the results that have been presented in the previous sections, beam scanning in the Gregorian antenna with parameters $F_p = 60\lambda, F_p = 3F_l, \epsilon = 0.5, \theta_1 = -22.92^\circ, \theta_2 = 17.19^\circ, \theta_3 = 5.73^\circ$ will be investigated for the two cases of the beam pointing. A Potter horn with $r = 2.3\lambda$ is used as a source. The far-field is evaluated using the GAP program [7]. It should be noted that, while analytical solutions have been obtained by analyzing only phase functions, which are related to the ray directions, the GAP program includes both phase and amplitude distributions.

The first example is devoted to the case of beam scanning in the plane of antenna symmetry at $+4^\circ$ ($\tilde{\theta} = 90^\circ, \tilde{\phi} = 86^\circ$, or $az = 0^\circ, el = 4^\circ$). Figure 2 represents the CBDFLs obtained from the first and second iterations (solid lines) and the OFPL at the yz -plane (dotted line). Figure 3 illustrates the beam pointing accuracy obtained for feed locations on these CBDFL. The OFP is obtained from the CBDFL and the OFPL, and is denoted by d in Figure 2. At the OFP, when the feed is located on the CBDFL-ITER I, the beam pointing accuracy is 0.145° ; if the feed is on the CBDFL-ITER II, then the accuracy is -0.015° . For a range of $z = \pm 6\lambda$ around the OFP the worst pointing accuracy is $+0.285^\circ$ on the CBDFL-ITER I, and -0.12° on the CBDFL-ITER II. Figure 4 compares the contour plots and gains for feed positions $a-g$ on the CBDFL-ITER II (see Figure 2). As can be seen, the feed located at the extreme left point a produces the most asymmetrical beam.

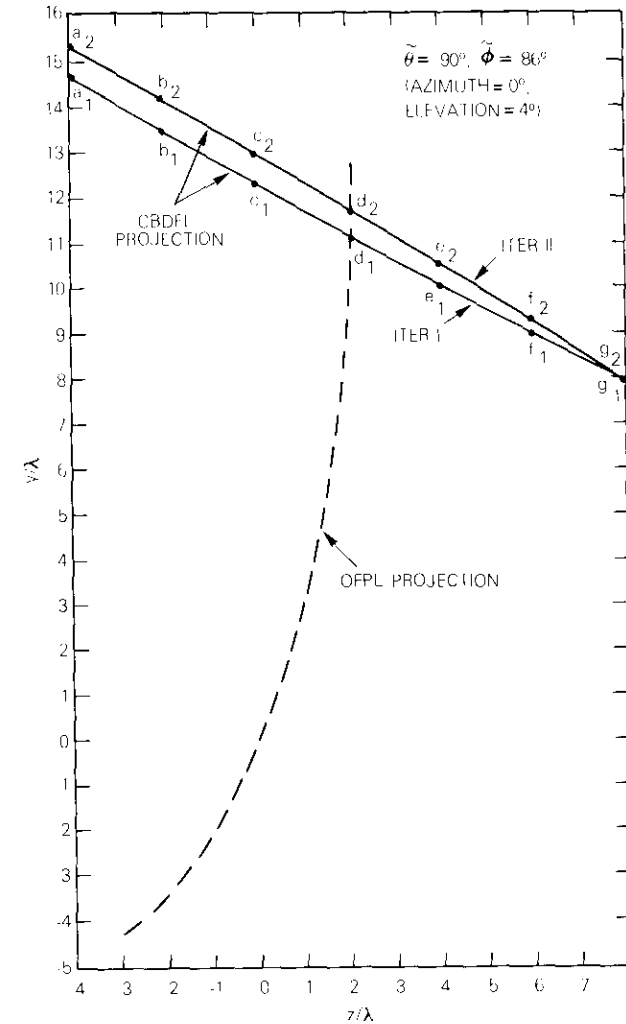


Figure 2. CBDFL After the First and Second Steps of Iteration (solid lines) and OFPL at the yz -Plane

As the feed approaches the OFP, the contour plots of the far-field become more symmetrical and the gain increases. Comparison of the contour plots and the gains for all the depicted feed positions shows that

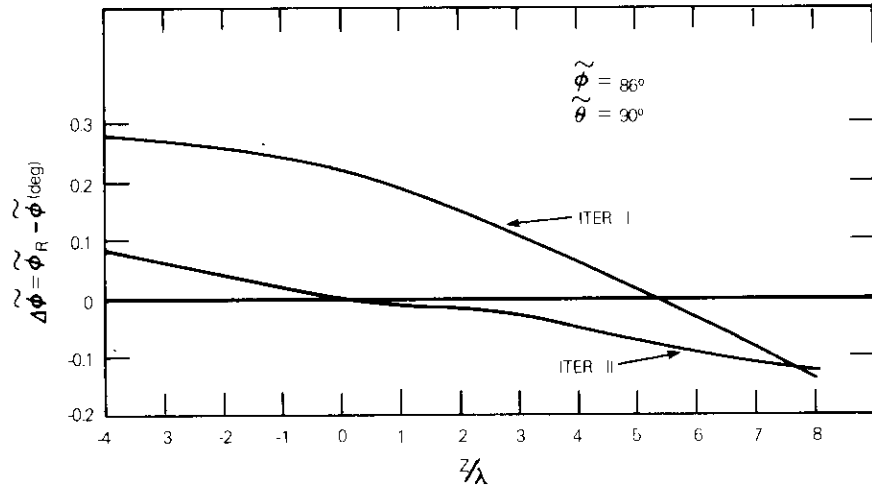


Figure 3. Beam Pointing Accuracy for the Feed on the CBDFL

the maximum gain can be achieved by locating the feed on the CBDFL at the left of the OFP, but the most symmetrical beam can be achieved by locating the feed at the right of the OFP. The feed position, e , is located on the plane that is tangential to the OFPL at the focal point F_2 .

The second example is devoted to the more general case of simultaneous scanning for $+3^\circ$ azimuth and $+3^\circ$ elevation ($\hat{\theta} = 87^\circ$ and $\hat{\phi} = 87^\circ$). Figure 5 represents the results of projecting the CBDFL projection on the yz -plane for both iteration steps (solid lines). The dotted line represents the projection of the supplemental line of intersection of the OFPL and the surface given by equation (22) on the yz -plane. The point of intersection of the solid and dotted lines gives the projection of the OFP on the yz -plane (y - and z -coordinates of the OFP). The x -coordinate of the OFP can be found from Figure 6, which gives the projection of the CBDFL on the xz -plane.

Figure 7 illustrates the beam pointing accuracy for the feed locations on the CBDFL for both iterations. $\Delta\hat{\theta}$ and $\Delta\hat{\phi}$ are the accuracies in the azimuth and elevation directions. For the parameter $Q = \sqrt{(\Delta\hat{\theta})^2 + (\Delta\hat{\phi})^2}$, the feed location at the OFP produces maximum discrepancies of 0.25° and 0.15° for the first and second iterations, respectively.

Figure 8 shows the far-field contour plots and gains for the feed locations at several positions on the CBDFL-ITER II. Once again, it can be seen that the gain increases and the contour plots become more symmetrical when the feed is moved along the CBDFL from the left to the OFP. As soon

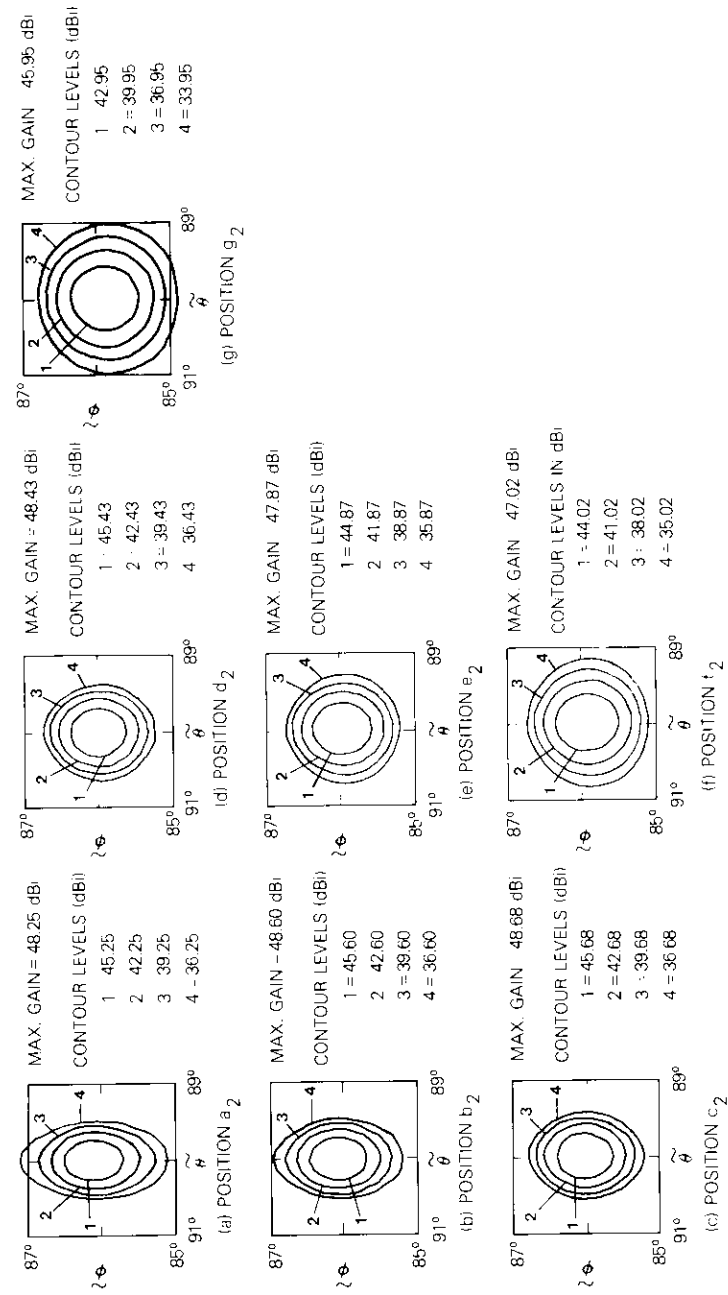


Figure 4. Comparison of the Contour Plots and Gains for the Feed Positions on the CBDFL ($\hat{\theta} = 90^\circ$, $\hat{\phi} = 86^\circ$) shown in Figure 2

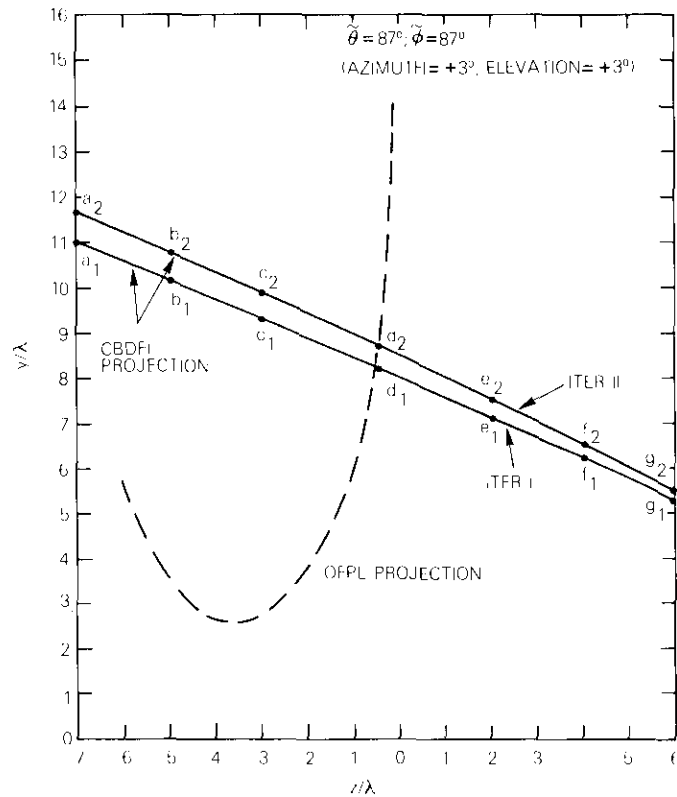


Figure 5. Projections on the yz -Plane of the CBDFL (solid lines) and of the Supplemental Line of Intersection of the OFPL and the Surface of Equation (22) (dotted line)

as the feed positions cross the OFP, the asymmetry begins to grow in the other main section of the beam. The gain is maximum to the left of the OFP. It should be noted that if the feed positions that produce the maximum gain and the most symmetrical beam do not coincide with the OFP, then they are located on the opposite sides of the OFP.

Figure 9 illustrates pattern cuts for beam scanning in the elevation plane (plane of symmetry) for an offset Gregorian antenna with $F_p = 100\lambda$, $F_l = 40\lambda$, and eccentricity of 0.5. Positive angles correspond to "upward" beam scanning as shown. As with other offset designs, the beams suffer more degradation when scanned upward than when they are scanned below the main reflector's focal axis.

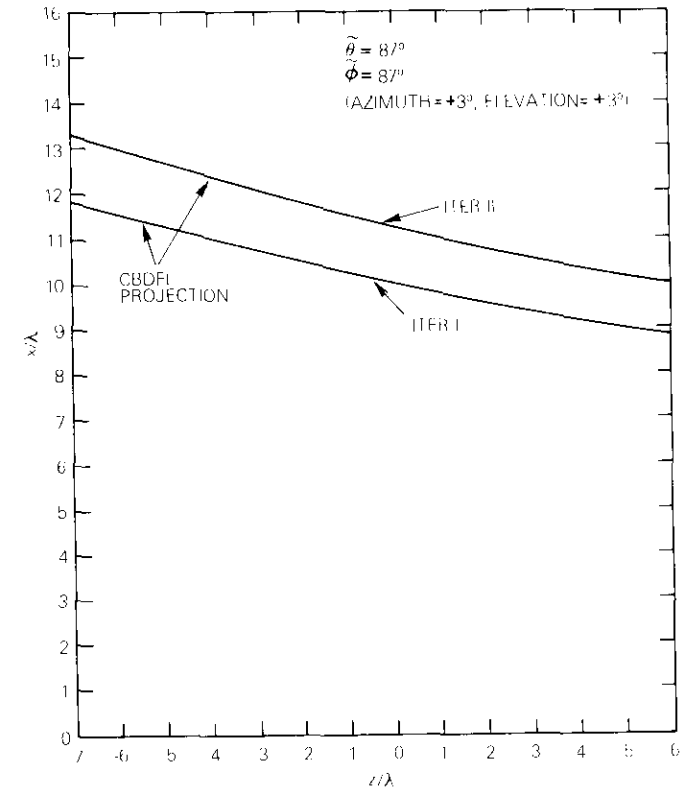


Figure 6. Projections of the CBDFL on the xz -Plane

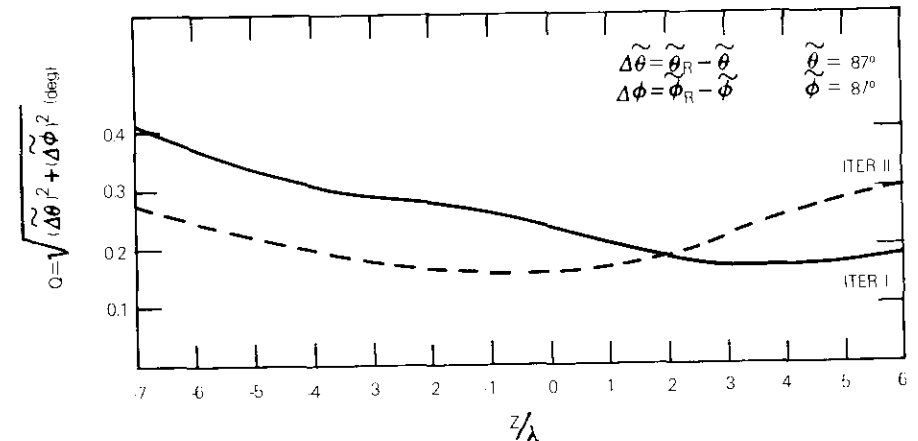


Figure 7. Beam Pointing Accuracy for the Feed on the CBDFL

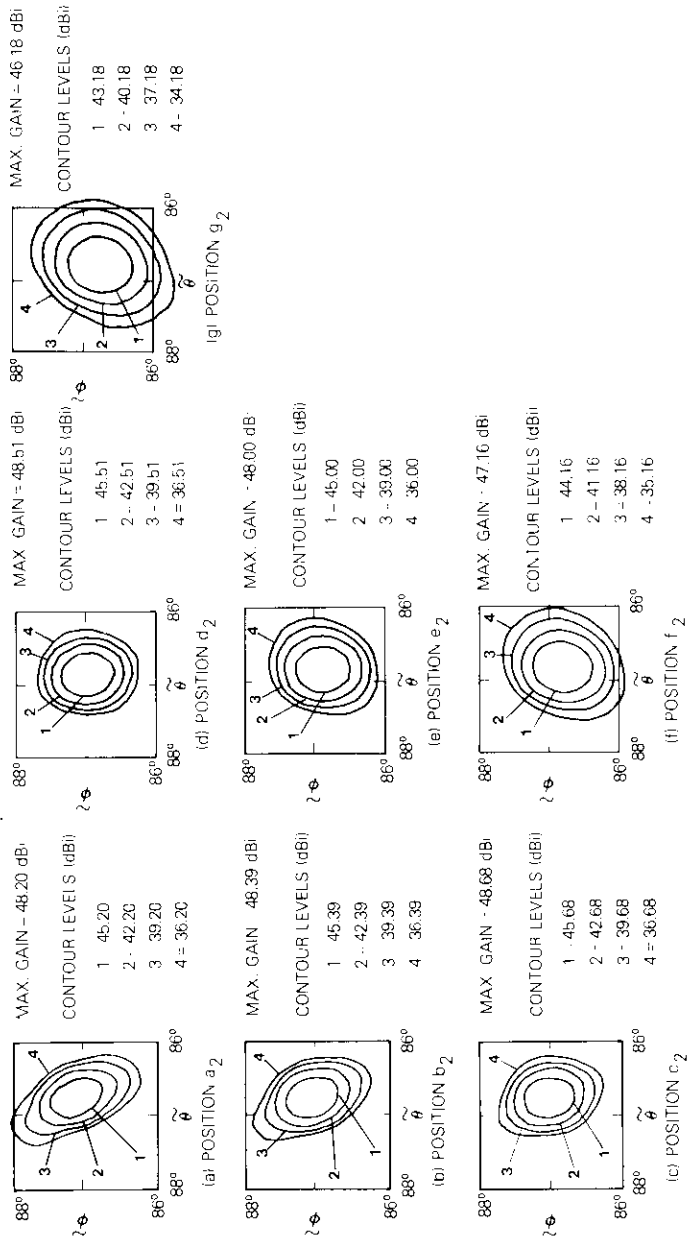


Figure 8. Comparison of the Contour Plots and Gains for the Feed Positions on the CBDFL ($\tilde{\theta} = 87^\circ, \tilde{\phi} = 87^\circ$)

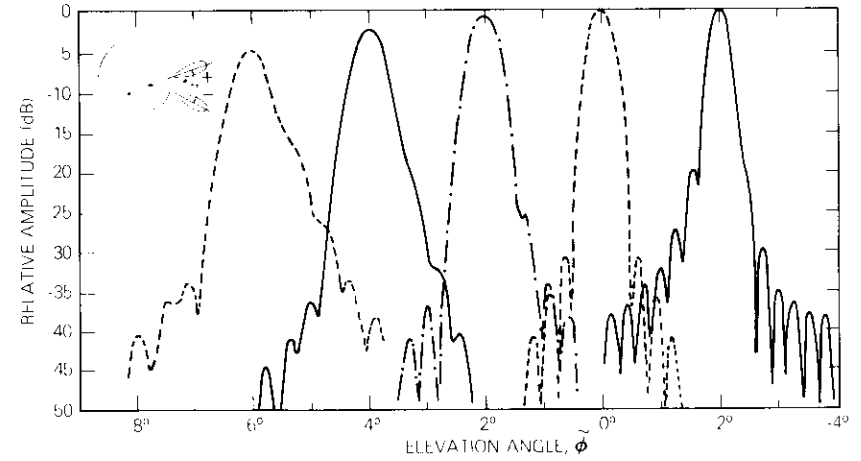


Figure 9. Pattern Cuts for Beam Scanning in the Elevation Plane

Conclusions

The CBDFL for the specific beam directions have been determined and the OFPL surface has been obtained in analytical form for the offset Gregorian antenna configuration. The optimum feed position for any specified beam direction is defined by the intersection of both loci. It was shown that, with the accuracy of the second terms of approximation, the OFPL is represented by an ellipsoidal surface. The analytical results have been demonstrated and confirmed using computer analysis of the far-field patterns. These results can be applied to the design of multi-beam and shaped beam antenna systems.

References

- [1] D. DiFonzo, "The Evolution of Communications Satellite Antennas," *IEEE Antennas and Propagation Symposium Digest*, Vol. 1, University of New Mexico, Albuquerque, New Mexico, May 24-28, 1982, pp. 358-361.
- [2] Y. Mizuguchi, M. Akagawa, and H. Yokoi, "Offset Gregorian Antenna," *Electronics and Communications in Japan*, Vol. 61-B, No. 3, 1978, pp. 58-66.
- [3] M. Akagawa and D. F. DiFonzo, "Beam Scanning Characteristics of Offset Gregorian Antennas," *AP Symposium Digest*, Vol. 1, pp. 262-265, IEEE International Symposium on Antennas and Propagation, Seattle, Washington, June 18-22, 1979.

- [4] V. Krichevsky and D. F. DiFonzo, "Optimum Feed Locus for Beam Scanning in the Symmetry Plane of Offset Cassegrain Antennas: Two-Dimensional Case," *COMSAT Technical Review*, Vol. 11, No. 1, Spring 1981, pp. 131-157.
- [5] V. Krichevsky and D. F. DiFonzo, "Optimum Feed Locus for General Three-Dimensional Beam Scanning in Offset Cassegrain Antenna," 1981 Antenna and Propagation Symposium, Los Angeles, California, June 16-19, 1981, *Digest*, Vol. 2, pp. 700-703.
- [6] V. Krichevsky, "Beam Scanning in Offset Cassegrain Antenna," Albuquerque, New Mexico, May 1982, *IEEE Antennas and Propagation Symposium Digest*, Vol. 1, pp. 257-260.
- [7] W. Cook, "A General-Purpose Antenna Analysis Program," Private Communication, January 8, 1974.

Appendix A. Coefficients for the OFPL Series

The coefficients for the OFPL series are as follows:

$$d_{1,0} = \frac{a_{0,2,0}}{a_{0,0,2}} \left[2 \frac{B_2}{B_1} - \frac{a_{0,1,1}}{a_{0,2,0}} \right]$$

$$d_{1,1} = \frac{a_{0,1,1}}{a_{0,0,2}} \cdot \frac{B_2}{B_1} - 2$$

$$d_x = \frac{a_{2,0,1}}{a_{0,0,2}} \left[\frac{B_2}{B_1} \left(\frac{a_{2,1,0}}{a_{2,0,1}} - \frac{A_2}{A_3} \right) + \left(1 - 2 \frac{a_{2,0,0}}{a_{2,0,1}} \frac{A_3}{A_1} \right) \cdot \left(\frac{A_2 B_2}{A_3 B_1} - 1 \right) \right]$$

$$d_{2,0} = \frac{a_{0,2,1}}{a_{0,0,2}} \frac{B_2}{B_1} \left[3 \frac{a_{0,3,0}}{a_{0,2,1}} - \frac{A_2}{A_3} \right] + \left(1 + \frac{A_2}{A_1} \cdot \frac{a_{0,1,1}}{a_{0,2,1}} \right) \cdot \left(\frac{A_2 B_2}{A_3 B_1} - 1 \right) \\ + \frac{a_{0,2,0}}{a_{0,0,2}} \frac{B_6}{B_1} \left[\left(2 - \frac{A_2 a_{0,1,1}}{A_3 a_{0,2,0}} \right) \cdot \left(\frac{A_2 B_2}{A_1 B_6} + 1 \right) \right] \\ + \frac{a_{0,1,1}}{a_{0,2,0}} \left(\frac{A_2}{A_3} - 2 \frac{B_4}{B_6} \right) \right]$$

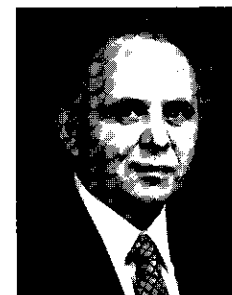
$$d_{2,1} = 2 \left[\frac{a_{0,2,1}}{a_{0,0,2}} \cdot \frac{B_2}{B_1} + \frac{a_{0,2,0}}{a_{0,0,2}} \left(\frac{A_3 B_2}{A_1 B_1} + 2 \frac{B_5}{B_1} \right) - \frac{a_{0,1,2}}{a_{0,0,2}} \right. \\ \left. - \frac{A_2}{A_1} - 2 \frac{B_4}{B_1} \right] + \frac{a_{0,1,1}}{a_{0,0,2}} \left(\frac{A_2 B_2}{A_1 B_1} - \frac{A_3}{A_1} \right)$$

$$d_{2,2} = \frac{a_{0,0,3}}{a_{0,0,2}} \cdot \frac{B_2}{B_1} \left(\frac{a_{0,1,2}}{a_{0,0,3}} - 3 \frac{A_2}{A_3} \right) + \frac{B_5}{B_1} \left(\frac{a_{0,1,1}}{a_{0,0,2}} - 2 \frac{A_2}{A_3} \right) \cdot \left(\frac{A_3 B_2}{A_1 B_5} + 2 \right) \\ + \left(3 \frac{a_{0,0,3}}{a_{0,0,2}} + 2 \frac{A_3}{A_1} \right) \left(\frac{A_2 B_2}{A_3 B_1} - 1 \right) + 2 \frac{B_6}{B_1} \left(2 \frac{A_2 B_5}{A_3 B_6} - 1 \right)$$

where A_i, B_i are coefficients in equations (22) and (23), and $a_{m,n,k}$ are given by

$$a_{m,n,k} = \frac{1}{m!n!k!} \left. \frac{\partial^{(m+n+k)} J}{\partial x_0^m \partial y_0^n \partial z_0^k} \right|_{x_0 = y_0 = z_0 = 0}$$

Vladimir Krichevsky received an M.S. and a Ph.D. in radio physics from Leningrad University and Kharkov University, USSR, respectively. Before joining COMSAT in 1978, he was with the University of Illinois, and earlier the Leningrad Institute of Communication. He is currently a member of the technical staff in the Satellite Antenna Department of the Antennas and Propagation Laboratory at COMSAT Laboratories. He is a member of the IEEE.



Daniel F. DiFonzo received a B.E.E. from Villanova University in 1962 and an M.S. from California State University in 1972. He is presently Director of the Antennas and Propagation Laboratory at COMSAT Laboratories, responsible for directing and performing research and development related to propagation studies and communications satellite and earth station antenna systems. Specifically, he has performed extensive analytical and experimental studies of techniques for the control and measurement of microwave antenna polarization properties and the design of multiple-beam spacecraft antennas. He is a member of IEEE, APS, and MTT. He was chairman of the Washington, D.C. chapter of the IEEE Antennas and Propagation Society for 1981-82.

Depolarization of 19-GHz signals

PRABHA N. KUMAR

(Manuscript received August 6, 1982)

Abstract

A knowledge of depolarization is important in the design of a frequency reuse communications system to increase the channel capacity. A quantitative measure of depolarization will assist in determining the pair of orthogonal polarizations that experience the least depolarization during rain, ice, or rain and ice depolarizing conditions. In this paper, measured rain-induced depolarization for 19-GHz vertically and horizontally polarized beacon signals from the COMSTAR satellites (D-1, D-2, and D-3) is discussed. The measured depolarization is compared with the values based on the CCIR empirical formula. Comparisons have also been made with Chu's semiempirical model, which uses a two-parameter Gaussian distribution. Then, some relevant events depicting ice depolarization are presented.

Introduction

Frequency reuse techniques will be increasingly introduced in future satellite communications systems operating at frequencies greater than 10 GHz. These systems will use two signals with orthogonal polarizations to increase the transmission capacity. Knowledge of the magnitude and occurrence of path depolarization is essential for efficient design of dual-polarized, frequency reuse communication systems. Depolarization in propagation paths is known to be caused by at least two sources [1]: hydrometeors, primarily rain and ice crystals [2]-[5]; and multipath propagation. Multipath-induced depolarization is generally limited to terrestrial links [6] and can be further induced by the cross-polarized patterns of the

receiving antenna [7]. Rain-induced depolarization and ice depolarization along earth-space paths have been considered by a number of researchers [8]–[12]. Some theoretical efforts for the prediction of rain depolarization have been published [13]–[16]. On the other hand, long-term measured data for depolarization of 19-GHz signals are not commonly found in the literature.

In this paper, measured depolarization of 19-GHz orthogonal linear polarized beacon signals from three different satellites, COMSTAR D-1, D-2, and D-3, are discussed. The results reported here reflect more than 3 years of continuous measurement. Elevation angle dependence, effects of polarization tilt angles, and year-to-year variations are important in assessing depolarization. The experimental setup for the measurement has been described in detail in previous papers [17], [18]. Table 1 [19] shows the satellite locations, elevation angles from the measurement facility at COMSAT Laboratories, and the times during which the data analyses have been conducted, along with other important parameters.

TABLE 1. CHARACTERISTICS OF COMSTAR SATELLITES^a

CHARACTERISTIC	COMSTAR SATELLITE		
	D-1	D-2	D-3
Satellite			
Locations (W. Long., deg)	128	95	87
Elevation Angle (deg)	21	41	43.5
Data Period	7/14/76–8/17/77	8/17/77–8/18/78	8/18/78–9/1/80
Polarization	Linear ^b	Linear ^b	Linear ^b
Tilt Angle (from local vertical, deg)	4	21	1.7

^aFrom Reference 19.

^bVertical and horizontal.

Definitions

The terms cross-polarization discrimination (XPD) and cross-polarization isolation (XPI) pertain to all frequency reuse communications systems. These terms are defined in different ways [1]–[3], [12], [20]; the

most commonly used terminology [1], [20] is used in this paper.

Let E_{ij} be the magnitude of the electric field of the signal at the receiver that is transmitted in polarization state i and received in polarization state j ($i, j = V, H$, where V denotes vertical polarization, and H denotes horizontal polarization). The terms E_{VV} and E_{HH} denote copolarized waves, and E_{VH} and E_{HV} refer to cross-polarized waves. XPD is the ratio (in decibels) of the power in the copolarized wave to that in the cross-polarized wave that was transmitted in the same polarization state. For vertical polarization,

$$\text{XPD}_V = 20 \log_{10} \left| \frac{E_{VV}}{E_{VH}} \right| \quad (1)$$

Similarly,

$$\text{XPD}_H = 20 \log_{10} \left| \frac{E_{HH}}{E_{HV}} \right| \quad (2)$$

for horizontal polarization.

The cross-polarization isolation, XPI, is the ratio (in decibels) of the copolarized power to the cross-polarized power that is received in the same polarization state. Symbolically,

$$\text{XPI}_V = 20 \log_{10} \left| \frac{E_{VV}}{E_{HV}} \right| \quad (3)$$

and

$$\text{XPI}_H = 20 \log_{10} \left| \frac{E_{HH}}{E_{HV}} \right| \quad (4)$$

Depolarization occurs as a result of the difference in attenuation and phase shift between the two orthogonal polarizations. Differential phase-shift is known to be the dominant factor in rain-induced cross-polarization at frequencies below 10 GHz [5], [21]. Differential attenuation becomes increasingly important for frequencies greater than 10 GHz.

Measured data

Four amplitudes (see Table 2) were measured for vertically and horizontally polarized 19.04-GHz beacon signals. Unlike other propagation experiments in which only XPD is measured, XPD and XPI for both polarizations could be determined in this experiment. Tables 3a and 3b show the link budget calculations for the 19-GHz vertically and hori-

zontally polarized signals from the COMSTAR D-2 beacons. Similar calculations for D-1 and D-3 beacons have indicated that the dynamic range of the received signals for both polarizations exceeded 35 dB. The dynamic range of the beacon receiver used in the measurement was about 35 dB for attenuation measurements.

TABLE 2. LEGENDS OF ABBREVIATIONS

ABBREVIATION	MEANING
19 TVRV	19-GHz signal transmitted in vertical polarization and received in vertical polarization (vertical, copolarized signal)
19 TVRH	19-GHz signal transmitted in vertical polarization and received in horizontal polarization (vertical, cross-polarized signal)
19 THRH	19-GHz signal transmitted in horizontal polarization and received in horizontal polarization (horizontal, copolarized signal)
19 THRV	19-GHz signal transmitted in horizontal polarization and received in vertical polarization (horizontal, cross-polarized signal)

TABLE 3A. LINK BUDGET FOR COMSTAR D-2
(19-GHz VERTICALLY POLARIZED SIGNAL)

Satellite e.i.r.p. for 19-GHz TV (measured with an antenna peak gain of 31.2 dBi) (dBW)	23.96
Measured Free Space Attenuation (clear dry day) (dB)	-209.58
Atmospheric Absorption (dB)	-0.58
Receiver Antenna Gain (dBi)	55.4
Received Signal Level (dBW)	-130.8
System Temperature T Referred to Antenna Flange (1,445 K + 290 K) (dBK)	32.4
Boltzmann's Constant, k (dBWsec/K)	-228.6
Bandwidth (100 Hz) (dB)	23.0
kTB (dBW)	-173.2
Signal C/N (dB)	42.4
Sideband Correction (dB)	3.0
Dynamic Range for Copol Amplitude Measurement (dB)	39.4

TABLE 3B. LINK BUDGET FOR COMSTAR D-2
(19-GHz HORIZONTALLY POLARIZED SIGNAL)

Satellite e.i.r.p. for 19-GHz TH (measured with an antenna peak gain of 31.15 dBi) (dBW)	26.31
Free Space Attenuation (clear dry day) (dB)	-209.58
Atmospheric Absorption (dB)	-0.58
Receiver Antenna Gain (dBi)	55.8
Received Signal Level (dBW)	-128.05
System Temperature T Referred to Antenna Flange (1,445 K + 290 K) (dBK)	32.4
Boltzmann's Constant, k (dBWsec/K)	-228.6
Bandwidth (dB)	23.0
kTB (dBW)	-173.2
Signal C/N (dB)	45.15
Sideband Correction (dB)	3.0
Dynamic Range for Copol Amplitude Measurement (dB)	42.15

Under clear sky conditions, the cross-polarized signal levels for both vertical and horizontal polarizations were about 35 dB below the copolarized signal levels. Based on these observations, a clear sky isolation of 35 dB was used in the data analyses.

Figure 1 shows the amount that the COMSTAR D-1 beacon copolarized and cross-polarized signal levels varied during rain from their respective clear sky levels, for vertical and horizontal polarizations. Figures 2 and 3 give these statistics for D-2 and D-3 beacon signals, respectively. These figures show that during rain the copolarized signal is attenuated, whereas the cross-polarized signal is enhanced. Although this increase in cross-polarized signal is significant at times (as high as 24 dB, as can be seen in Figure 1), the cross-polarized signal is generally weak relative to the copolarized signal.

There are some occasions (see Figure 2) when the cross-polarized signal increase is pronounced, even for small copolarized attenuation values. This phenomenon, called anomalous or ice crystal depolarization, is of special interest in the study of depolarization [4]-[8], [21]-[23]. A section near the end of this paper briefly describes some observed ice depolarization events.

Cross-polarization discriminations (XPDs) and cross-polarization isola-

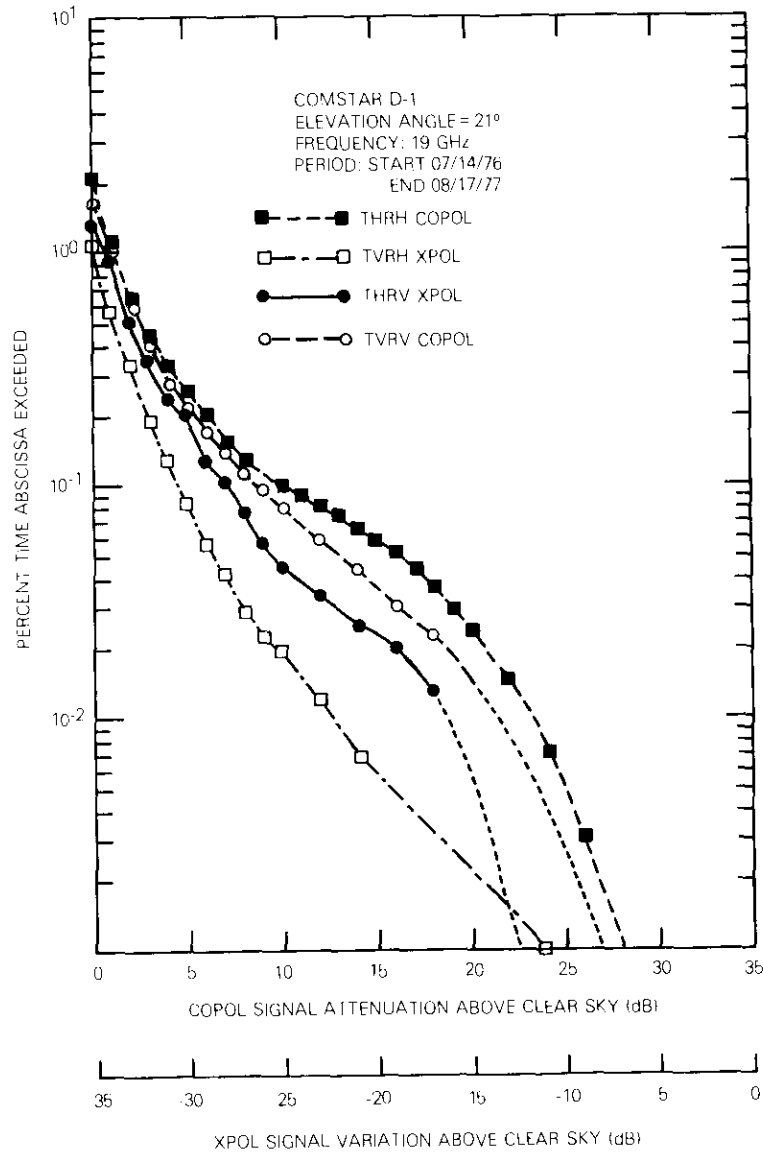


Figure 1. Cumulative Distributions of Copol and Xpol Signal Variations

tions (XPIs) are calculated for vertical and horizontal polarizations by equations (1) through (4). Figure 4 illustrates the statistical variations

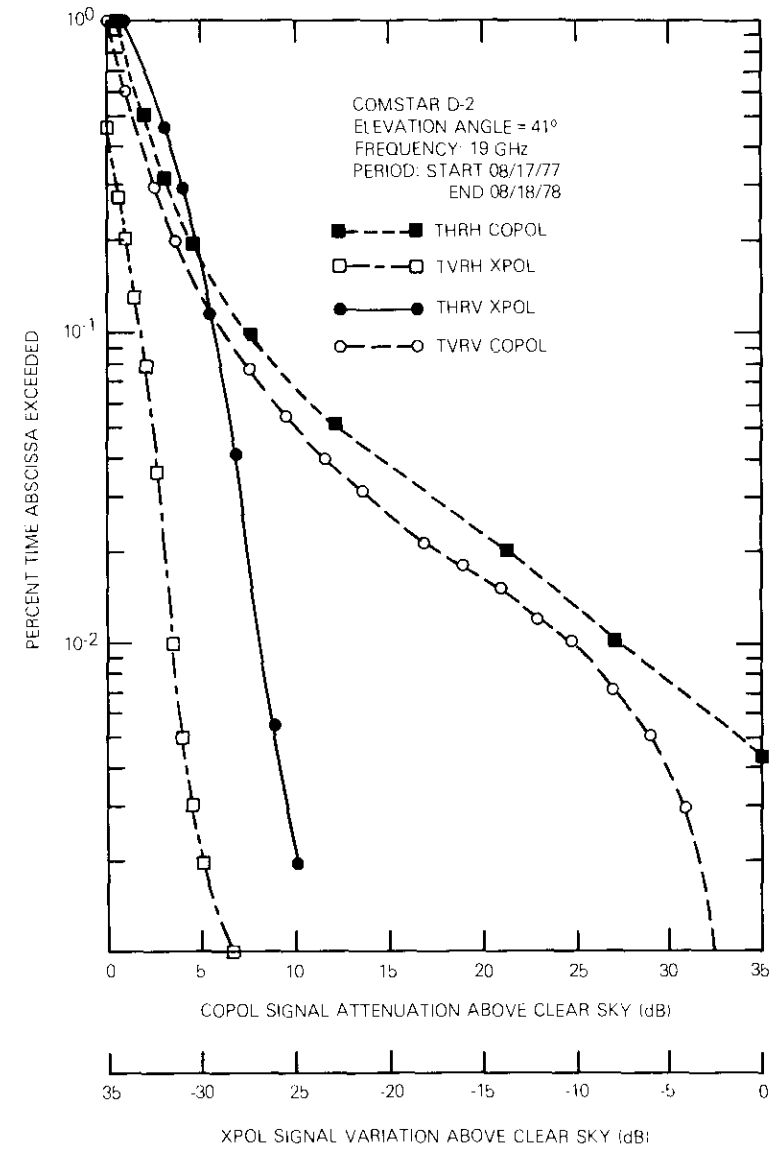


Figure 2. Cumulative Distributions of Copol and Xpol Signal Variations

of XPD_V and XPI_V . These figures show that XPD_V and XPI_V increase with increase in percentage of time and approach the clear sky isolation for the

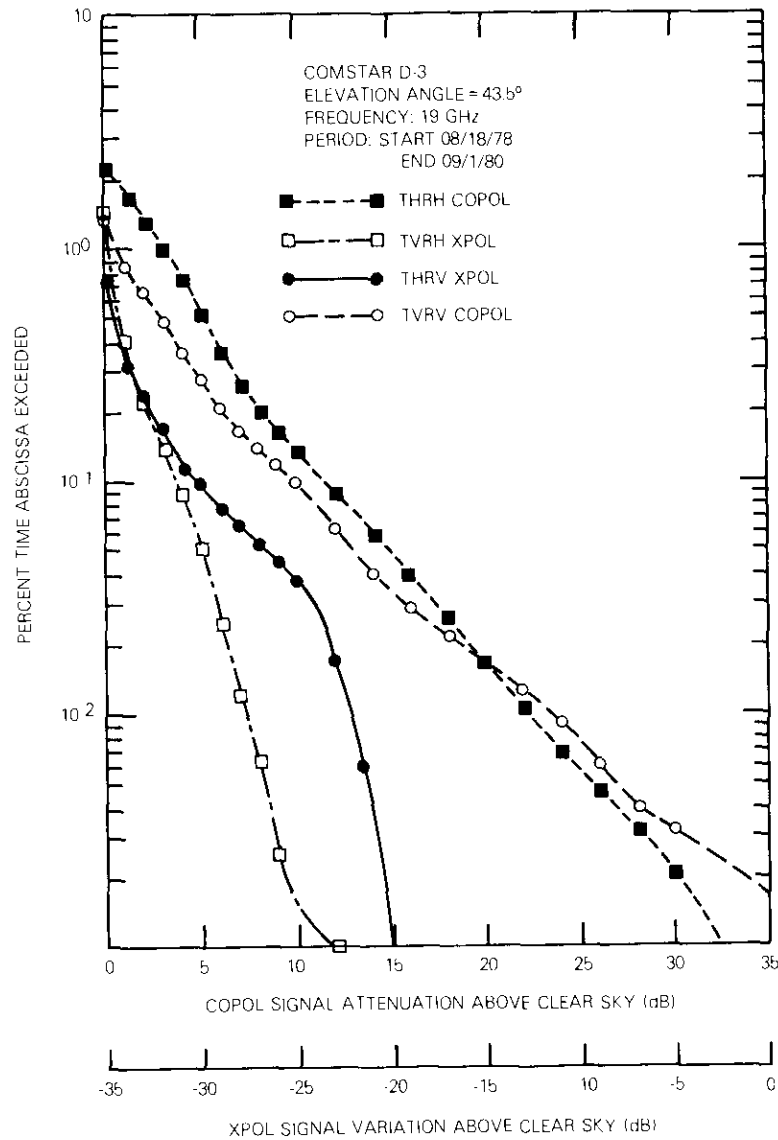


Figure 3. Cumulative Distributions of Copol and Xpol Signal Variations

largest percentage of time. In an ideal measurement for rain-induced depolarization, the curves for XPD_V and XPI_V are expected to be the same

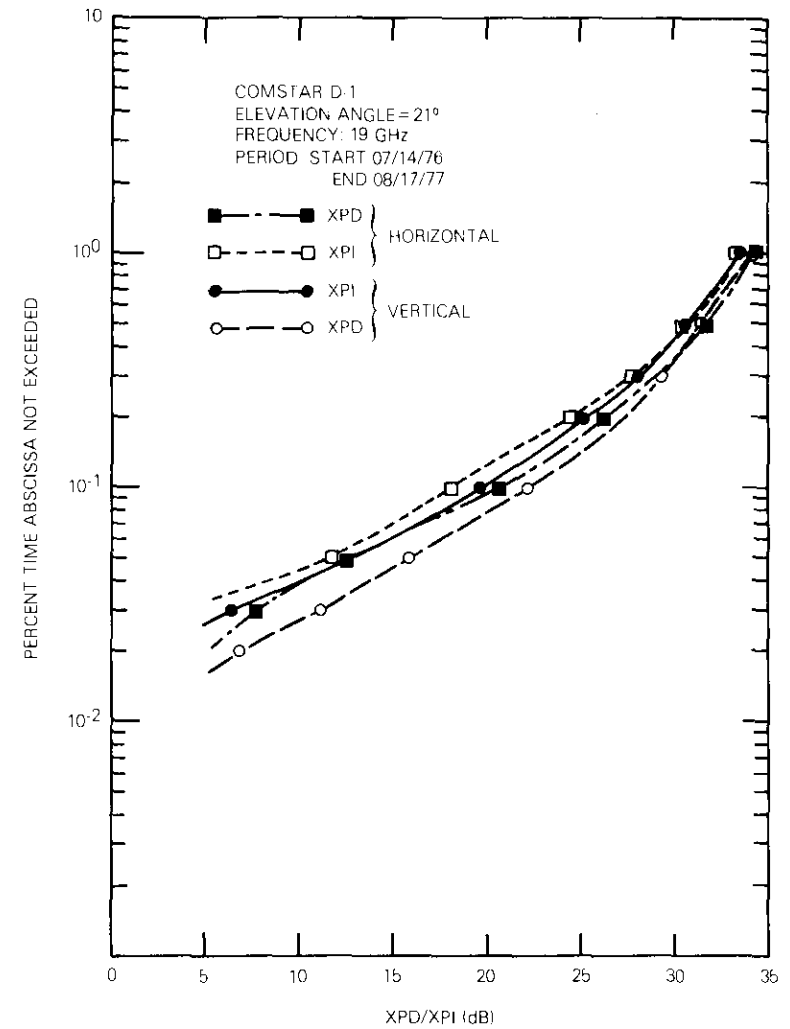


Figure 4. Cumulative Distributions of Measured XPD and XPI

[21]. However, the measured data indicate that this equality does not necessarily hold (see Figure 4). There is a difference of less than 5 dB for small percentages of time, and this difference becomes smaller for higher percentages of time. The difference can be explained by analyzing the basic concept involved in the measurement of XPD_V and XPI_V . From the definitions of these quantities, equations (1) and (3), it is

clear that XPD_V and XPI_V depend on the cross-channel interference at the two orthogonal receive antenna ports due to two mutually orthogonal polarized signals at the transmitting end. Figure 2 shows that the cross-polarized signal (E_{HV}) due to the horizontally polarized transmitted signal is weaker than the cross-polarized signal (E_{VH}) component of the vertically polarized transmitted signal. This difference may also be because the horizontally polarized signal attenuates more during rain than does the vertically polarized signal [19]. Besides the differences in attenuation, the relative phases of the two signals and the system noise may have some effects on this type of behavior. Note that the variations described have been observed consistently for all the three COMSTAR D-1, D-2, and D-3 beacon signals, as shown by Figures 5 and 6. A careful examination of these results indicates that horizontally polarized signals seem to have a slightly better isolation than vertically polarized signals. In any case, for system design considerations, it is a good idea to estimate XPI to be about 5 dB below the measured or estimated XPD values.

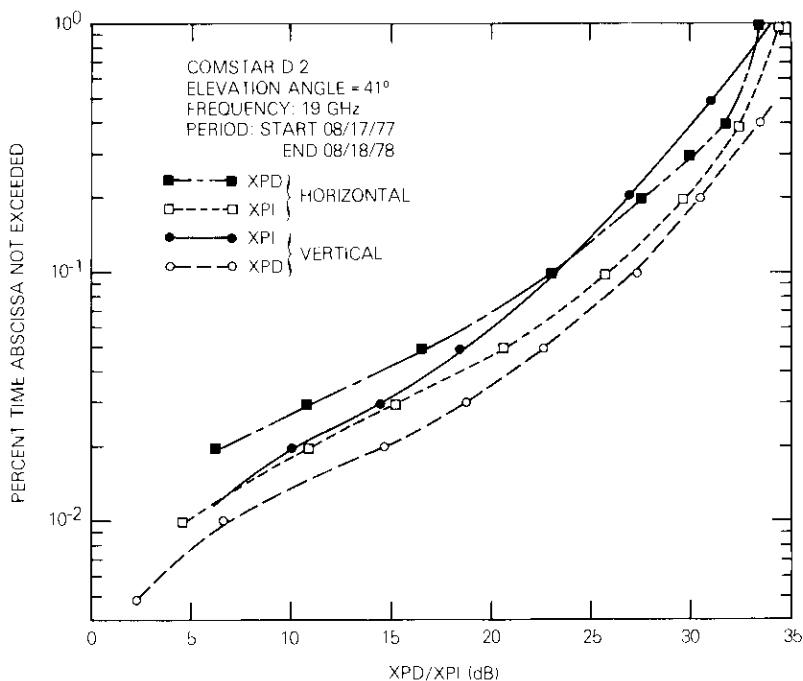


Figure 5. Cumulative Distributions of Measured XPD and XPI

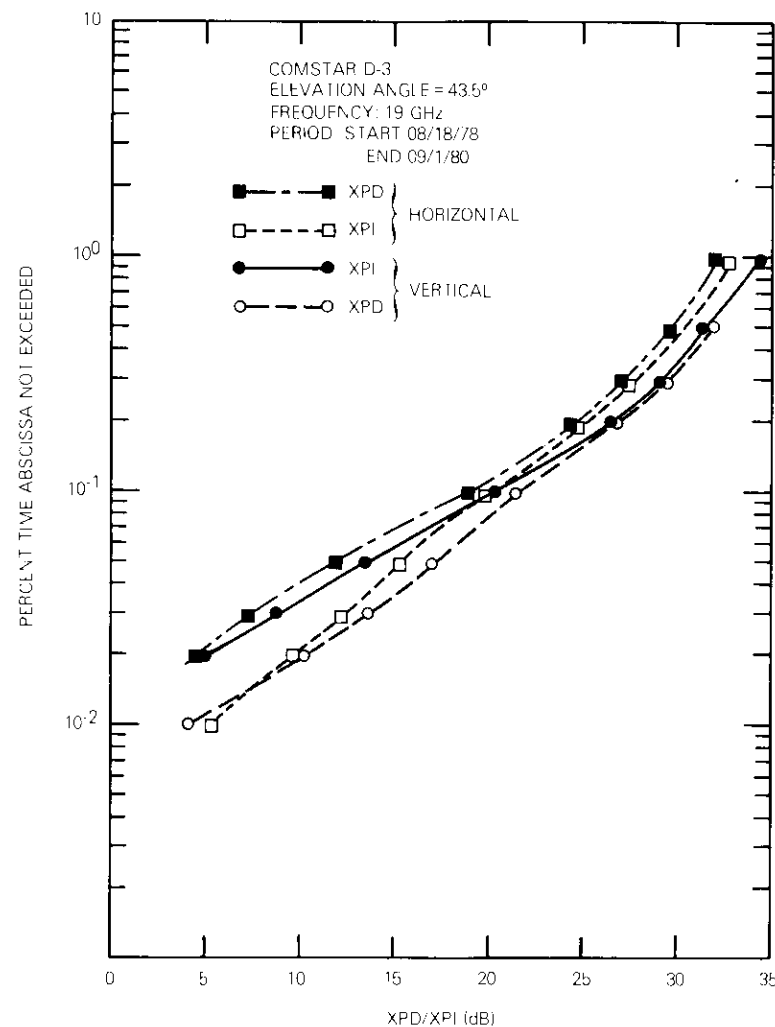


Figure 6. Cumulative Distributions of Measured XPD and XPI

Comparisons of measured XPD with theoretical models

In this section, measured XPD are compared with the theoretical values based on a CCIR approximate formula [13], [21] and another semi-empirical formula, which has recently been proposed [24].

Reference 21 recommends an approximate relation for depolarization versus attenuation given by

$$\begin{aligned} \text{XPD} = & 0.0053\sigma^2 + 30 \log_{10} f - 40 \log_{10}(\cos \epsilon) \\ & - I(\tau) - V_1 \log_{10}(\text{CPA}) \text{ (dB)} \end{aligned} \quad (5)$$

where

$$\begin{aligned} V_1 = 20 & \quad , \quad 8 \leq f \leq 15 \text{ GHz} \\ V_1 = 23 & \quad , \quad 15 \leq f \leq 35 \text{ GHz} \end{aligned}$$

and where

σ = standard deviation of effective canting angle of raindrops (deg)

τ = polarization tilt angle with respect to local horizontal (deg)

ϵ = path elevation angle (deg)

f = frequency (GHz)

CPA = copolarized signal attenuation (dB).

The factor $I(\tau)$ in equation (5) is approximately the improvement of linear polarization with respect to circular polarization. It is assumed to take two forms [21],

$$I(\tau) = -20 \log_{10}(\sin 2|\varphi - \tau|) \quad (6)$$

and

$$I(\tau) = -10 \log_{10} \left\{ \frac{1}{2} [1 - \cos(4\tau) e^{-\kappa_m^2}] \right\} \quad (7)$$

where

$$\kappa_m^2 = 0.0024\sigma_m^2$$

and φ is the mean effective canting angle of raindrops (in degrees).

In equations (5) through (7), values of σ and φ are not generally available, and for small σ_m (3° or less), assuming the observed mean canting angle is $\varphi \approx 0$, it can be easily shown that equation (7) and equation (6)

give nearly identical results [24]. Therefore, equation (5) can be approximated as

$$\begin{aligned} \text{XPD} = & 30 \log_{10} f - 20 \log_{10}(\sin 2\tau) - 40 \log_{10}(\cos \epsilon) \\ & - V_1 \log_{10}(\text{CPA}) \text{ (dB)} \end{aligned} \quad (8)$$

Figure 7 shows depolarization vs copolarized attenuation for the 19-GHz vertically polarized signal during the three data periods listed in Table 1. This figure also provides a means to compare depolarization vs attenuation for three different elevation angles.

The measured XPD for elevation angle 41° is in good agreement with the theoretical result for copolarized attenuation less than about 20 dB. For other elevation angles, the model predicts less depolarization (higher XPD) for all copolarized attenuation. This discrepancy may be attributed to several factors, such as the accuracy in measuring polarization tilt angle, the effect of canting angle of raindrops, and the calibration errors in determining clear sky isolation. Further, it should be noted that the model is only an approximation.

A few attempts have been made to revise the frequency dependence and raindrop canting angle distribution [24], [25]. A semiempirical formula suggested in Reference 24 uses a frequency-dependence term of $20 \log f$ instead of $30 \log f$. For this approximation, the first term in equation (5) is combined with other terms that account for differential attenuation and differential phase shifts, and the resulting term is treated as a parameter, $(\text{XPD})_0$, that is taken to be constant for a particular rain climate region. The term $(\text{XPD})_0$ is estimated to be approximately 11.5 dB [24] for the Northeastern United States. The semiempirical formula [24] for small σ_m reduces to

$$\begin{aligned} \text{XPD} = & (\text{XPD})_0 + 20 \log_{10} f - 20 \log_{10}(\sin 2\tau) \\ & - 40 \log_{10}(\cos \epsilon) - 20 \log_{10} A \pm \frac{\Delta A}{2} \end{aligned} \quad (9)$$

where ΔA is the differential attenuation correction term between vertical and horizontal polarizations and is approximated by

$$\Delta A = 0.15A \cos^2 \epsilon \cos 2\tau \quad (10)$$

With $(\text{XPD})_0$ taken to be 11.5 dB, the XPD values resulting from equation

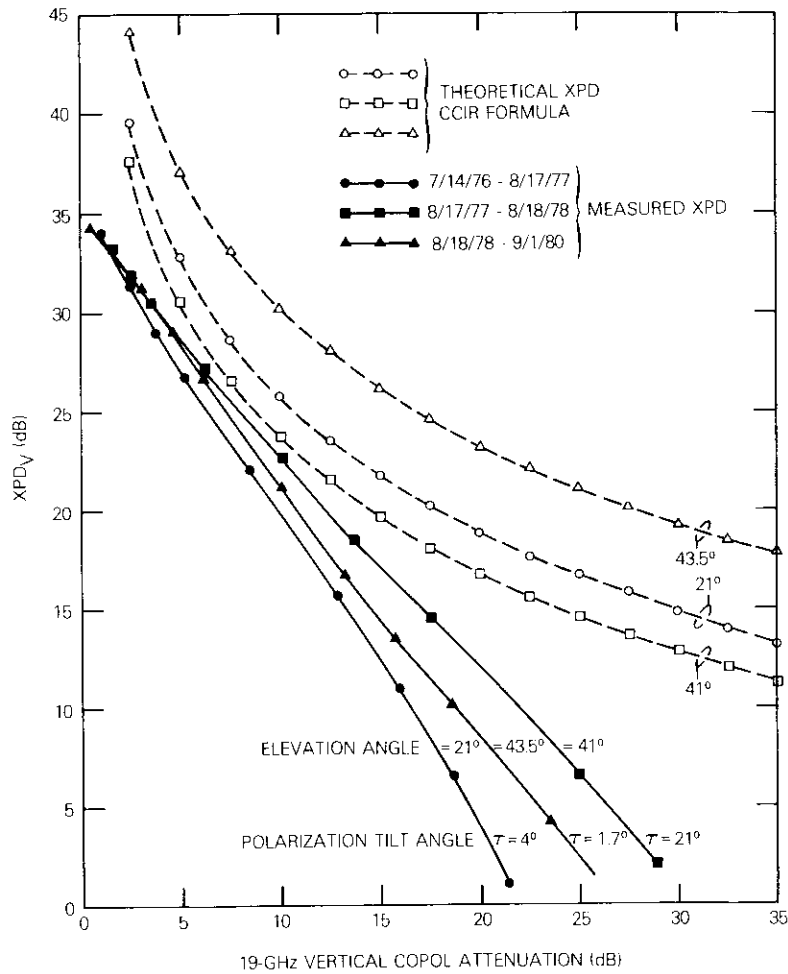


Figure 7. Comparisons of Measured XPD with CCIR-Predicted Result for Varying Elevation Angles

(9) are plotted with the measured results in Figure 8. As Figure 8 shows, this model [24] also predicts higher xpd for higher attenuation values. However, the measured xpd for COMSTAR D-2 beacon signal (with elevation angle of 41°) are still in good agreement with the model for attenuations up to 15 to 20 dB. It is suspected that other hydrometeors such as ice particles or snow are responsible for the depolarization of the COMSTAR

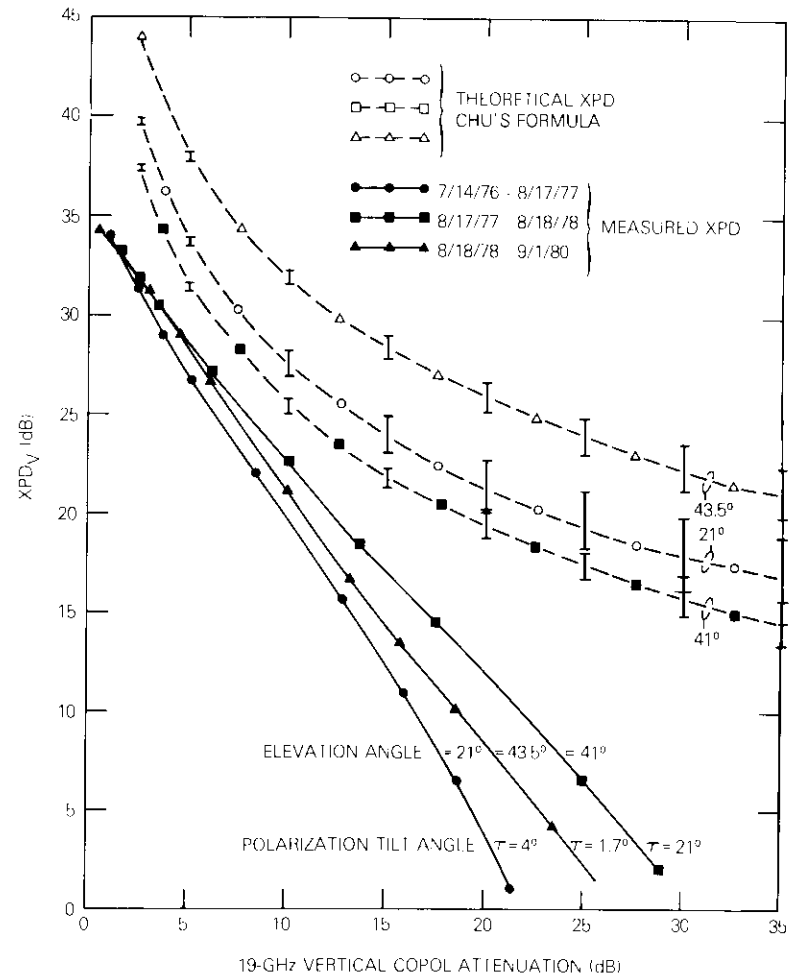


Figure 8. Comparisons of Measured XPD with Chu's Empirical Result [24] for Varying Elevation Angles

D-3 beacon signal (elevation angle of 43.5°) being slightly higher (less than 3 dB) than that for the D-2 beacon signals (elevation angle of 41°).

In Figure 9, measured xpd is compared with data measured by Bell Laboratories [3] for the median depolarization level of the 19-GHz vertically polarized signal. Note that the two measured results show almost identical depolarization for copolarized signal attenuation less than 15 dB.

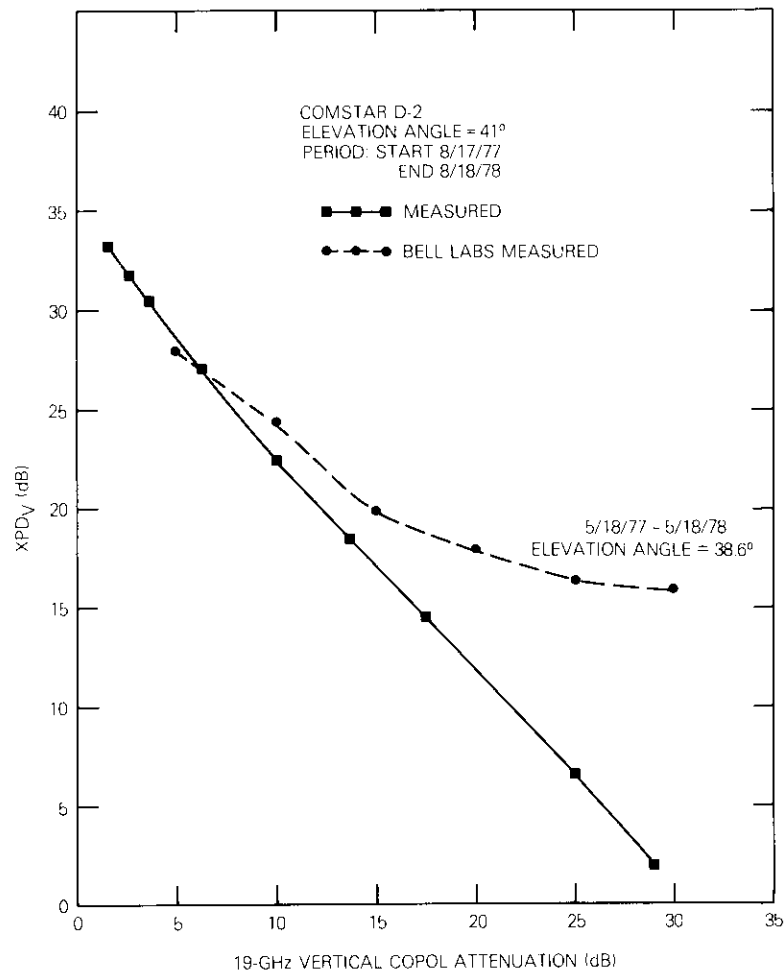


Figure 9. Comparison of Measured XPD with Bell Laboratories Data [3]

For higher attenuation, COMSAT Laboratories' measurements of XPD are much less than Bell Laboratories'. The difference in the measurements may be attributed to the difference in the rain structure between the two geographical locations of the measurements, the difference in the slant path elevation angles, and the measurement periods being nonidentical.

Ice Depolarization Events

Depolarization due to ice crystals is generally characterized by a significant increase in the cross-polarized signal level accompanied by a small (<5 dB) copolarization signal attenuation [4], [9], [22], [23], [26]. An example of such depolarization observed for the 19-GHz beacon signal is shown in Figures 10a and 10b. Figure 10a shows the signal variation for 19-GHz cross-polarized (19 THRV) and copolarized (19 TVRV) components, and Figure 10b shows the signal variation for their counterparts in horizontal polarization (19 TVRH and 19 THRH). Both of these figures represent the actual data recorded on September 27, 1977, between 2000 and 2120 GMT.

Note that the depolarization event first begins in the vertical channel and then 13 minutes later starts in the horizontal polarization. The copolarized signal attenuation for both vertical (19 TVRV) and horizontal (19 THRH) polarization is less than 2 dB. The cross-polarized signals (19 TVRH, 19 THRV) vary by ± 5 to ± 10 dB from their respective clear sky

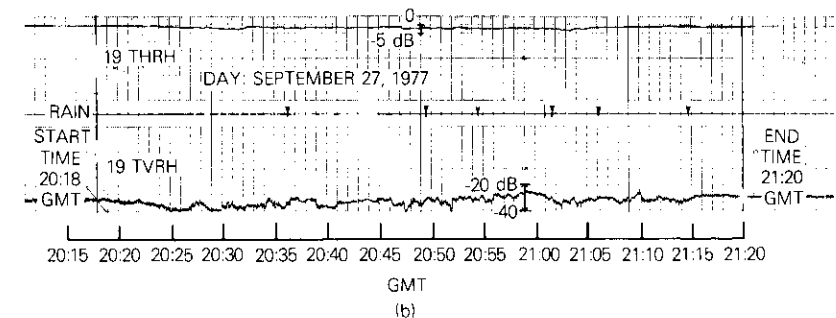
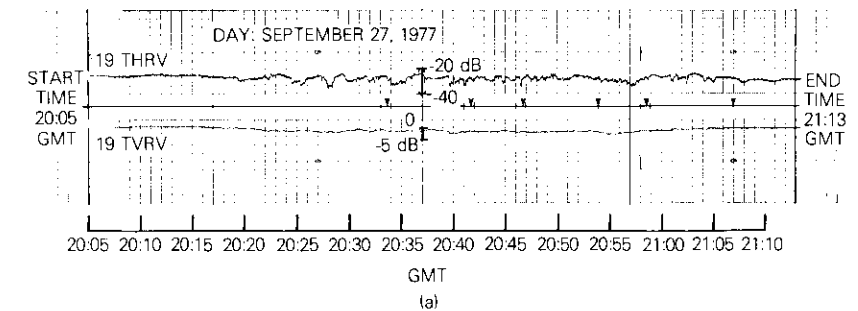


Figure 10. Ice Depolarization Event Recorded on September 27, 1977

levels (nominal levels of -35 dB). The physical phenomenon causing such a variation in cross-polarized signals, accompanied by a negligible copolarized signal attenuation, is differential phase shift due to ice particles along the propagation path [4], [17], [26], [27].

Figure 11 shows the longest depolarization event (which lasted more than 3 hours), recorded on December 9, 1977. This event was similar in its characteristics to the event before, except that the clear sky isolation (shown by the unperturbed part of the trace) did not shift considerably (<2 dB) either at the beginning or at the end of the event.

The depolarization event might have been caused by both ice and rain along the propagation path. A careful analysis of this event shows that during the first 1 hour and 30 minutes of the time involved, the cross-polarized signal (19 THRV) level had a tendency to vary -5 to -7 dB (more dips) from its clear sky isolation. During the next 1 hour and 15 minutes, the cross-polarized signal level seems to increase by about 2-5 dB. For the remaining time of duration of the event, the cross-polarized signal level appears to oscillate around the clear sky isolation and finally attain the clear sky value. Note that during this 3- to 4-hour period, there was only a light rain (which could have been mixed with snow), represented by sporadic rain ticks in Figure 11. There is no significant attenuation (<2 dB) in the copolarized signal.

Figure 12 shows another example of an ice depolarization event, recorded on April 6, 1978. This event is short compared to earlier events. Here is another example of ice depolarization when there was a very light rain and the cross-polarized signal level varied by ± 5 dB. The clear sky isolation is shifted by about $+7$ dB before the event and for about 5 minutes after the event. These three examples indicate that the ice depolarization can occur during any season of the year and is not generally restricted to summer and winter months [27].

Conclusions

This experiment is one of the few in which both the cross-polarization isolation (XPI) and the cross-polarization discrimination (XPD) are measured for both vertically and horizontally polarized 19-GHz beacon signals. The measured data have indicated that XPD_V for the vertically polarized transmitted signal is slightly better (by 2-5 dB) than XPI_V for higher rain rates; whereas, for the horizontally polarized transmitted signal XPI_H is about 2-5 dB better than XPD_H for higher rain rates. It can be argued that the system noise in the receiver may be the cause for this effect, because it is difficult to exactly match the amount of noise in the

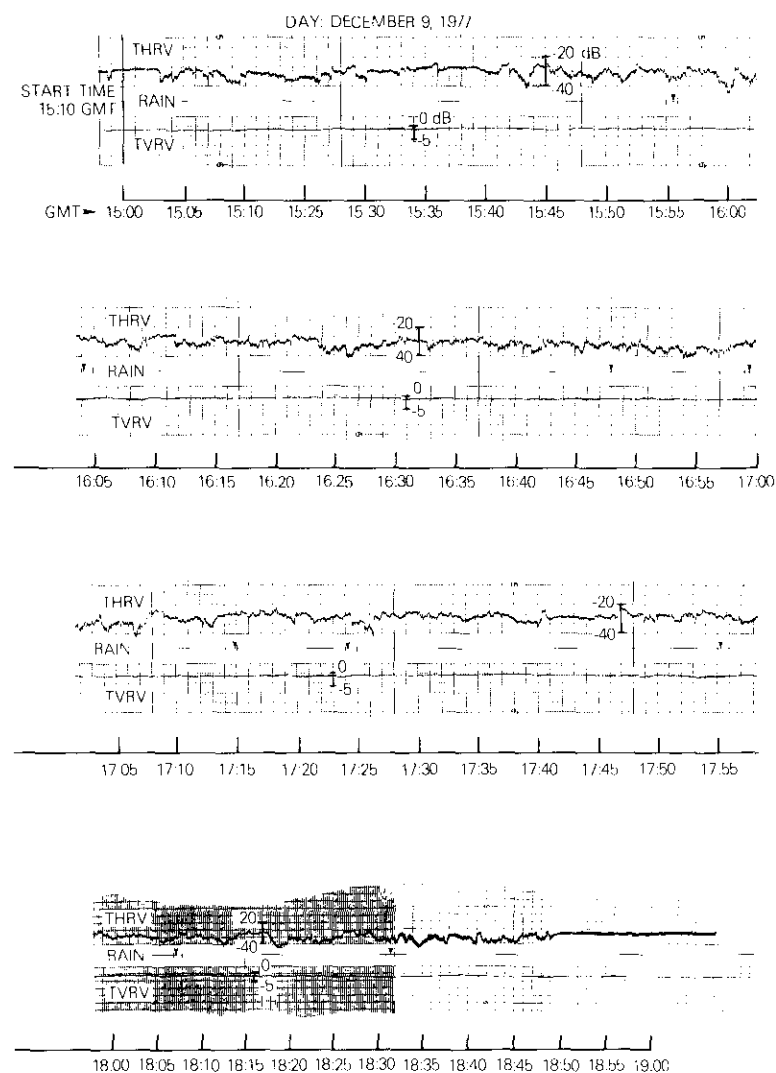


Figure 11. Ice Depolarization Event Recorded on December 9, 1977

two channels. However, the measured data have consistently shown this effect during four years. Thus, it is suspected that this effect is related to the anisotropy of the medium.

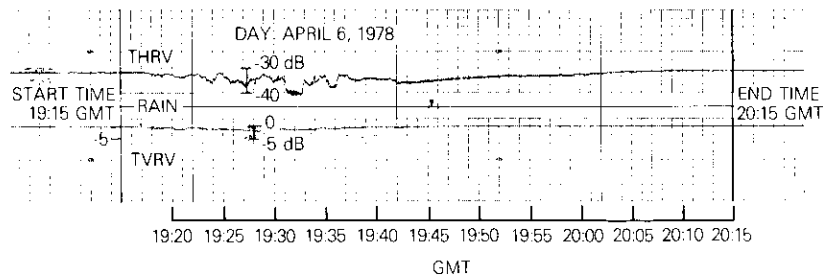


Figure 12. Ice Depolarization Event Recorded on April 6, 1978

For instance, the copolarized component (19 THR) of the horizontally polarized transmitted signal has shown greater (about 2 dB) attenuation than the copolarized component (19 TVR) of the vertically polarized signal. It may be reasonable to expect the cross-polarized component (19 TVRH) of the vertically polarized signal arriving at the horizontal port of the receiver to be weaker than the cross-polarized component (19 THRV) of the horizontally polarized transmitted signal arriving at the vertical port.

One other reason that the measured XPD and XPI for one polarization may not be equal is the presence of other hydrometeors, such as ice particles and snowflakes, that cause depolarization and not significant attenuation along the propagation path.

The analysis of a few ice depolarization events has shown that the XPD and XPI can vary ± 5 -7 dB from their respective clear sky isolations. Again, the physical phenomenon responsible for such depolarization is the difference in phase shift between the orthogonal polarizations. Recently, the study of ice depolarization has attained considerable interest [27] and concern in the communications system design. In general, it is to our advantage to estimate the cross-polarization isolation to be about 2-5 dB lower than the measured cross-polarization discrimination, depending on the system availability specifications.

Another important contribution from this experiment is that it provides a means to compare measured data with the existing empirical models for predicting XPD from copolarized signal attenuation for varying elevation angles. Comparisons with the CCIR formula [21] and its suggested modification on frequency dependence [24] have shown that there are some inherent weaknesses in the model. Comparisons of measured data for different locations, elevation angles, and frequencies may bring

out these weaknesses and will enhance the applicability of the CCIR model.

Acknowledgment

The work described here would not have been possible without the cooperation of the technicians who took care of the hardware used in the measurements. Thanks are due to several colleagues, D. Fang in particular, for comments and suggestions. The discussions with D. Rogers and J. A. Bennett were very helpful, and G. Hyde supervised the data collection. Thanks are due to K. Yeh and her colleagues for the data reduction work and the computer runs. Thanks are also due to L. Pollack for his interest in supporting this work.

References

- [1] L. J. Ippolito, "Radio Propagation for Space Communications Systems," *Proceedings of the IEEE*, Vol. 69, No. 6, pp. 697-727, June 1981.
- [2] T. S. Chu, "Rain-Induced Crosspolarization at Centimeter and Millimeter Wavelengths," *Bell System Technical Journal*, Vol. 53, No. 8, October 1974, pp. 1557-1579.
- [3] H. W. Arnold and D. C. Cox, "Dependence of Depolarization on Incident Polarization for 19-GHz Satellite Signals," *Bell System Technical Journal*, Vol. 57, No. 9, November 1978, pp. 3267-3276.
- [4] D. C. Cox, H. W. Arnold, and H. H. Hoffman, "Depolarization of 19 and 28 GHz Earth-Space Signals by Ice Particles," *Radio Science*, Vol. 13, No. 3, May-June 1978, pp. 511-517.
- [5] D. C. Cox, H. W. Arnold, H. H. Hoffman, and R. P. Leck, "Properties of Attenuating and Depolarizing Atmospheric Hydrometeors Measured on a 19-GHz Earth-Space Radio Path," *Radio Science*, Vol. 15, No. 4, July-August 1980, pp. 855-865.
- [6] S. H. Lin, "Impact of Microwave Depolarization during Multipath Fading on Digital Radio Performance," *Bell System Technical Journal*, Vol. 56, No. 5, pp. 645-674, May 1977.
- [7] I. P. Shkarofsky and S. B. Nickerson, "Multipath Depolarization Theory Combining Antenna with Atmospheric and Ground Reflection Effect," URSI Commission F International Symposium, Lennoxville, Canada, May 26-30, 1980.
- [8] D. C. Cox, "Some Effects of Measurement Errors on Rain Depolarization Experiments," *Bell System Technical Journal*, Vol. 54, No. 2, February 1975, pp. 435-450.

- [9] H. W. Arnold, D. C. Cox, H. H. Hoffman, and R. P. Leck, "Ice Depolarization Statistics for 19-GHz Satellite-to-Earth Propagation," *IEEE Transactions on Communications*, Vol. COM-29, No. 5, May 1981, pp. 710-715.
- [10] M. J. Saunders, "Cross-Polarizations at 18 and 30 GHz Due to Rain," *IEEE Transactions on Antennas and Propagation*, Vol. AP-19, 1971, pp. 273-277.
- [11] J. Thirlwell, D. M. Knox, and R. G. Howell, "Crosspolar Variations on an Earth Satellite Path," *Electronics Letters*, Vol. 13, No. 17, August 1977, pp. 516-518.
- [12] J. J. Schlesak and J. I. Strickland, "Measurements of Precipitation Attenuation, Depolarization, and Site Diversity Improvement in Canada," Preparatory Seminar for 1983 RARC on Broadcasting Satellite Planning, Principles, and Methodology, May 4-8, 1981, Ottawa, Canada.
- [13] R. L. Olsen and W. L. Nowland, "Semi-Empirical Relations for the Prediction of Rain Depolarization Statistics: Their Theoretical and Experimental Basis," *Proceedings*, International Symposium on Antennas and Propagation, Sendai, Japan, August 1978, pp. 477-480.
- [14] W. L. Nowland and J. I. Strickland, "Theoretical Relationship Between Rain Depolarization and Attenuation," *Electronics Letters*, Vol. 13, No. 22, October 1977, pp. 676-677.
- [15] T. Oguchi, "Attenuation and Phase Rotation of Radio Waves Due to Rain: Calculations at 19.3 and 34.8 GHz," *Radio Science*, Vol. 8, No. 1, January 1973, pp. 31-38.
- [16] M. S. Pontes, "A Method to Estimate Statistics of Rain Depolarization," *Extrait Annales des Telecommunications*, Tome 32, Nov.-Dec. 1977, pp. 11-12.
- [17] J. M. Harris and G. Hyde, "Preliminary Results of COMSTAR 19/29 GHz Beacon Measurement at Clarksburg, Maryland," *COMSAT Technical Review*, Vol. 7, No. 2, Fall 1977, pp. 599-624.
- [18] A. F. Standing, "COMSTAR Beacon Receiver," *COMSAT Technical Review*, Vol. 8, No. 1, Spring 1978, pp. 187-203.
- [19] P. N. Kumar, "Precipitation Fade Statistics for 19/29-GHz COMSTAR Beacon Signals and 12-GHz Radiometric Measurements at Clarksburg, Maryland," *COMSAT Technical Review*, Vol. 12, No. 1, Spring 1982, pp. 1-27.
- [20] R. Kaul, R. Wallace, and G. Kinal, *A Propagation Effects Handbook for Satellite Systems Design*, NASA Communication Division, Chapter IV.
- [21] CCIR Report 722(MODF), "Cross-Polarization Due to the Atmosphere," Document 5/1031-E, CCIR XVth Plenary Assembly, Geneva, 1982.
- [22] D. C. Cox, H. W. Arnold, and A. J. Rustako, Jr., "Some Observations of Anomalous Depolarization on 19 and 12 GHz Earth Space Propagation Paths," *Radio Science*, Vol. 12, No. 3, 1977, pp. 435-440.
- [23] C. W. Bostian and J. E. Allnutt, "Ice-Crystal Depolarisation on Satellite-Earth Microwave Radio Paths," *Proceedings IEE*, Vol. 126, 1979, pp. 951-960.

- [24] T. S. Chu, "A Semi-Empirical Formula for Microwave Depolarization versus Rain Attenuation on Earth-Space Paths," To be published in *IEEE Transactions on Communications*, November 1982.
- [25] A. W. Dissanayake, D. P. Haworth, and P. A. Watson, "Analytical Models for Cross-polarization in Rainstorm on Earth-Space Radio Paths for the Frequency Range 9 to 30 GHz," *Annales des Telecommunications*, Vol. 35, November-December 1980, pp. 397-404.
- [26] J. Goldhirsh, "Ice Depolarization of the COMSTAR Beacon at 28.56 GHz During Low Fades and Correlation with Radar Backscatter," *IEEE Transactions on Antennas and Propagation*, Vol. AP-30, No. 2, March 1982, pp. 183-190.
- [27] D. C. Cox, "Depolarization of Radio Waves by Atmospheric Hydrometeors in Earth-Space Paths; A Review," *Radio Science*, Vol. 16, No. 5, September-October 1981, pp. 781-812.

Prabha N. Kumar received a B.S. and an M.S. from Bangalore University, India, in 1968 and 1970, and a Ph.D. in Applied Physics from Southern Illinois University in 1976. From 1970 to 1972 she was a Senior Research Fellow in Modulated Surface Wave Structures at the Microwave Laboratory of the Indian Institute of Science, Bangalore. She was with Computer Sciences Corporation between 1977 and 1979, where she worked on laser reflector arrays. Dr. Kumar joined COMSAT Laboratories in 1979. Her present research centers on the effects of precipitation on satellite signals for frequencies greater than 10 GHz, and on a laser optical rain gauge. Dr. Kumar received the NASA recognition award for her work on laser reflectors in 1981. She is a member of IEEE and of CCIR U.S. Study Group 5.



Optimum orbital location of a communications satellite

A. K. SINHA

(Manuscript received August 5, 1981)

Abstract

This paper describes a formulation for determining the longitude of a geostationary communications satellite that would yield optimum link performance over a specified geographical coverage region. The analysis method addresses the inherent trade-off between the range- and elevation-angle-dependent propagation loss (including rain-induced fading) and the antenna gain variation as a function of the solid angle subtended for a given coverage area. The latter factor arises from the assumption that, as the satellite is moved to an orbital location resulting in a lower elevation angle, with respect to the boresight, for example, the beamwidth required to cover a specified region decreases, hence requiring a larger onboard antenna. The effects of the receive system noise temperature variation with elevation angle and fading are incorporated. The criterion for optimizing satellite location is essentially expressed in terms of the carrier power to noise temperature ratio for the down-link. Illustrative numerical results are presented for the 12-GHz down-link band allocated to broadcast satellite services (BSS).

Introduction

For a specified antenna beam coverage region on the surface of the earth, the longitude of a geostationary satellite determines the necessary satellite antenna beamwidth, *i.e.*, the solid angle subtended by the

coverage region at the satellite, as well as the maximum range and the minimum elevation angle. These factors determine, in turn, the size and the associated directivity or gain of the satellite transmission antenna and the signal degradation due to propagation effects. Signal degradation arises from spreading loss, increase in system noise temperature, and attenuation by the earth's atmosphere. This paper formulates a general analytical model and methodology for determining the optimum orbital location of a geostationary satellite for a specified coverage region on the basis of the above-mentioned factors.

A computer program developed to implement the model for determining the optimum satellite longitude has been used to obtain illustrative numerical examples for specific geographical beam coverage regions. It is shown that, depending on the specific optimization criterion, the optimum location for the satellite differs significantly (approximately 30°) from the longitude of the beam boresight (*i.e.*, the midpoint of the coverage region). In addition, appreciable variation in the satellite link performance may result from a shift in the satellite location, especially when rain-induced fading becomes a predominant factor in system performance.

This paper is divided into two sections: a description of the model and illustrative examples. The first section discusses the role of geometrical and meteorological factors in the optimization and introduces the basic optimization criteria. The second section provides sample computer applications. The relevance of the analyses and systems considerations presented in this paper to future communications satellite systems, such as those using higher frequency bands or providing direct broadcast services, is discussed. Such considerations are pertinent in the context of the RARC-83 Conference, which will address the important questions of appropriate orbital allocations and frequency bands for various types of regional traffic and service requirements.

Model description

The basic optimization criterion is expressed in terms of the minimum value of the down-link carrier power to noise temperature ratio (C/T) that represents the worst-case situation in the coverage region. An alternative criterion based on the average performance, represented by the down-link C/T for the antenna boresight location, has also been considered.

For a given geographical coverage region, satellite transmit power, operational frequency and ground segment equipment characteristics, the variations of the satellite antenna gain, fading and noise temperature

degradations as functions of the satellite longitude are considered. The gain varies because the satellite antenna beamwidth required for a given coverage region is smaller for a satellite located either east or west of the boresight longitude. Smaller beamwidth is, of course, achieved by using a larger aperture while keeping the other system parameters constant. In this discussion, the solid angle rather than the aperture diameter is treated as the basic model parameter to highlight the effect of the shape and size variation of the coverage region.

Geometrical considerations

The geometry of the problem is shown in Figure 1. The specified coverage region is defined by a set of uniformly distributed boundary points S_1, S_2, \dots, S_N , each specified by a colatitude θ_j and a longitude ϕ_j ($J = 1, 2, \dots, N$). The center of the coverage region is denoted by $S_j(\theta_j, \phi_j)$. Let the location (longitude) of the satellite (S in Figure 1) be ϕ . The range of the satellite with respect to S_j is R_j , and the range with

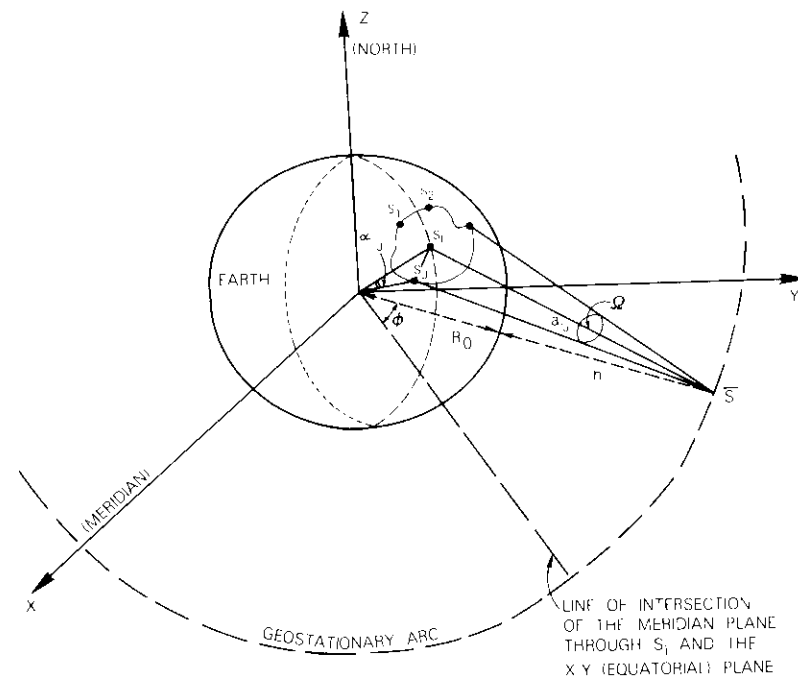


Figure 1. Geometry of Coverage by Satellite Antenna Beam

respect to S_j is $R_j (j = 1, 2, \dots, N)$. Let the maximum range within the coverage region be

$$R_M = \max(R_j : 1 \leq j \leq N) \quad (1)$$

and let Ω be the solid angle subtended by the coverage region at the satellite. Neglecting the sidelobe radiation, which has no direct bearing on the calculation, the transmitted power of the satellite can be assumed to be primarily radiated within solid angle Ω . The received power at S_j is

$$P_r(j) = P_t G_t(j) \left(\frac{\lambda}{4\pi R_j} \right)^2 G_j L_j^{-1} \quad (2)$$

where P_t = satellite transmit power

$G_t(j)$ = satellite transmit antenna gain in the direction of S_j

λ = down-link wavelength

G_j = earth station receiver antenna gain at S_j

L_j = fade factor for propagation loss due to precipitation at S_j .

For a given satellite location, transmit power, earth station antenna size ($G_j = G_r = \text{constant for all } j$), and down-link frequency, the power received is a minimum corresponding to the maximum value of the quantity,

$$\frac{R_j^2 L_j}{G_t(j)} \quad (3)$$

Here it is assumed that the range of climatic and link variation within the coverage region is adequately represented by the set of receiving earth stations $\{S_j : 1 \leq j \leq N\}$ located uniformly around the 3-dB beam edge of the coverage region, so that, except for a roughly constant antenna gain slope or roll-off factor, $G_t(j) \approx 4\pi/\Omega$ for all j . That is, any gain variation over the specified representative set of the earth stations is neglected by assuming that beam shaping provides a 3-dB pattern contour coincident with the geographical boundary of the coverage region. Let $\Gamma_j = R_j^2 L_j$ and

$$\Gamma_{\max} = \max\{\Gamma_j : 1 \leq j \leq N\} \quad (4)$$

Then, the minimum value of the received power is

$$(P_r)_{\min} = P_t G_r \frac{\lambda^2}{4\pi} \frac{1}{\Omega \Gamma_{\max}} \quad (5)$$

Therefore, the optimum satellite location $\bar{\varphi}_o$ is the value of $\bar{\varphi}$ that minimizes the objective function

$$f(\bar{\varphi}) = \Omega \Gamma_{\max} \quad (6)$$

i.e.,

$$\left. \frac{\partial f}{\partial \varphi} \right|_{\bar{\varphi} = \bar{\varphi}_o} = 0$$

This max-min problem thus maximizes the minimum received power or power flux density (PFD) for a given transmit power. This procedure is obviously equivalent to minimizing the satellite transmission power to yield a prespecified threshold value for the minimum PFD within the coverage region.

Fade factor

The loss L_j varies with satellite location because of inherent elevation angle dependence, especially for small elevation angles. To incorporate this dependence and its related effect on system performance, the rain-induced fading factor must be considered and a suitable generalization of the objective function must be introduced.

For any given earth station, as the satellite location is varied, the part of the signal path length within the earth's atmosphere and hence the signal attenuation due to atmospheric absorption varies as shown in Figure 2.

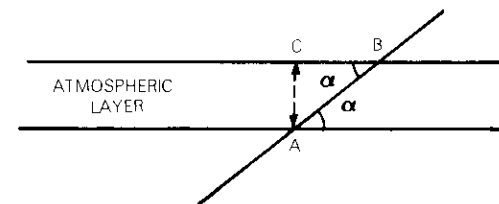


Figure 2. The $\csc \alpha$ Dependence of Atmospheric Path Length with Elevation Angle (α)

The signal path goes from point B to point A , whereas the atmospheric thickness is the distance between C and A . Thus, the characteristic atmospheric path length has a $\csc \alpha$ dependence, where α is the elevation angle of the satellite with respect to the earth station. From empirical observations, it can be concluded [1] that the fade factor F for an earth station at S_J can be written as

$$F = 10 \log_{10} L_J = K_1 \csc \alpha_J \text{ (dB)} \quad (7)$$

where α_J is the elevation angle at S_J ($0 < \alpha_J \leq 90^\circ$, $1 \leq J \leq N$), and K_1 depends on the frequency and the climatic zone classification of the coverage region involved.

Combining equations (3), (4), and (7), and rearranging yields:

$$\Gamma_{\max} = \max_J \{ R_J^2 \exp(0.23 K_1 \csc \alpha_J) \} \quad (8)$$

The minimum received power for a specific satellite location and optimum satellite longitude $\bar{\varphi}_0$ can be determined by using equation (8) in equations (5) and (6), respectively. Note that $K_1 = 0$ represents no fading. In this case, because

$$\Gamma_{\max} = R_M^2, \quad (9a)$$

the objective function is

$$f(\bar{\varphi}) = \Omega R_M^2. \quad (9b)$$

Thus, in the absence of fading, the optimization process is governed only by the tradeoff between the maximum range (spreading) and the solid angle (gain), as expected.

More generally (for $K_1 \neq 0$), because Ω decreases monotonically with respect to the angle by which the satellite is moved to the east or west of the boresight longitude (midpoint in the coverage region), the optimum satellite location is primarily determined by the relative dominance of the increase in satellite transmit antenna gain over the higher signal degradation due to fading.

Worst-case optimization criterion

Besides the fade factor, another source of signal degradation must be included in this consideration: the variation of receiving system noise

temperature with respect to elevation angle and precipitation.

The contributions to the antenna noise temperature from sky radiation and atmospheric emission increase as the elevation angle decreases, thereby increasing the effective system noise temperature and reducing the effective G/T of the receiving ground terminal even for receive antennas of fixed size and gain. Thus, if the optimum satellite location is expressed in terms of maximizing the minimum value of the C/T instead of maximizing the minimum value of the receive power, P_r (or PFD), then the effective noise temperature of the receive system must also be considered.

For a given satellite location, the minimum value of the C/T is

$$(C/T)_{\min} = \min_J \frac{P_r(J)}{T_s(J)} : 1 \leq J \leq N \quad (10)$$

where T_s is the effective system noise temperature of the receiving ground terminal and is given in terms of the antenna noise temperature, T_a , and the receiver noise temperature, T_r , by

$$T_s = T_a + T_r. \quad (11)$$

Thus, the optimization is now the max-min solution based on the modified objective function

$$f_1(\bar{\varphi}) = \Omega(\Gamma T_s)_{\max} \cong \Omega \Gamma_{\max}(T_s)_{\max} \quad (12)$$

where the maximum is with respect to the index set $\{J : 1 \leq J \leq N\}$.

Alternate optimization criterion

The max-min algorithm described in the preceding section obviously corresponds to the worst-case performance in the coverage region. An alternate optimization criterion is the orbital location that maximizes the "average" performance, represented by the down-link C/T ratio at a central location in the coverage region (for example, the beam boresight location). This C/T will be denoted as $(C/T)_{av}$ to distinguish it from $(C/T)_{\min}$, given in equation (10).

Although this method is quite general, the selected optimization criteria, $(C/T)_{\min}$ and $(C/T)_{av}$, involve limitations in the overall scope of optimization, because they reflect only the down-link performance.

Moreover, important factors such as polarization characteristics (*e.g.*, the tilt angle) of the receive field, impact of frequency reuse requirements, and gain variation of the satellite transmit antenna for the directions of individual earth stations $\{S_J: 1 \leq J \leq N\}$ are ignored. Nevertheless, illustrative examples given in the next section highlight the impact of specific criteria on the optimization of satellite location and lead to useful conclusions expected to be generally valid.

Illustrative examples

In this section, some examples of the application of the model are presented for several different types of coverage regions. Appendix A discusses the derivation of the system noise temperature, T_s . The solid angle Ω is easily calculated from the geometry of the problem (see Figure 1).

Evaluating the factor K_1

For the 12-GHz down-link frequency band allocated by WARC-79 for broadcast satellite services (BSS), the value of the fading factor K_1 , which appears in equation (7), has been empirically determined to be 1.36, 0.92, 0.68, or 0.44 dB, depending on the climatic zone classification of the coverage region [1]. For instance, with this classification, the northern and southern segments of the Eastern U.S.* coverage region have values $K_1 = 0.92$ and $K_1 = 1.36$, respectively. A more detailed analysis of the rain statistics of various representative cities in the Eastern region as a function of elevation angle leads to a mean value of K_1 of approximately 0.94, corresponding to 99.75-percent availability (0.25-percent outage) at 12 GHz. Therefore, in the numerical results subsequently given for the Eastern U.S. coverage region, a value of 0.94 is used for K_1 unless otherwise specified.

Effect of the shape, size, and orientation of the coverage region

First, a number of hypothetical beam coverage regions of different geometrical shapes, sizes, and orientations are considered to study the influence of these parameters on the optimization results.

Figures 3a-3c show three hypothetical coverage regions with geometrically symmetrical contours, approximately equal total areas, and the same boresight location. Figure 3a shows an elliptical coverage region

*The Eastern, Central, Mountain, and Pacific regions denote the conventional time zone divisions of the U.S.

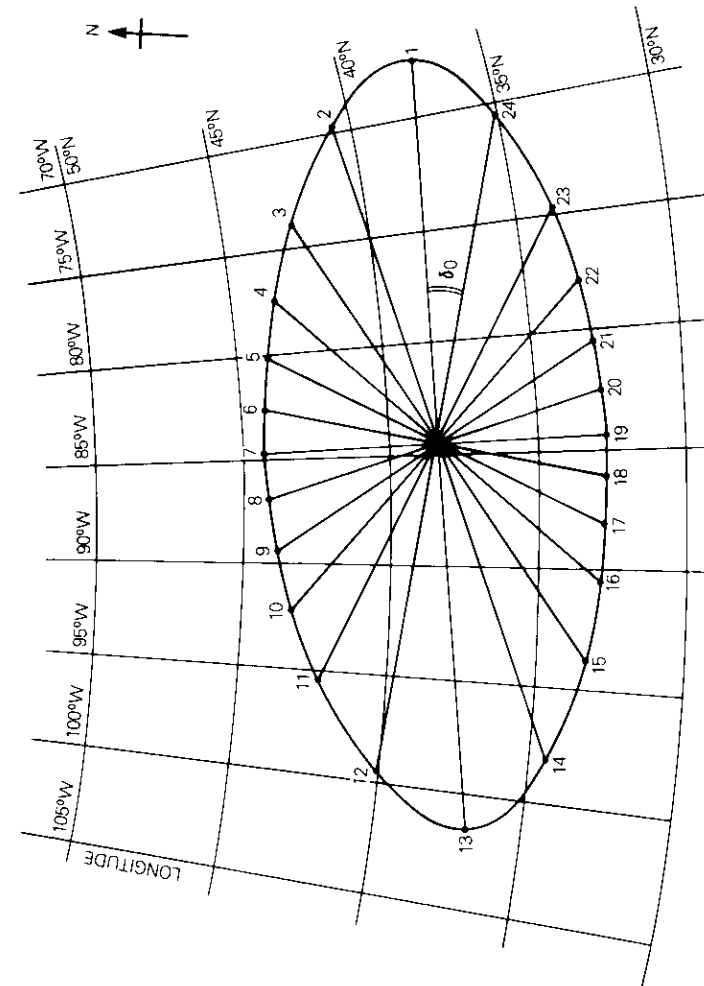


Figure 3a. Elliptical Coverage Region with Major Axis in the East-West Direction

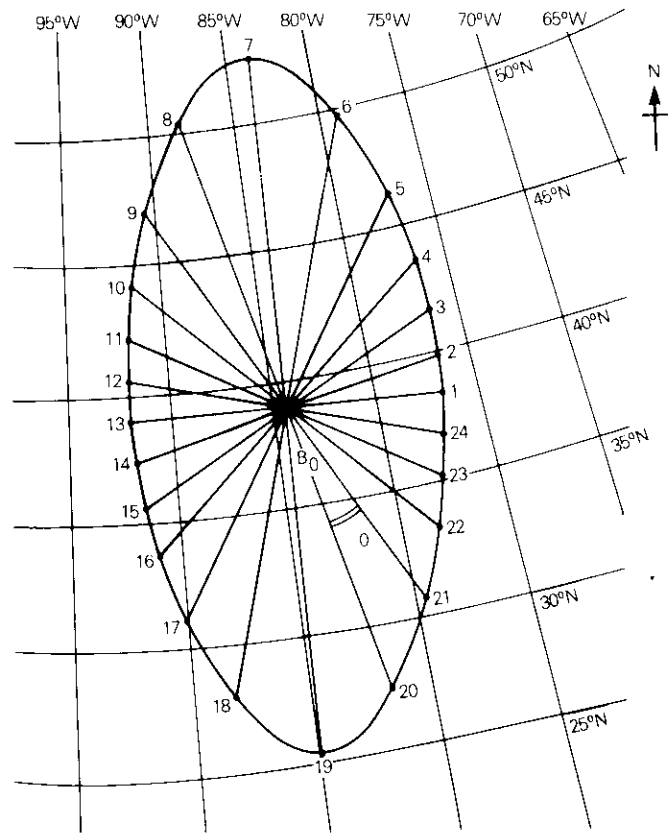


Figure 3b. Elliptical Coverage Region with Major Axis in the North-South Direction

with its major axis in the east-west (E-W) direction. Figure 3b is for an elliptical coverage region with its major axis in the north-south (N-S) direction. Figure 3c shows a circular coverage region. For convenience, Figures 3a and 3b will be referred to as the horizontal and vertical ellipses, respectively. The latitude and longitude grids are marked on each figure. The boundary of each coverage region is marked by 24 numbered points chosen so that the angular separation δ_0 between consecutive points is constant ($\delta_0 = 360/24 = 15^\circ$ in Figures 3a-3c). Such uniform angular

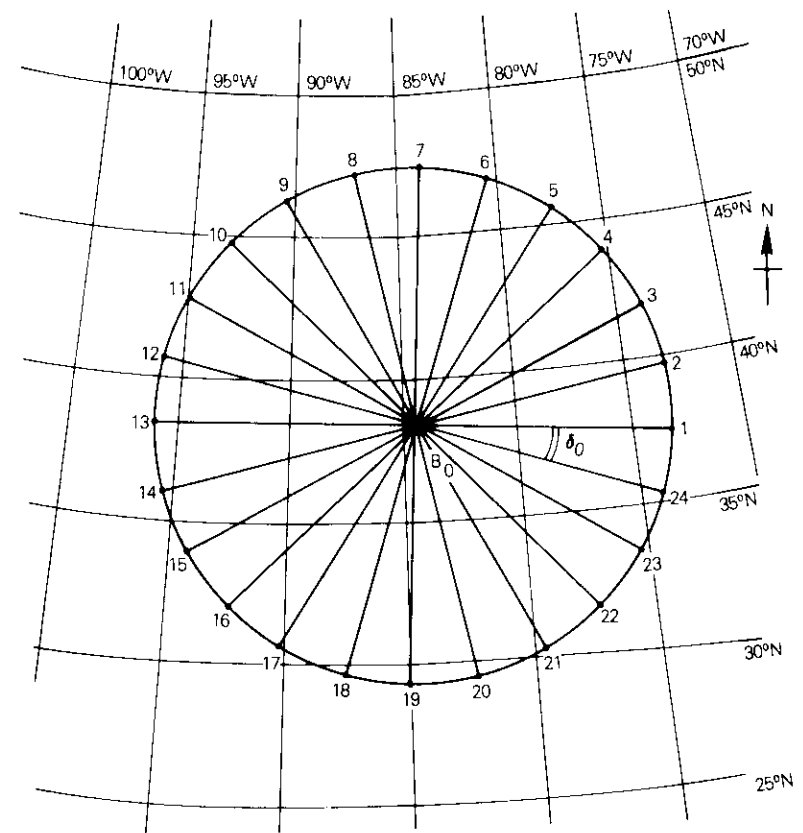


Figure 3c. Circular Coverage Region

spacing of boundary points facilitates estimating the solid angle subtended by the coverage region at the satellite. Also, such spacing is useful for determining $(C/T)_{\min}$ by applying a simple search over the set of boundary points.

Corresponding to the coverage region shown in Figure 3a, the computed antenna gain (G), the minimum carrier power to noise temperature ratio [$(C/T)_{\min}$], as well as the associated values of the fade factor (F) and the receiver system total noise temperature (T) are shown as functions of the satellite location in Figure 4.

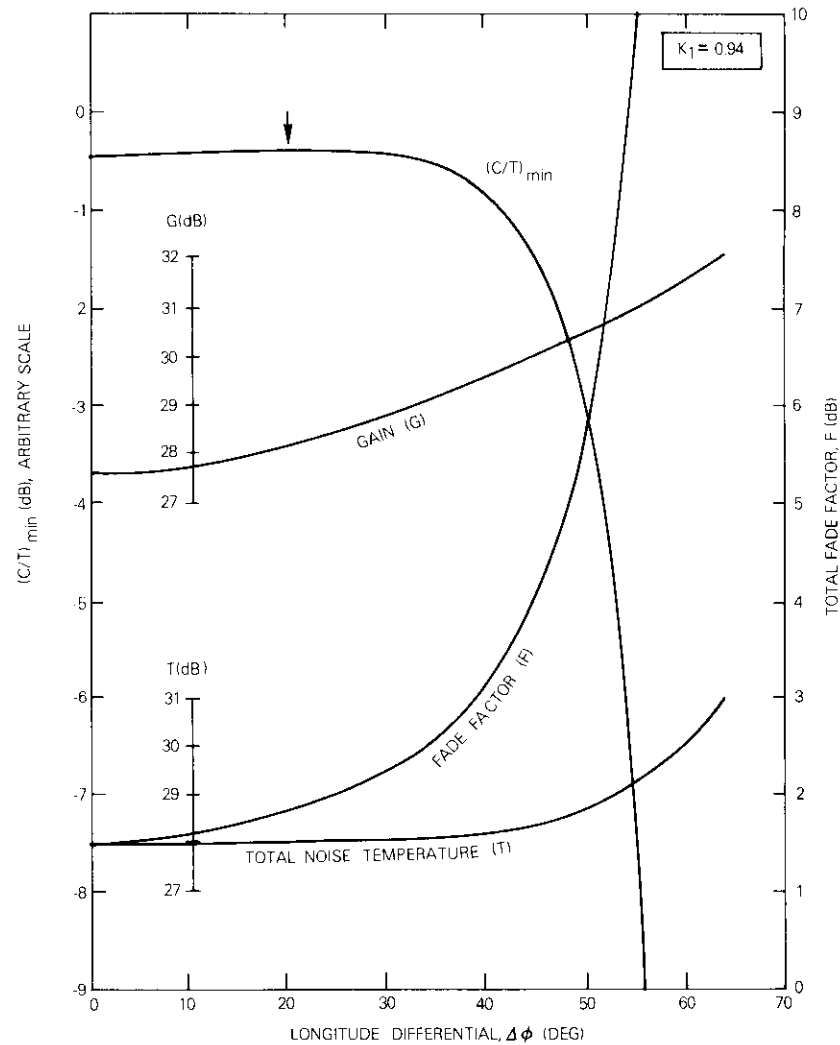


Figure 4. Minimum Performance for the Horizontal Elliptical Coverage Region

The satellite location given in Figure 4 is expressed in terms of the longitude differential

$$\Delta\phi = \bar{\phi} - \phi_0$$

where $\bar{\phi}$ is the satellite longitude and ϕ_0 the longitude of the midpoint of the coverage region or the beam boresight. (This point, denoted as B_0 in Figures 3a-3c, will be referred to as the reference point and the longitude ϕ_0 will be referred to as the reference longitude.) Only positive values of $\Delta\phi$ (corresponding to the westward placement of the satellite with respect to the reference point) are shown. Depending on the longitudinal symmetry of the coverage region, however, similar results occur for negative values of $\Delta\phi$ (corresponding to eastward placement of the satellite with respect to the reference point). Note that practical considerations (namely, desirability of a solar eclipse at the satellite occurring at least an hour after local midnight for the service region) require that the satellite be typically located at least about 15° westward from the coverage region. Therefore, it is sufficient for all practical purposes to consider only positive values of $\Delta\phi$.

As shown in Figure 4, as the longitude differential of the satellite position, $\Delta\phi$, increases, the satellite antenna gain also increases because of the decreasing solid angle resulting from the use of a correspondingly larger satellite antenna, as implicitly assumed here. However, the fading loss and the effective value of the total noise temperature also increase with increasing $\Delta\phi$, and thereby tend to balance out, and finally overshadow, the increase in satellite antenna gain. The net result is typically a slow rise in the resultant $(C/T)_{min}$ for low $\Delta\phi$ values and a rapid decline in $(C/T)_{min}$ for high $\Delta\phi$ values. Therefore, a nominal peak in the $(C/T)_{min}$ curve (marked by a short vertical arrow in Figure 4) results for $\Delta\phi = 20^\circ$, signifying the optimum location of the satellite.

Similar results (not shown) are also obtained for the vertical ellipse (Figure 3b) and the circular coverage (Figure 3c). However, in these cases, the optimum satellite location lies close to the reference longitude (i.e., $\Delta\phi \approx 0$). This difference in the variation patterns, and consequently the results, for the three cases is easily understood in terms of the variation of the beamwidth, or solid angle (and hence gain), with respect to the satellite location for different orientations of the coverage region with respect to the geostationary orbital arc (or the equatorial plane) over which the satellite location is varied. Thus, for the horizontal ellipse (Figures 3a and 4), the solid angle for the satellite at the reference longitude ($\Delta\phi = 0$) is larger and results in approximately 4 dB less gain than that for the location $\Delta\phi = 60^\circ$. In the case of the vertical ellipse (Figure 3b), the gain variation resulting from solid angle variation is found to be less than 1 dB, and for the circular case (Figure 3c), this variation is slightly over 2 dB. Note that throughout this paper it is

assumed that the design of the onboard antenna is appropriately modified for different satellite locations to provide the same footprint of the antenna beam on the ground for the specified coverage region.

Figure 5 shows plots of G , F , T , and $(C/T)_{av}$ vs $\Delta\phi$ for the horizontal

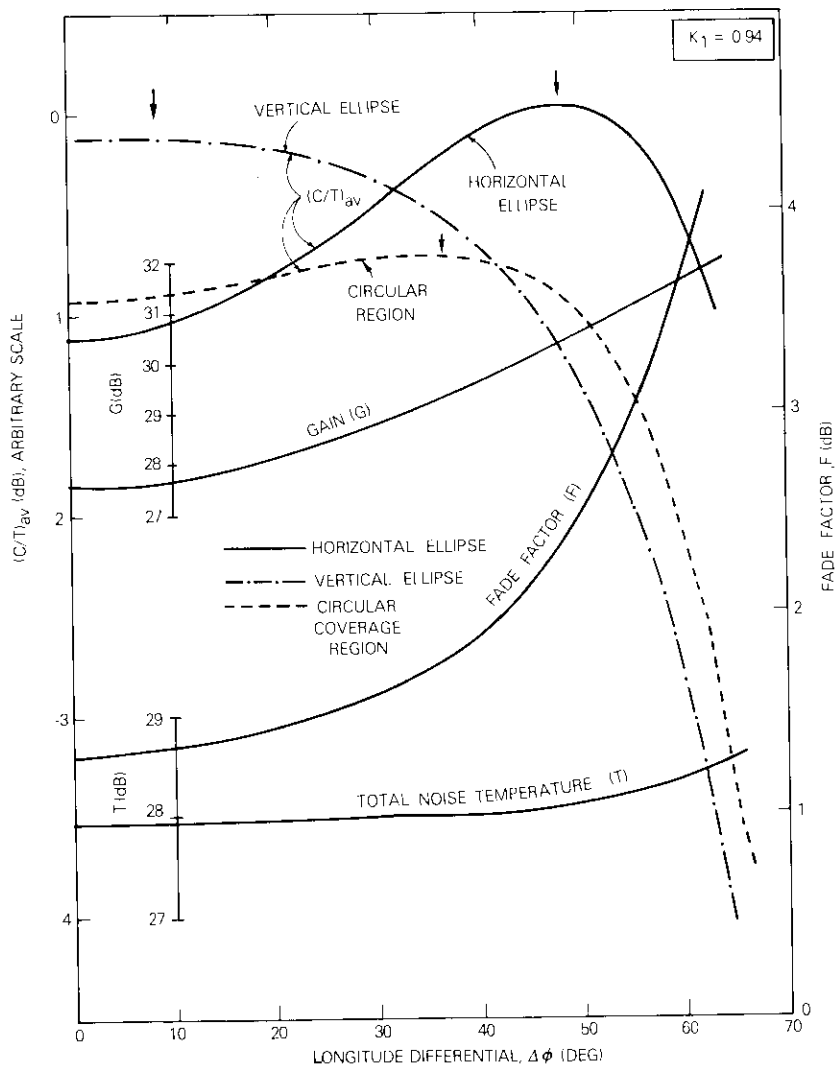


Figure 5. "Average" Performance for the Three Types of Coverage Regions of Figures 3a-3c

ellipse (solid curves). Plots of $(C/T)_{av}$ vs $\Delta\phi$ for the vertical ellipse and circular coverage regions are also shown (dashed and dotted curves, as annotated) for convenience. The curve for the horizontal ellipse displays a pronounced maximum in the $(C/T)_{av}$ curve, indicating an optimum location $\Delta\phi \approx 48^\circ$, with more than a 1.25-dB enhancement in $(C/T)_{av}$ compared to the value at the reference longitude. The curve for the vertical ellipse yields a nominal peak (enhancement ≤ 0.03 dB), for $\Delta\phi \approx 7.5^\circ$. The third curve, for the circular coverage region, exhibits a medium size peak (enhancement ≈ 0.25 dB) for $\Delta\phi \approx 35^\circ$. These variation patterns can again be explained in terms of the relative dominance of the antenna gain enhancement vs fading-induced degradations as a function of satellite location. In addition, the impact of the specific orientation of the coverage region with respect to the geostationary arc on the variation pattern of the antenna beamwidth, solid angle, and gain must be considered.

The size of the coverage region is another parameter that may affect the relative variation of G and F and thereby the optimum location with respect to the reference longitude. In general, an increase in the size of the coverage region is expected to shift the optimum satellite location farther away from the reference longitude because of the larger increase in gain resulting from decrease in solid angle for varying satellite locations. This tendency may not necessarily hold for very large coverage regions, however.

A number of complications arise for a very large coverage region. For instance, different segments of a large coverage region normally correspond to different climatic zone classifications, and the use of any single value of K_1 is not appropriate for the coverage region as a whole. Furthermore, for a very large coverage region, if the satellite is very far from (e.g., to the west of) the reference longitude, the minimum elevation angle corresponding to a point at the opposite (east) extremity might be too small to be acceptable. The latter factor generally tends toward an optimum satellite location that is close to, or actually coincident with, the reference longitude, particularly if the optimization criterion is the worst-case type, for which $(C/T)_{min}$ is determined. However, as exemplified by the case of the horizontal ellipse (Figure 4 vs 5), the optimization criterion based on $(C/T)_{av}$ rather than $(C/T)_{min}$ results in a variation in relative performance with respect to satellite location that is more marked, and also an optimum location generally farther from the reference longitude. These inferences are confirmed by additional numerical examples presented subsequently.

U.S. coverage region

Next, the Eastern U.S. is chosen as an example of the coverage region. Values of the basic parameters are plotted against the satellite location in Figures 6 and 7.

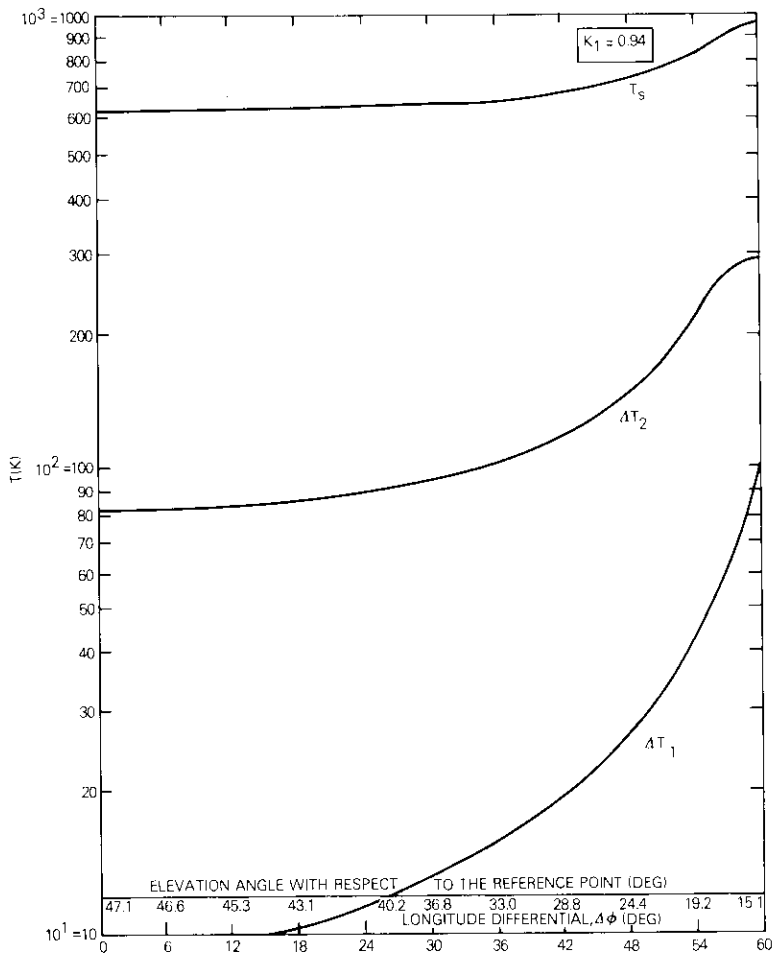


Figure 6. Noise Temperature vs Satellite Location for Eastern United States Coverage Region

Figure 6 shows the dependence of the antenna and receiver noise temperature degradations ΔT_1 and ΔT_2 due to atmospheric absorption and rain fades, respectively (see Appendix A). The resultant total noise temperature, T_s , for the receive system is also shown. It is seen that, with

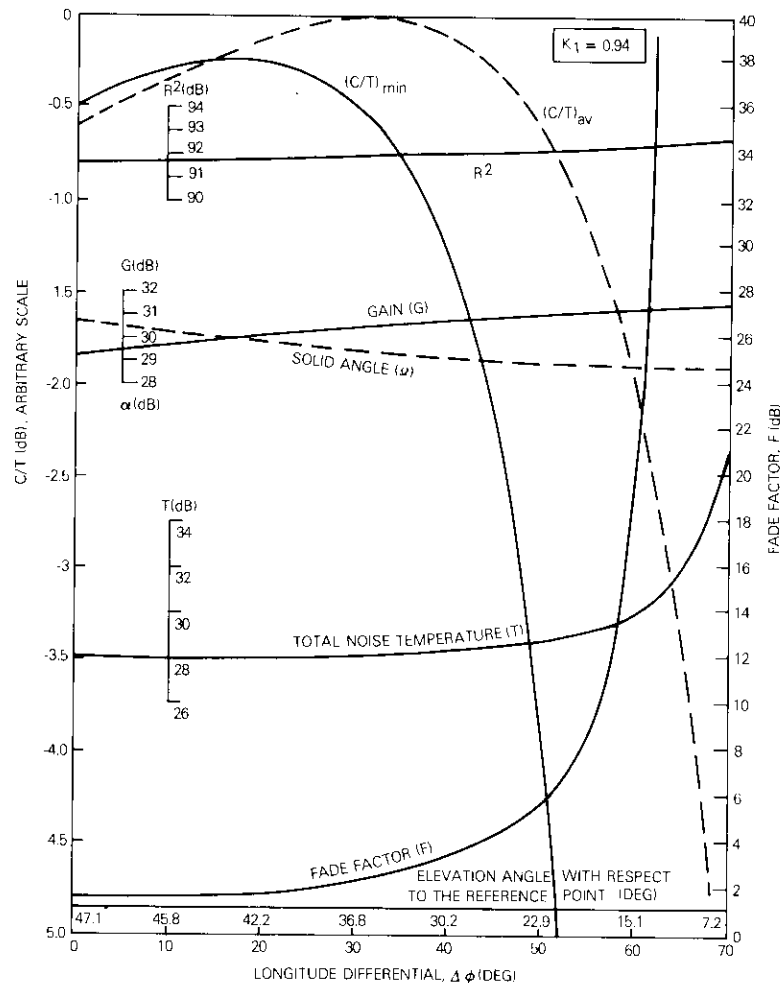


Figure 7. System Parameters vs Satellite Location for the Eastern United States

varying satellite location (and hence varying elevation angle with respect to the reference point, also an abscissa in Figure 6), the fade-induced increment (ΔT_2) in the noise temperature is a dominant factor. ΔT_2 increases with decreasing elevation angle, the rate of increase being relatively small for elevation angles larger than about 30° . At smaller elevation angles, ΔT_2 increases more rapidly with decreasing elevation angle and then approaches an asymptote of 290 K, which is the approximate value for elevation angles below about 15° . The total noise temperature accordingly varies between 620 K for large elevation angles ($\geq 40^\circ$) to approximately 900 K for low elevation angles ($\leq 15^\circ$).

The link performance is summarized in Figure 7, which comprises plots of the fade factor, total noise temperature, solid angle, satellite antenna gain, range or spreading loss (R^2), as well as $(C/T)_{\min}$, vs the longitude differential ($\Delta\phi$). The elevation angle with respect to the reference point is indicated on the abscissa, as for Figure 6. For contrast, corresponding values of $(C/T)_{\text{av}}$ for the down-link to the reference point are also plotted (dashed curve), with the ordinate representing both types of C/T on an arbitrary scale.

It can be seen from Figure 7 that, for low elevation angles, the fade increasingly dominates the link performance, contributing to rapid rise in noise temperature and rapid degradation in $(C/T)_{\min}$, particularly for $\Delta\phi > 45^\circ$. Although the overall variation in $(C/T)_{\min}$ for $0 \leq \Delta\phi \leq 30^\circ$ is small (approximately 0.3 dB), a maximum value $(C/T)_{\min}$ is seen to occur at $\Delta\phi \cong 18^\circ$.

For the $(C/T)_{\text{av}}$ (dashed curve), however, the optimum satellite location is farther away, at approximately 32° from the reference point. The optimal enhancement in the link performance compared to the reference longitude is also larger (approximately 0.6 dB) in this case.

As an additional illustration, Figure 8 provides the two types of C/T vs $\Delta\phi$ curves for the contiguous U.S. (CONUS), with the value of K_1 taken as a parameter. Values of $(C/T)_{\min}$ corresponding to $K_1 = 0.44, 0.68, 0.92,$ and 1.36 are shown, as well as of $(C/T)_{\text{av}}$ (dashed curves) for the two extreme values of K_1 (0.44 and 1.36). In this case, it should be recalled that no single value of K_1 is completely representative of the entire area for such large coverage regions and that the optimum location tends to lie close to the reference longitude, because of the occurrence of very low (below threshold) elevation angles that result from the use of the worst-case performance criterion, $(C/T)_{\min}$. For the "average" performance criterion, $(C/T)_{\text{av}}$, on the other hand, a shift of over 50° from the reference longitude and performance enhancement of over 1 dB with respect to that

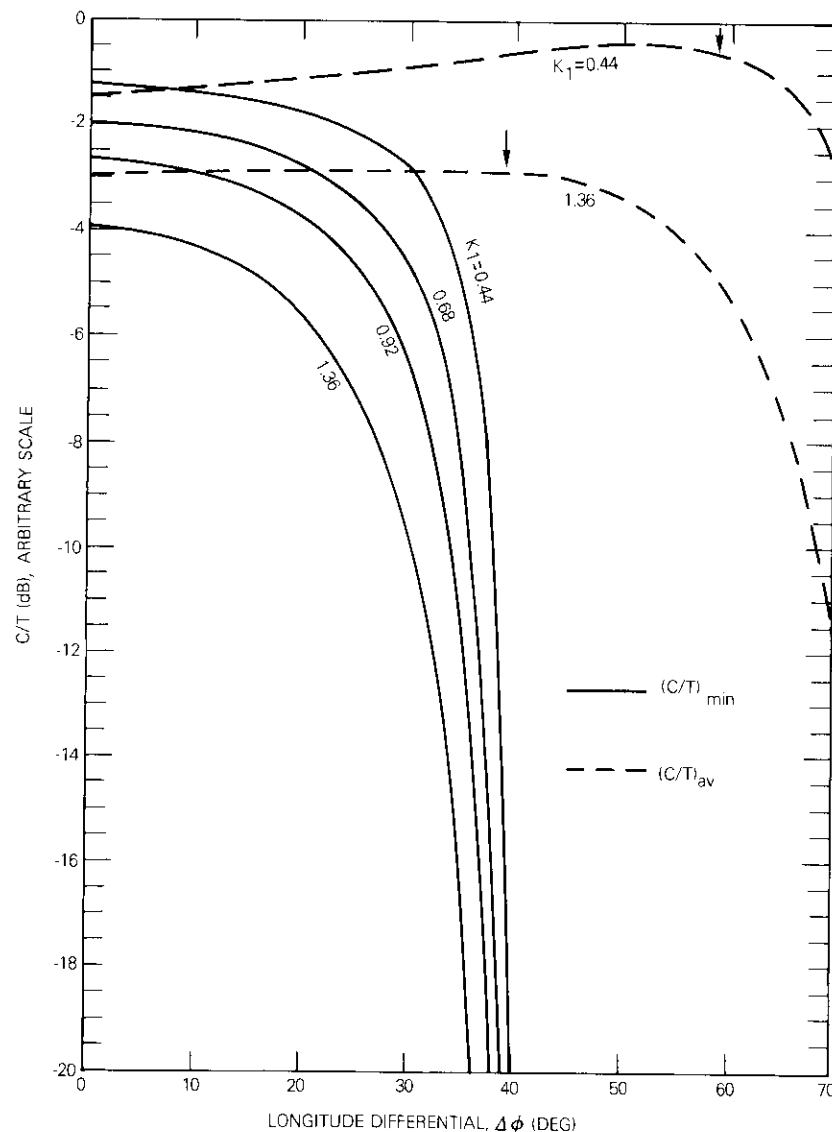


Figure 8. Link Performance for the CONUS Coverage Region

at the reference longitude are observed for the optimum location for $K_1 = 0.44$. Both the enhancement and the angular shift diminish con-

siderably (to about 0.1 dB and about 25°, respectively) for the higher value of K_1 (1.36).

Obviously, an increase in K_1 represents a higher level of fading and related degradation. Equivalently, a larger K_1 implies that fading effects progressively dominate the monotonic increase in satellite antenna gain with respect to increasing shift in the satellite location from the reference longitude. Because the variation in antenna gain is responsible for shifting the optimum satellite location from the reference longitude, an increase in K_1 is generally expected to lead to an optimum location closer to the reference longitude, and also to diminished gain-induced enhancement in link performance, as observed in Figure 8.

It should be remembered that the analysis in this paper addresses gain variation and fade-induced degradation for the down-link only and assumes that all link parameters except the satellite longitude and onboard antenna aperture size are fixed. Similar variations will occur for the up-link as well. For this reason, the net effect on the system performance as a function of the satellite longitude will be more pronounced than indicated in this analysis, and system planning must include these effects.

Clearly, even a small enhancement (e.g., 0.5 dB) in $(C/T)_{\min}$ or $(C/T)_{\text{av}}$ achieved through optimizing satellite location, as exemplified in this paper, may be useful for a direct broadcasting satellite system. Because small home terminals receive the signals directly, the utmost maximization of received PFD for a specified satellite output power or the utmost minimization of satellite output power requirement for a specified PFD threshold is important for system economy and viability.

Conclusions

A simple analytical model has been presented to study the impact of the longitudinal location of a geostationary satellite on the communications performance (down-link C/T) of the system for a specified coverage region. The inherent tradeoff is between satellite antenna gain (associated with the variation in satellite antenna aperture consistent with the satellite location necessary to maintain a basic beam coverage, or terrestrial footprint of the antenna pattern) and rain-induced fading, as well as noise degradation, as a function of elevation angle. Suitable optimization criteria and objective functions have been defined to determine the optimum satellite location. The computer program developed to implement the model has been used to provide illustrative numerical results for various types of coverage regions for the down-link frequency in the 12-GHz frequency band allocated for BSS.

It is observed that the optimum satellite longitude may typically be 10° to 40° from the longitude of the beam boresight, depending on the optimization criterion selected. For the worst-case performance within the coverage region, generally the value of down-link C/T varies within a small range (approximately 0.5 dB) for large longitudinal variations (approximately 30°) in the satellite location. Therefore, in practice, a fair degree of flexibility may exist in selecting the satellite location. However, for the "average" performance, represented by the down-link C/T at the boresight location, a larger degree (approximately 1 dB) of link enhancement and a larger shift (>30°) of the optimum satellite longitude from the boresight longitude may result.

The sensitivity of the optimum satellite location to the variation of the shape, size, and relative orientation of the coverage region and the intensity of fading has also been briefly analyzed. It is observed that for a coverage region where E-W dimensions are much larger than its N-S dimensions, the optimum satellite longitude is farther away from the boresight longitude than in the reverse case (i.e., N-S dimensions larger than E-W dimensions). Also, the link enhancement resulting from shifting the satellite from the boresight longitude to the optimum longitude is larger in the former case than in the latter.

Although no specific example has been given for other frequency bands, similar results are generally expected to hold. At higher frequencies (e.g., 30/20 GHz), fading effects are expected to dominate, implying that the optimal satellite locations may be relatively closer to the boresight longitude. In general, for any type of service (and hence operating frequency band), coverage region (shape, size, orientation, and climatic conditions), and optimization criterion (maximization of the worst-case or the average link), the optimum satellite location can be determined by this model. Obviously, this type of optimization is desirable before regional allocation of the geostationary arc and frequency bands for various types of services [fixed satellite service (FSS), BSS]. The importance of such optimization escalates as growing communications needs inevitably lead to smaller spacing between adjacent satellites in the geostationary arc. Thus, the type of optimization methodology presented here may be of interest to RARC-83, as well as to domestic and international entities involved with implementing communications satellite programs. The optimization procedure that has been presented should prove to be a useful step toward the efficient use of the three most important yet limited resources of satellite communications systems: the geostationary arc, the spectral bandwidth, and the satellite (down-link) power.

Acknowledgment

The author is indebted to J. Whitworth for his support of this study and helpful discussions. D. Rogers from COMSAT Labs provided rain fade data used for evaluation of the fading constant. C. DePeuter and K. Ebert provided valuable assistance in the presentation of the numerical results. E. Reinhart presented a summary of the results of this study as part of the U.S. contribution to the CCIR Study Group II in Geneva in September 1981.

Reference

- [1] CCIR Report 811, "Broadcasting Satellite Service Planning Elements Required for the Establishment of a Plan of Frequency Assignments and Orbital Positions for the Broadcasting-Satellite Service in the 12 GHz Band," Kyoto, 1974.

Appendix A. Evaluation of the increase in the noise temperature

For simplicity, the following model is used for the receiver antenna system noise temperature:

$$T_s = T_0 + \Delta T_1 + \Delta T_2 \quad (\text{A-1})$$

where T_0 is the nominal value, while ΔT_1 and ΔT_2 represent noise degradations corresponding to the enhancement of antenna background sky noise and fade-induced receiver noise, respectively. At 12 GHz (down-link), the following approximations are used:

$$T_0 = 537 \text{ K} \quad (\text{A-2})$$

$$\Delta T_1 \cong \frac{300}{\alpha} \text{ K} \quad (\text{A-3})$$

$$\Delta T_2 \cong 290 (1 - 10^{-F/10}) \text{ K} \quad (\text{A-4})$$

where α is the elevation angle in degrees and F is the fade constant in dB as given in equation (7).

The value of T_0 includes 527 K as the nominal receiver noise temperature plus 10 K as the antenna background noise. Approximation (A-3) for ΔT_1 is based on a rough numerical fit to measured data given in the literature [A-1]-[A-4]. Approximation (A-4) for ΔT_2 is simply related to the transmittance of the atmosphere in the presence of the elevation-angle-dependent fading.

References

- [A-1] P. F. Panter, *Communication System Design*, New York: McGraw Hill Book Co., 1972.
- [A-2] D. C. Hogg, "Problems in Low Noise Reception of Microwave," IRE Trans. 5th National Symp. Space Electronic Telemetry, pp. 1-11, 1960.
- [A-3] L. V. Blake, "Antenna and Receiving System Noise Temperature Calculation," NRL Report 5668, September 19, 1961.
- [A-4] A. Miya (Editor), *Satellite Communications Engineering*, Lattice Corporation, Tokyo, Japan, 1975.

Ashok K. Sinha received a B.Sc. and an M.Sc. in physics from Patna University, India, and a Ph.D. in physics from the University of Maryland. In 1974 he joined COMSAT Laboratories, where he worked on analytical computer-based modeling, optimization, performance analysis, and long-range planning methodology of communications satellite systems, including TDMA and ISL. Subsequently, he was involved in technical analysis and planning of several overseas (ARABSAT, SATCOL, and CHINASAT) and domestic (DBS) satellite systems with COMSAT's Systems Technology Division. He also participated in studies for NASA and others relating to the 30/20-GHz band, the space platform, the space shuttle, and the INTELSAT VI program. In 1982, after becoming Manager of Systems Engineering of the INMARSAT Division, he joined INTELSAT, where he is responsible for Service Development as part of future planning activities. He is a member of the International Union of Radio Science, the International Association of Geomagnetism and Astronomy, the American Physical Society, and IEEE.



Cancellation of acoustic feedback

O. HORNA

(Manuscript received June 29, 1982)

Abstract

Echo cancellers employing adaptive finite impulse response filters (AFIRFs) are used to eliminate the disturbing effects of echo phenomena in long-distance telephone communication systems. Acoustic echo cancellers (AECs) are similar devices that can be used to reduce the effects of echoes and acoustic coupling between loudspeakers and microphones in teleconference rooms or public address systems. AECs must have a processing window of at least 50 ms, a bandwidth of 5 to 7.5 kHz, and a substantially wider dynamic range than the echo cancellers used in telephone systems.

Several models were built to test AECs under actual conditions. A series-parallel organization of convolution processors and memories was employed to allow an increase in the number of coefficients to 750. Also, a special VLSI circuit was developed to simplify the digital part of the AEC, and a digital automatic gain control circuit was used to reduce the dynamic range of the microphone signal.

A teleconference room organized and acoustically designed to minimize the echo control problem is also discussed.

Introduction

Echo cancellers employing AFIRFs are widely used in long-distance telephone circuits to remove echoes generated at the hybrid coil that connects four-wire long-distance circuits to two-wire local circuits (Figure 1) [1], [2]. Experiments performed at COMSAT Laboratories [3] have revealed that echo cancellers could also reduce the acoustic coupling between

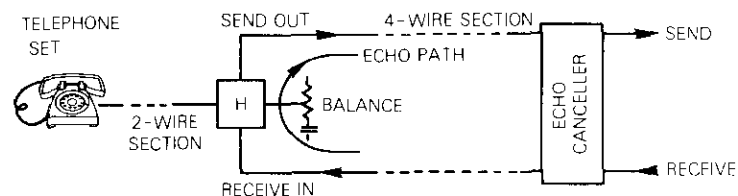


Figure 1. Long-Distance Telephone Connection With Echo Canceller

microphones and loudspeakers, for example, in a teleconference room (Figure 2). These experiments also revealed that a canceller intended for the control of acoustic echoes must meet requirements different from

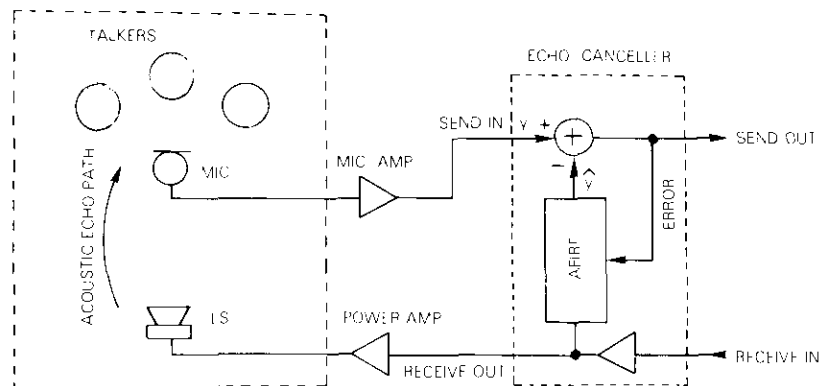


Figure 2. Teleconference Circuit With Echo Canceller

those for the echo cancellers presently used in telephone systems. These differences are apparent from Table 1, in which the electric parameters of a production-type telephone echo canceller (TSI Model EC4500) are compared to those of an experimental AEC (Figure 3).

Teleconference room

A teleconference room should provide conference participants with an acoustic, visual, and psychological environment resembling that of a regular conference room as closely as possible, while minimizing acoustic echo control problems. A typical room setup is shown in Figure 4. Participants are seated around a table equipped with one or more microphones

TABLE 1. COMPARISON OF PARAMETERS OF A TELEPHONE ECHO CANCELLER (TELESYSTEMS, INC., MODEL EC4500) WITH AN EXPERIMENTAL ACOUSTIC ECHO CANCELLER

PARAMETER	EC4500	AEC
Bandwidth (kHz)	3.3	5.2
Sampling Frequency (kHz)	8.5	12.8
Processing Window (ms)	30.1	60
Number of Coefficients	256	768
Flat Delay Compensation (ms)	No	Max. 26
Quantization Resolution (bits)	5	6
Dynamic Range (dB)	42	48
Overload Point (dBm0)	+3	+6
Minimum Echo Return Loss (dB)	6	3

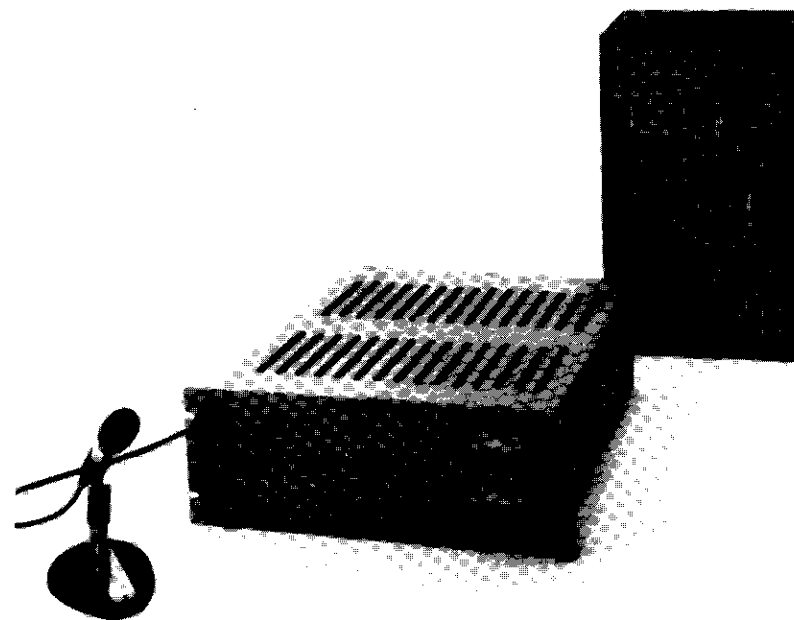


Figure 3. Experimental Acoustic Echo Canceller

and facing a wall where the TV monitor, loudspeaker(s), and TV camera are located. This arrangement does not restrain the movement of participants, but keeps them at a proper distance from the microphone and in view of the TV camera.

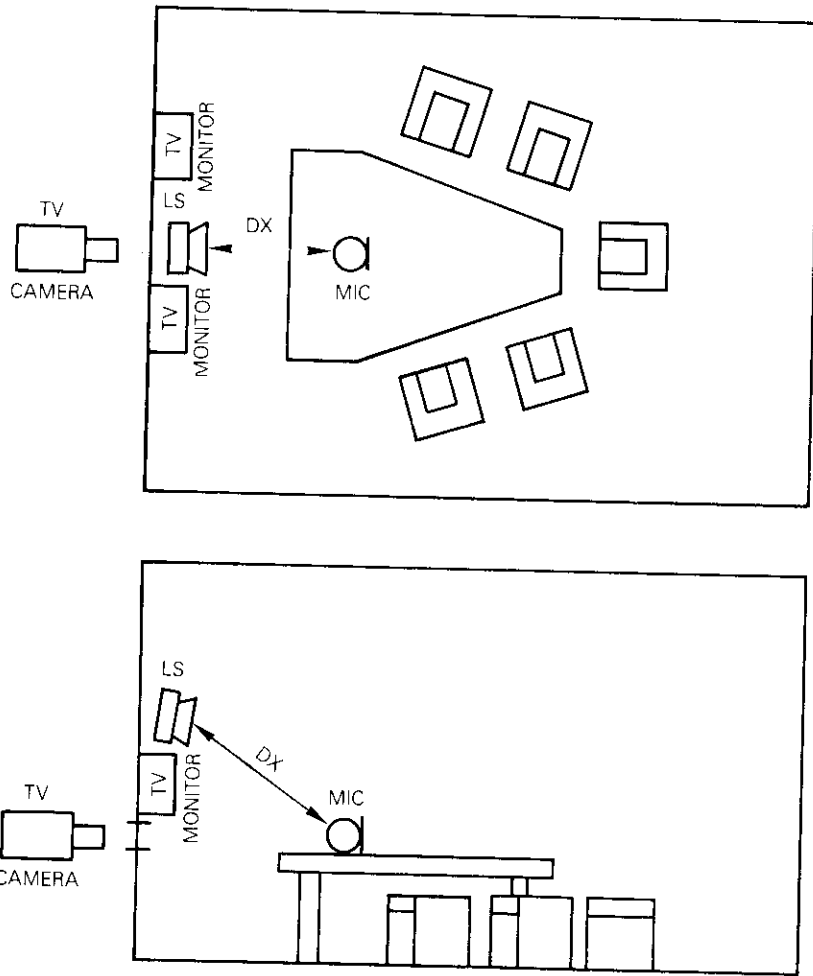


Figure 4. Teleconference Room Setup

The average preferred listening level [4] is between 59 and 72 dB (relative to a sound level pressure of 0.2×10^{-9} bar) and depends on the noise level in the room (Figure 5). The preferred speech level measured at 1 meter in front of the speaker also depends, to a lesser extent, on the noise in the room (measured with the A-weighting frequency characteristic, Figure 6).

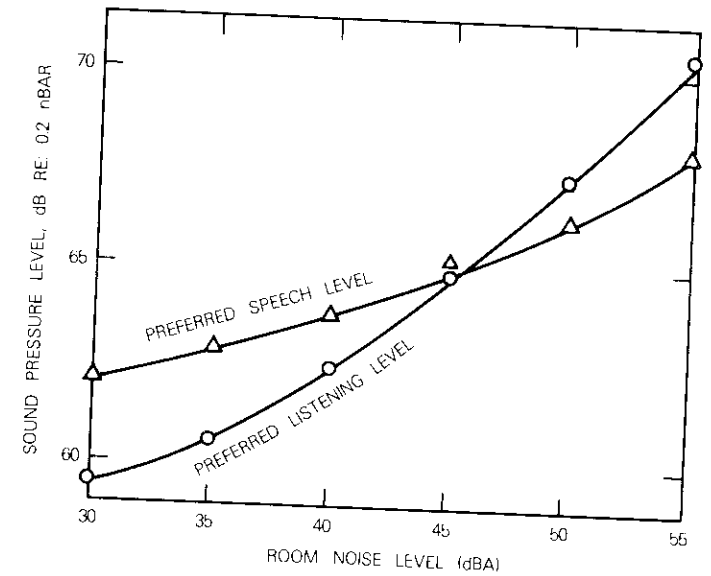


Figure 5. Average Preferred Listening and Speech Level Relative to Room Noise Level (A-Weighting)

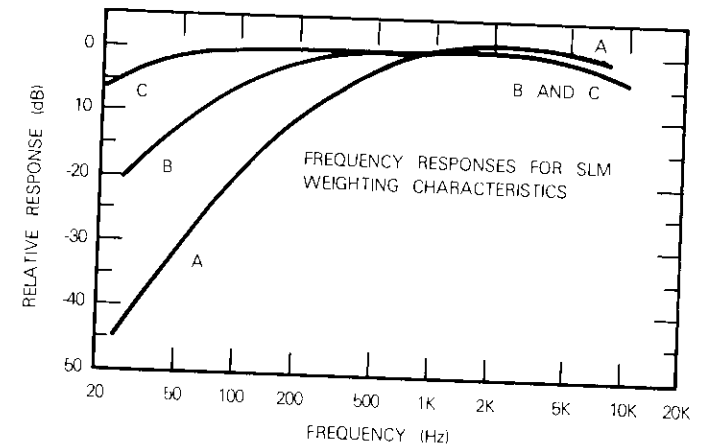


Figure 6. Frequency Response Characteristics for Sound Level Meters According to ANSI-S1.4-1971

The noise level in a teleconference room should not be higher than the level recommended for TV studios, theaters, and music rooms [5], that is,

below the noise criteria curve NC-25 (Figure 7). The NC-30 curve should be considered as the absolute maximum ambient noise level for the arrangement in Figure 4. For higher noise levels, individual microphones must be close to each participant because good intelligibility of transmitted speech requires a signal-to-noise ratio substantially better than that needed in direct face-to-face speech communications. Binaural hearing, in the latter case, substantially improves the subjective ratio between desired and undesired signals.

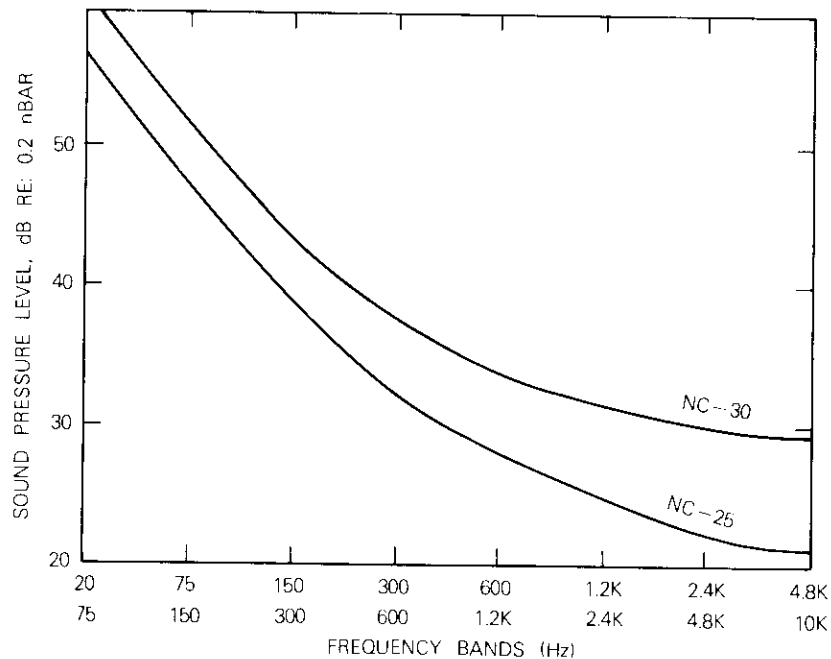


Figure 7. Recommended Noise Criteria Curves: NC-25 for TV Studios and NC-30 for Motion-Picture Theaters

Acoustic design

The reverberation time, T_R , in a teleconference room must be relatively short, $0.1 < T_R < 0.25$ s (-60 dB), to accomplish the following:

a. ensure good intelligibility of transmitted speech under the acoustic conditions shown in Figure 4, with constantly open microphone(s);

b. have the shortest possible processing window in the AEC for the required acoustic echo return loss (AERL) enhancement;

c. reduce the acoustic coupling between the loudspeaker and the microphone (Figure 4) as much as possible to achieve a positive AERL for given preferred speech and listening levels (Figure 5). This condition is necessary for proper adaptation of the AEC transversal filter and for the stability of the response under "double-talk" conditions, that is, when both parties are talking simultaneously [6].

At a certain distance, D_c , the sound level radiated directly from the loudspeaker (which follows the $1/(4\pi D^2)$ law) drops to the same level as the reverberant sound. This critical distance [5]

$$D_c = 0.03121 \sqrt{\frac{Q \cdot V}{T_R}} \quad (1)$$

depends on the directivity ratio Q of the loudspeaker ($5 \leq Q \leq 50$), the volume V (ft^3) of the room, and the reverberation time T_R . If the microphone is placed at a distance $D_x = D_c$ (Figure 4), the maximum acoustic separation between the loudspeaker and the microphone is only 3 dB, even if the microphone's characteristic is an ideal cardioid. For distances $D_x > D_c$, the acoustic field is a nearly steady reverberant and the separation approaches 0 dB. In this case, the AERL is limited to the difference between the preferred speech level and the listening level, which is positive (2 to 3 dB) in a quiet room (Figure 2).

To improve the AERL, the critical distance in the room must satisfy $D_c \gg D_x$. From equation (1), it follows that an ideal teleconference room should have not only good acoustic damping (short T_R), but also a relatively large volume V (all room dimensions $\gg D_c$, see Figure 4). Also, both the microphone and the loudspeaker should have a high directivity ratio, Q . This latter is the least expensive way to increase D_c .

AEC design criteria

The design philosophy of a telephone echo canceller has been described in detail [4]. Typical parameters of a production model (TSI Model EC4500) are given in Table 1. The internal operational code is pseudologarithmic, with 5-bit resolution, and the echo return loss (ERL) enhancement is better than 20 dB, with $\text{ERL} = 6$ dB. The residual echo is suppressed by a nonlinear device termed a "center clipper" [6].

The required parameters for an AEC differ from those of telephone echo cancellers as follows (also refer to Table 1):

a. Since the reverberation time can reach 250 ms, it is necessary to use a processing window of about one-third of the reverberation time. Hence, $50 < T_d < 85$ ms must be used to obtain an AERLE of approximately 20 dB.

b. The bandwidth must be extended 5 to 7.5 kHz to achieve broadcast-quality transmission, and the sampling rate must be increased accordingly. Consequently, for a 60-ms window, the number of coefficients must be equal to or greater than 750.

c. The residual echo (error signal) must be reduced to curtail distortion caused by the center clipper. This requires a code with an improved resolution of 6 to 7 bits.

d. The dynamic range of the signal must be substantially greater. The distance between the talker and the microphone varies, and acoustic feedback to the talker's ear, which adjusts the volume of the telephone conversation, is lacking in AECs.

e. The speed of adaptation must be maintained as high as possible, preferably <100 ms, because a sudden position change by a person close to the microphone can alter the echo response.

Based on these considerations, the design of AECs must be more complex than that of echo cancellers for telephone system applications.

Computational algorithms

A block diagram of a teleconference room with an acoustic echo path and an AEC is shown in Figure 2. The AFIRF emulates the unit impulse response of the electro-acoustic echo path, convolves it with the received signal, and subtracts the simulated echo \hat{y} from the true echo signal y . The error $\epsilon = y - \hat{y}$ is used to compute corrections for the coefficients of the filter that will eventually reduce $\epsilon \rightarrow 0$. Figure 8 is a block diagram of the digital AFIRF.

The input signal X is sampled, converted into digital form $[(S + H)/ADC]$, and samples x_{i+j} are stored in a shift register for n sampling periods, T_s . A similar register contains the coefficients h_j , that is, the samples of impulse response $H(t)$. The total length T_d of the delay line, $T_d = nT_s$, is called the "processing window." The multipliers with the accumulator form the convolution processor.

By using Svoboda's fast converging method for matrix inversion [7] and Berndt's sign correlation algorithm [8], a new, simple, and relatively fast computational method for AEC AFIRFs was developed. The simulated echo sample after the i -th sampling period is computed from

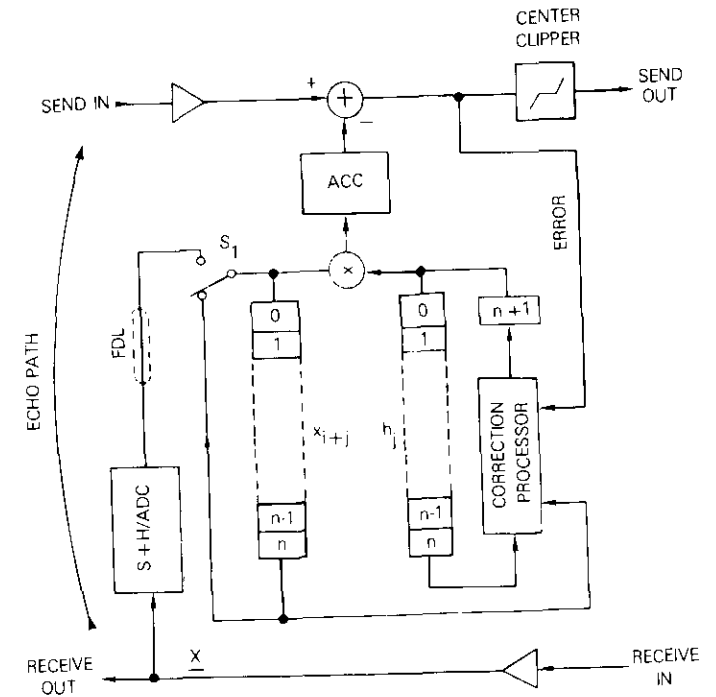


Figure 8. Digital Implementation of the Adaptive FIR Filter as Used in the Echo Canceller

$$\hat{y}(i) = \sum_{j=0}^n x_{i+j}h_j(i) = \sum_{j=0}^n x_{i+j}h_j(i-1) [1 + \Delta_f(i)] \quad (2)$$

The multiplicative correction factor $\Delta_f(i)$ is determined from

$$\Delta_f(i) = \eta f(i-1) \varphi(i+j-1) \text{Sgn } x_{i+j-1} \text{Sgn } \bar{e}(i-1) \quad (3)$$

The functions $f(i)$ and $\varphi(i+j)$ are defined as follows [9]:

$$f(i) = \left[\frac{\bar{e}(i)}{\alpha + \beta \bar{X}_i} \right]_{I2} \quad (4)$$

$$\varphi(i + j) = \left[\frac{x_{i+j}}{\gamma + \delta \bar{X}} \right]_{I2} \quad (5)$$

where

$[\cdot]_{I2}$ = integral part of $[\cdot]$ quantized with 2-bit resolution

$\alpha, \beta, \gamma, \varphi,$ and η = constants [2], [6]

$\bar{e}(i)$ = average value of error in the last m sampling periods

\bar{X}_i = average value of signal samples x_{i+j} in the memory register.

It is obvious that calculations with the above equations require very little computational effort, especially where pseudologarithmic (floating-point) arithmetic is used [6].

Processing window

If the distance between the microphone and the loudspeaker is held constant, the “flat delay” portion (3 ms/m) of the echo path response can be compensated by a delay line between the converter and convolution processor (see FDL in Figure 8). This can reduce the size of the x_{i+j} and h_j memory registers. The delay must be at least 25 ms, and it has been experimentally determined that delay adjustments in 1.5- to 2-ms steps are required to achieve optimum results.

The number n of coefficients h_j in the processor is limited by the read-write time of the memory. It is presently $n \approx 250$, with a 15-kHz sampling rate. The longer processing window ($n \geq 250$) was implemented by cascading several processors, as shown in Figure 9. The memory registers that store signal samples x_{i+j} and impulse response samples h_j are divided into several shorter sections, each with individual multipliers and accumulators [10].

During every sampling period, when multiplexer S_1 is switched into position b to load a new x sample into the X register, the “oldest” sample from register 1 is transferred by multiplexer S_2 into register 2. Therefore, the first part of the filter processes samples x_0 to x_{n-1} , the second part processes samples x_n to x_{2n-1} , etc. The products $h_j x_{i+j}$ are added in accumulators ACC1, ACC2, and ACC3, and, at the end of the convolution cycle, all components of the estimate of a complex echo are subtracted from the

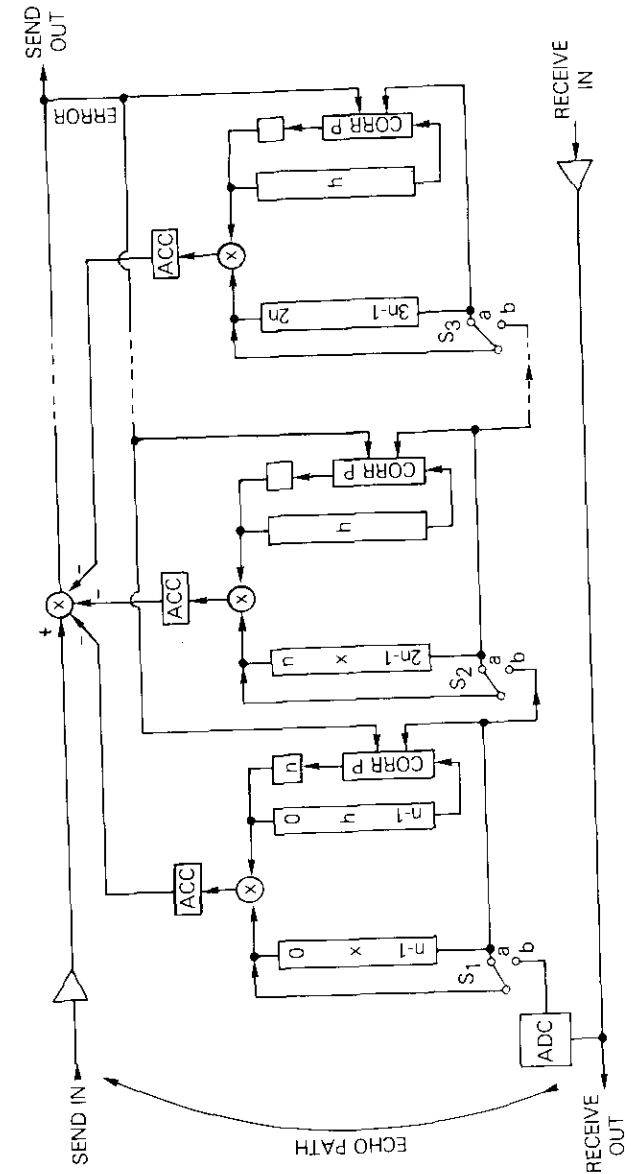


Figure 9. Cascading of Several Digital Sections for FIR Filters With More Than 256 Coefficients

true signal. The same error signal, e , is used by all correction processors to compute corrections δh_j during the next cycle.

VLSI convolution processor

Since the floating-point multiplier and accumulator represent most of the AEC's digital hardware, a semicustom VLSI circuit was developed to reduce the size, complexity, and power of the canceller. Figure 10 is a block diagram of this circuit. Its inputs are the exponents of samples of

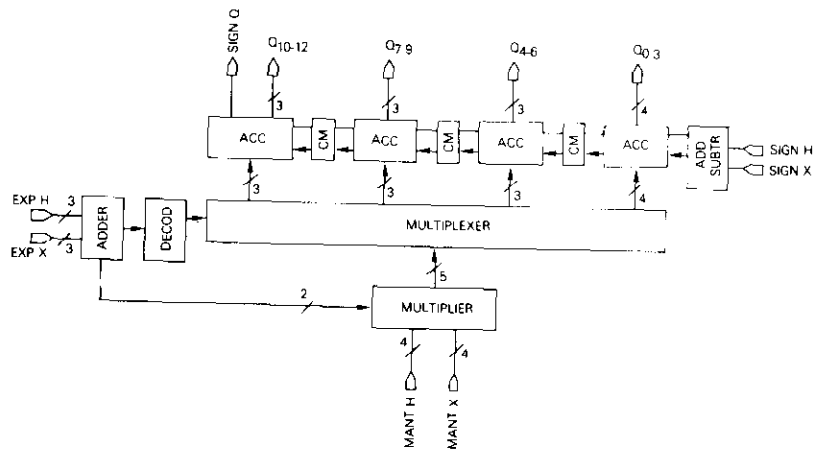


Figure 10. VLSI Convolution Processor (Floating-point multiplier and accumulator)

signal x_{i+j} and response h_j , the mantissa of the product of $x_{i+j} \cdot h_j$, and the signs of the samples. The exponents are added and their sum, E_{xh} , is decoded to form the input of the static shifter (multiplexer), which shifts the 5-bit product $x_{i+j} \cdot h_j$ to the left by E_{xh} places. Thus, the floating-point product is converted to a 13-bit fixed-point number, which is then added to a 14-bit accumulator. The logic is conventional except for the accumulator, which is divided into four sections with memories for the carry bits from the previous addition or subtraction. At the end of each convolution cycle, three clock pulses are used to add the stored carry bits. This accumulator organization permits fast operation and eliminates complex look-ahead logic circuitry for fast carry propagation, which would require long interconnections inside the chip and would occupy a substantial part of the chip area.

Automatic level control

Although the impulse response of the acoustic echo path can change rapidly, the range of the changes is relatively narrow for a given room and arrangement of microphones and loudspeakers. Therefore, the required dynamic range and resolution for h_j samples can be implemented by using existing techniques.

The audio A/D converters limit the dynamic range and resolution of signal samples x_{i+j} to 13 to 14 bits, which is not always sufficient. Performance can be improved if the signal level is held in a narrower dynamic range by the automatic gain control (AGC) device used in broadcast studios.

When the AGC circuit is connected in the receive-in line (Figure 11), the AGC1 tends to boost residual echo and background noise. Insertion of this device into the send-in path (AGC2, Figure 11) would be beneficial in protecting the send path from overload by a very loud talker. However, during the double-talk condition, in which the adaptation process in the AFIRF is stopped [4], AGC2 would change the gain in the echo path according to the nearest talker's speech. Since the AEC cannot adapt to this new condition, the AFIRF could generate an echo signal.

This problem can be solved by using two identical gain control devices (AGC2 and AGC3, Figure 9) in the send-in line and AFIRF output. Performance of this circuitry depends on the degree of gain match of the two AGC circuits, which should be at least ± 0.2 dB. Although this gain match was difficult to achieve with analog techniques, the recent development of a digitally controlled precision logarithmic divider IC has helped to solve the problem [11].

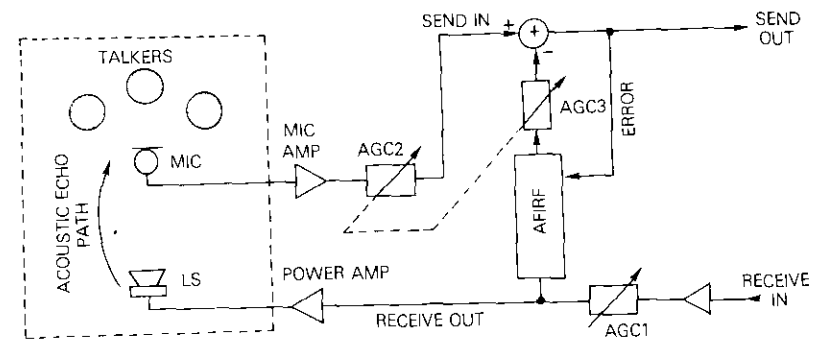


Figure 11. Echo Canceller with Automatic Gain Control Circuits

Conclusion

To test acoustic echo cancellation operationally, several experimental cancellers were built with 5.2-kHz bandwidth, selectable flat delay sections (26 ms), and 768 coefficients h_j . With levels properly adjusted (VU meters at the receive and send inputs), the microphone in a teleconference room could be kept open during a conference without any perception of an echo. In a properly designed room, echo can be attenuated more than 20 dB by the AEC AFIRF, and residual echo can be fully suppressed by a center clipper [4].

Tests performed with this experimental AEC by the author and Onufry [3] have also shown that the AFIRF could significantly reduce the influence of acoustic coupling between a microphone and loudspeakers in a public address system. However, additional research and development are needed in this area.

References

- [1] S. J. Campanella, H. G. Suyderhoud, and M. Onufry, "Analysis of an Adaptive Impulse Response Echo Canceller," *COMSAT Technical Review*, Vol. 2, No. 1, Spring 1972, pp. 1-38.
- [2] O. A. Horna, "Logarithmic Echo Canceller," U.S. Patent No. 4,064,379, December 20, 1977.
- [3] M. Onufry, Private Communication.
- [4] J. G. Brunting et al., "Audio Teleconferencing," U.S. Patent No. 4,237,339, December 2, 1980.
- [5] D. Davis and C. Davis, *Sound System Engineering*, Indianapolis, Indiana: Howard W. Sams & Co., Inc., 1975.
- [6] O. A. Horna, "Echo Canceller With Adaptive Transversal Filter Utilizing Pseudo-Logarithmic Coding," *COMSAT Technical Review*, Vol. 7, No. 2, Fall 1977, pp. 393-428.
- [7] A. Svoboda, "Linear Analyzer in Czechoslovakia" (in Czech), *Czechoslovak Journal for Physics*, Vol. 10, No. 10, October 1951.
- [8] H. Berndt, "Correlation Function Estimation by a Polarity Method Using Stochastic Reference Signals," *IEEE Transactions on Information Theory*, IT-14, November 1968, pp. 769-801.
- [9] O. A. Horna, "Identification Algorithms for Adaptive Filters," *COMSAT Technical Review*, Vol. 8, No. 2, Fall 1978, pp. 331-351.
- [10] O. A. Horna, "Extended Range Echo Cancellers," *Proc. IEEE Southeascon*, Huntsville, Alabama, April 1981, pp. 846-853.
- [11] "CMOS Logarithmic D/A Converter LOGDAC AD 7111," Analog Devices, Norwood, Massachusetts, 1981.

Otakar A. Horna studied at various European Universities and received an M.S. degree in electrical engineering from the Czech Institute of Technology, a Ph.D. in electronics from the Institute of Radio Technique and Electronics, and a State Diploma in Mathematical Logic from Charles University in Prague. He was Senior Scientist and Secretary of the Scientific Council of the Research Institute for Mathematical Machines in Prague in charge of the Computer Technology Division. Later he became Senior Engineer with Multronics Corporation, Rockville, Maryland, where he worked in military electronics. He joined COMSAT Laboratories, Clarksburg, Maryland, in 1969 and is presently a Senior Scientist of the Communications Technology Division.



He is the author of five books, more than 30 U.S. and foreign patents, and numerous scientific and technical articles. His work was awarded with a Gold Medal at the Brussels World Fair in 1958, and a Gold Medal at the Brno Fair in 1967. He received the first COMSAT Research Award for his echo canceller design. He is a Senior Member of IEEE.

Hardware simulation facility for 120-Mbit/s QPSK/TDMA system*

C. BURWELL AND S. GOVER
(Manuscript received July 8, 1982)

Abstract

This paper describes a TDMA system simulation facility (named the INTELSAT TDMA Test Bed) consisting of 120-Mbit/s TDMA terminals and related synchronization equipment, a separate 120-Mbit/s QPSK modem, a transmission path simulator, FEC coding, and a performance measurement system. The terminals, which have numerous variable parameters for experimentation, have been used to examine performance over a simulated INTELSAT V transmission link, which includes an HPA simulator and an INTELSAT V communications transponder simulator. The INTELSAT V simulator has provisions for adjacent channel, co-channel, and satellite multipath interference simulation. The TDMA Test Bed is quite flexible. It has accommodated 120-Mbit/s modem tests in linear and non-linear channels, simulation of earth station equalization for an INTELSAT V link, and transmission with FEC coding. The system characteristics and measurement techniques are described.

Introduction

The INTELSAT TDMA Test Bed (Figure 1) is a simulation facility developed at COMSAT Laboratories to examine 120-Mbit/s TDMA system

*This paper is based upon work performed at COMSAT Laboratories under the sponsorship of the International Telecommunications Satellite Organization (INTELSAT).



Figure 1. *INTELSAT TDMA Test Bed*

operation and transmission system parameters. This facility includes 120-Mbit/s terminals with programmable burst formats and uses several TDMA frame acquisition and synchronization techniques. The terminals have external interfaces for FEC encoders and decoders, space diversity synchronization and switch-over control equipment, open-loop acquisition and synchronization control, frequency-hopping control, and a TDMA performance measurement interface. The simulated transmission path includes an HPA and an INTELSAT V simulator.

The TDMA Test Bed development began in the late 1970's during the development of the INTELSAT V program. The system was designed to allow investigation of possible new parameters for a TDMA system using INTELSAT V and possibly satellites developed later. Factors considered in the studies included the higher modem bit rate resulting from the transponder bandwidth of INTELSAT V being twice that of INTELSAT IV and increased frequency reuse by spatially isolated and dual polarized beams. The resulting co-channel interference effects on TDMA, FEC coding, or space diversity to meet system performance requirements, particularly at 14/11 GHz, and new acquisition and synchronization techniques to improve TDMA performance were also considered. From 1976 through 1980, the separate TDMA subsystems listed in Table I were developed. Descriptions of the TDMA terminals, FEC coding, and space diversity

TABLE 1. TDMA TEST BED SUBSYSTEMS

SUBSYSTEM	MANUFACTURER
120-Mbit/s TDMA Terminals	Mitsubishi Electric Co. (MELCO)
120-Mbit/s QPSK Burst Modem	MELCO
120-Mbit/s FEC Codecs	KDD and Nippon Electric Co. (NEC)
SS/TDMA Acquisition and Synchronization Unit	NEC
TDMA Space Diversity Switchover and Control Terminal	KDD and Fujitsu
Space Diversity Path Simulator	KDD and Fujitsu
120-Mbit/s TDMA Open-Loop Acquisition and Synchronization Unit	COMSAT
TDMA Data Acquisition Unit	COMSAT
Transmission Path Simulator	COMSAT
INTELSAT V Simulator	COMSAT and Ford Aerospace

control subsystems can be found in the literature [1]-[3]. Prototypal TDMA terminals have been subsequently tested over a simulated INTELSAT V transmission link that includes an HPA and an INTELSAT V transponder simulator. The INTELSAT V simulator has provisions for adjacent channel, co-channel, and satellite multipath interference simulation.

System characteristics

The TDMA Test Bed system parameters summarized in Table 2 are

TABLE 2. TDMA TEST BED SYSTEM PARAMETERS

Transmission Bit Rate	120.064 Mbit/s
TDMA Frame	750 μ s
Initial Acquisition Control Frame	2^{17} TDMA frames
Control Signaling Frame	10 TDMA frames
Modulation	QPSK
IF	140 MHz
Steady-State Synchronization Accuracy	± 1 symbol
Acquisition Time (low-level and normal-level fine acquisition)	6 s for global beam loopback; 15 s for spot beam feedback
Fast Reentry (normal-level fine acquisition)	3 s for global beam loopback; 9 s for spot beam feedback
Fast Reentry Accuracy	± 3 symbols
FEC Coding	(128, 112) modified BCH code
Burst Position Control	loopback (traffic station observes own signal), feedback control, and open-loop control with separate synchronization unit
Two Voice Order Wire Channels	32-kbit/s delta modulation
Data Scrambler Polynomial	$x^{15} + x + 1$

based on the INTELSAT prototype TDMA system specification adopted in 1974 with modifications for 120-Mbit/s operation. In addition, provisions for FEC coding, traffic burst synchronization with feedback control, recovered carrier phase ambiguity resolution by unique word detection, frequency hopping, and various system parameter changes were included in the revised INTELSAT TDMA system specification adopted in 1980. In some cases, the TDMA Test Bed implementation of certain parameters is different from that of the revised INTELSAT specification. The TDMA Test Bed modems meet most of the INTELSAT TDMA performance specifications.

TDMA frame and burst formats

The TDMA burst formats shown in Figure 2 are slightly different from those of the INTELSAT TDMA specification adopted in 1974, in that the burst preamble lengths may be varied to examine the carrier synchronization and unique word detection for different QPSK coherence recovery patterns and unique word patterns. One frame marker, or reference burst, is transmitted for each transponder in each 750- μ s frame. The reference burst comprises the QPSK carrier and symbol timing recovery sequence, the unique word, and the station address and status code (SICS). The traffic burst preamble contains the same features as the reference burst plus a control signaling channel (CSC), a teletype order wire channel (TTY), and two voice order wire channels. Each traffic burst has the same unique word, which is different from the reference burst unique word. Because the TDMA terminals do not include provisions for backup reference burst transmission, the reference station status code is fixed.

The CSC is used for reference burst unique word lost and BER detection status, initial frame acquisition and steady-state burst position feedback, relative reference burst time-phase feedback for multiple transponder operation, and voice order wire signaling. The 40-bit CSC word is encoded by a 40-bit BCH polynomial and is transmitted 4 bits per frame multiplexed over the control signaling frame. The control signaling frame consists of 26 information bits, 13 parity check bits, and an uncoded dummy bit. The BCH code for the signaling channel is used only for error detection and is capable of detecting up to 13 consecutive errors or any 5-bit errors in the 40-bit CSC word. The generator polynomial for the BCH code is $g(x) = x^{13} + x^{12} + x^{11} + x^7 + x^4 + 1$. A 10-frame multiframe marker for the control signaling frame is obtained by inverting the bit pattern of the traffic burst unique word when differential encoding is used and by interchanging the P and Q channel bits of the unique word when differential encoding is not used.

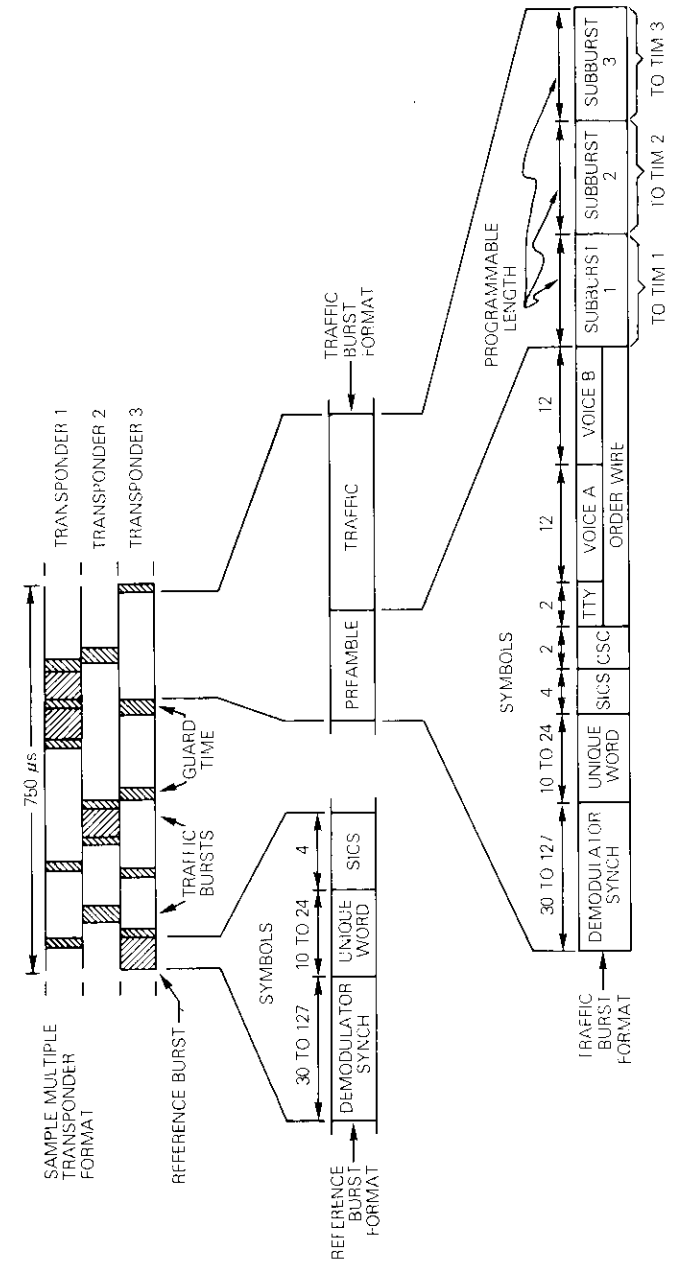


Figure 2. TDMA Burst Formats

Multiple-transponder operation is possible in the test bed (although not actually conducted). Each TDMA terminal is capable of generating a burst for each of three transponders during each frame. When frequency hopping is used, one of the bursts transmitted by each traffic terminal, designated the *master burst*, is used to maintain burst synchronization. If a traffic terminal receives more than one reference burst per frame from the reference station, one of the reference bursts, designated a *master reference burst*, is used to maintain frame synchronization. The assigned burst positions prevent the reception of overlapping bursts at traffic terminals.

TDMA terminals

The TDMA Test Bed has three 120-Mbit/s TDMA terminals. The main traffic terminal performs all the functions usually performed by the common TDMA terminal equipment (CTTE), excluding terrestrial interface bit rate compression and expansion buffers. As many as three terrestrial interface modules (TIMs) may be connected to the main traffic terminal. The monitoring terminal is similar to the main traffic terminal, except that the TIM interface and the space diversity control interface are not available. The monitoring terminal also can control the acquisition and synchronization of the main traffic terminal by feedback control and act as a TDMA traffic terminal with simulated traffic generated by an internal pseudorandom sequence generator. The reference terminal is used only to generate the system reference burst. The characteristics of the TDMA terminals are given in Table 3.

TABLE 3. CHARACTERISTICS OF TDMA TERMINALS

CHARACTERISTIC	MAIN TRAFFIC TERMINAL	MONITORING TERMINAL	REFERENCE TERMINAL
Variable Burst Format	x	x	x
Loopback Synchronization	x	x	
Feedback Synchronization	x		
Open-Loop Synchronization	x	x	
Differential or Absolute Data Encoding	x	x	x
Modem Carrier/Clock Recovery Pattern Length Variable to 127 Symbols	x	x	x
Traffic Burst Unique Word Detected with Variable Bit-Error Tolerance	x	x	
Reference Unique Word Detected with 0-Bit-Error Tolerance	x	x	
Variable Unique Word Pattern (up to 48 bits)	x	x	x

TABLE 3. CHARACTERISTICS OF TDMA TERMINALS (continued)

CHARACTERISTIC	MAIN TRAFFIC TERMINAL	MONITORING TERMINAL	REFERENCE TERMINAL
PN Sequence Initial Acquisition	x		
Pulsed-Carrier Initial Acquisition	x	x	
Open-Loop Initial Acquisition	x	x	
Variable Initial Acquisition Time Slot	x	x	
FEC Codec Connection	x	x	
Space Diversity Control Connection	x		
BER Measurement Using Voice Order Wire Channel	x	x	
Up to 3 Transmitted Bursts	x	x	x
Up to 3 Connectable TIMs	x	x	
$2^{15}-1$ PN Data Scrambler Sequence	x	x	x
Traffic Burst Acquisition/ Synchronization Monitoring		x	
Internal Simulated Traffic		x	
Continuous Clock Frequency Shift up to 2×10^{-7} in Magnitude			x
Digital Clock Frequency Shift up to 9 Symbols per 1000 Frames in Magnitude			x

TDMA modems

The major characteristics of the TDMA modems are given in Table 4. The TDMA Test Bed modems in Figure 3 were originally designed to use channel filters based on the INTELSAT TDMA specification adopted in 1974, that is, a channel filter at the transmitter having a 30-percent cosine roll-off Nyquist response ($BT = 1.0$ for 60.032 Mbaud) with $x/\sin x$ compensation for the $(\sin x)/x$ input spectrum. No presampling receive filter was used. A wideband bandpass filter with flat amplitude and group delay was used at the receiver to reject out-of-band noise and interference. Although these filters are good for minimizing intersymbol interference in a linear channel, using filters with a less sharp roll-off at the transmitter and splitting the channel filtering between the transmitter and the receiver have been shown to give better performance over INTELSAT-type satellite channels [4], [5]. Square-root 40-percent roll-off Nyquist filters for the TDMA modems were subsequently developed by Mitsubishi Electric Co. These filters improved the nonlinear channel performance and

TABLE 4. TDMA TEST BED MODEM CHARACTERISTICS

Bit Rate	120.064 Mbit/s
Symbol Rate	60.032 Mbaud
Modulation	QPSK
IF	140 MHz
Allocated Bandwidth	80 MHz
Carrier Phase Ambiguity Resolution	Unique word detection or differential decoding
Unique Word Error Rate (30-symbol carrier and clock recovery pattern, differential encoding)	Less than 10^{-8} for BER = 10^{-4}
Bit-Error Rate (30% cosine roll-off transmit filters, differential encoding)	Less than 10^{-4} for $E_b/N_o = 10.6$ dB; less than 10^{-6} for $E_b/N_o = 14.6$ dB
Modulator	
Static Phase Balance	$<1^\circ$
Static Amplitude Balance (Magnitude)	≤ 0.1 dB
Carrier Frequency Offset	<1 kHz
Carrier Frequency Stability	1×10^{-7} /day
Carrier on/off Ratio	40-50 dB
Out-of-Band Spurious	<-40 dB
Demodulator	
Demodulation	4-phase coherent detection
AGC Dynamic Range	± 5 dB relative to nominal level
Carrier Frequency Offset	± 50 kHz
Burst-to-Burst Frequency Variation	5 kHz
Burst-to-Burst Level Variation	3 dB
Out-of-Band Rejection	<35 dB for $f_c = 95$ MHz, <35 dB for $f_c = 190$ MHz, adjustable from 30 to 90
Q Factor of Carrier Recovery Tank Circuits	adjustable from 70 to 140

conformed to the revised INTELSAT TDMA specification adopted in 1980. Modem performance measurements were performed over linear and nonlinear channels with both the cosine roll-off and square-root Nyquist channel filters.

The carrier recovery circuit in Figure 4 uses a frequency quadrupler with automatic frequency control and narrow-band filtering [6], [7]. The carrier component at four times the carrier frequency is translated in frequency and passed through a narrow-band filter that is variable in bandwidth from about 666 kHz to 2 MHz (with Q ranging from 30 to 90). The symbol clock recovery circuit in Figure 5 uses the classic half-symbol delay and multiply technique [8].

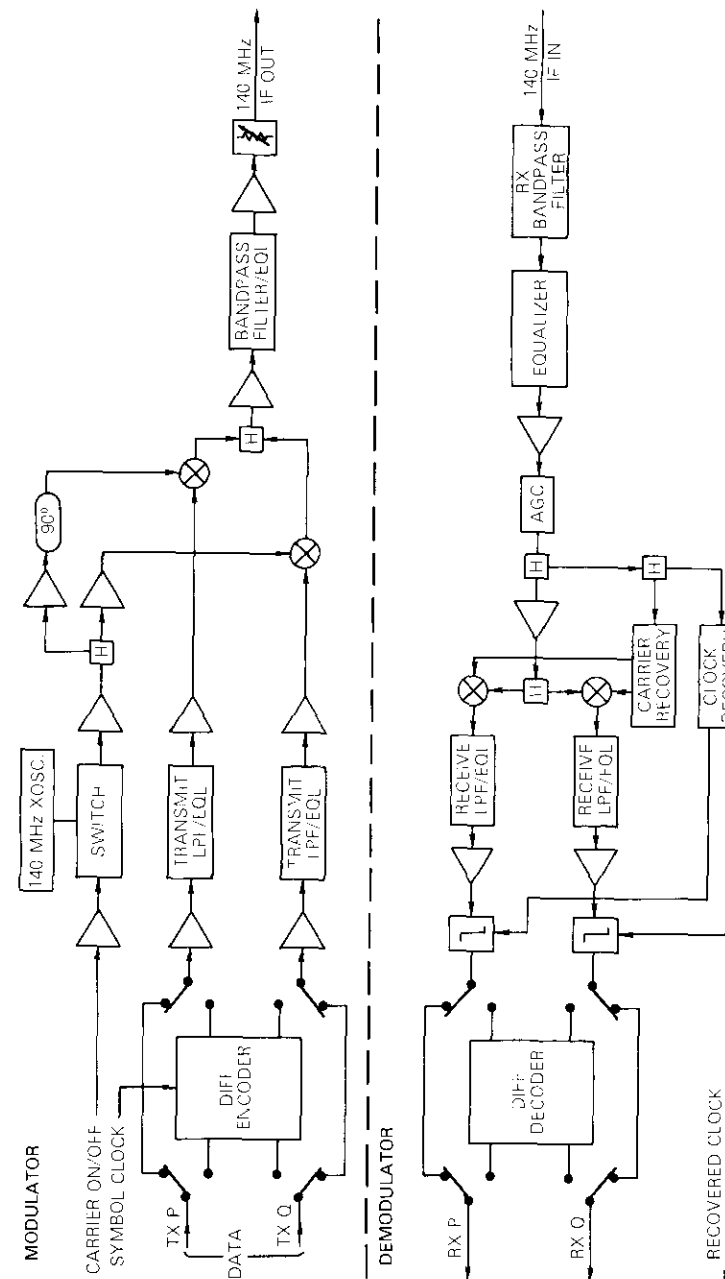


Figure 3. TDMA Test Bed Modems

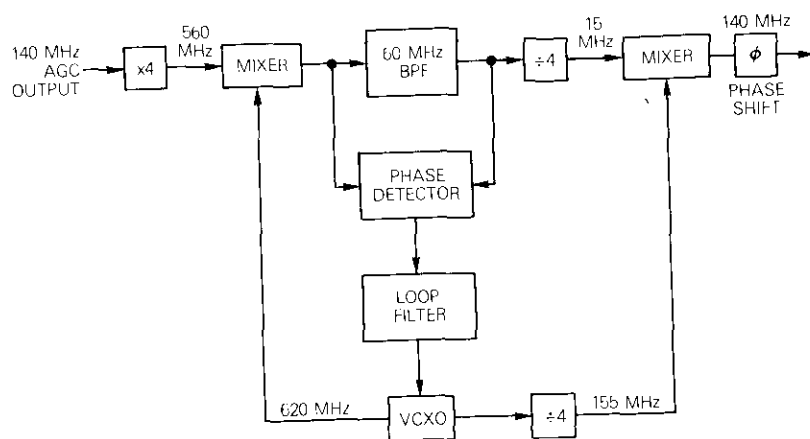


Figure 4. Carrier Recovery Circuit

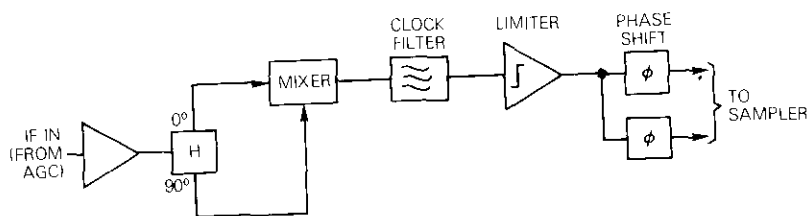


Figure 5. Clock Recovery Circuit

FEC coding

The TDMA Test Bed forward error-correcting (FEC) coding units use a (128, 112) double error-correcting, triple error-detecting code modified from the (127, 113) BCH code by including an additional parity check bit and a single dummy bit in each 128-bit code block. FEC coding is applied to all traffic bursts at the modem bit rate of 120 Mbit/s. The FEC codec design also assumes that traffic is not differentially encoded. Bit-error rate and distribution of error-free interval measurements are performed with this codec connected to the main traffic terminal as shown in Figure 6.

The symbol clock rate at the input and output of the FEC codec are the same. Data rate conversion due to parity bits introduced by the encoder is performed by using an intermittent clock for data to the encoder and from the decoder. Traffic to and from the terrestrial interface buffers is

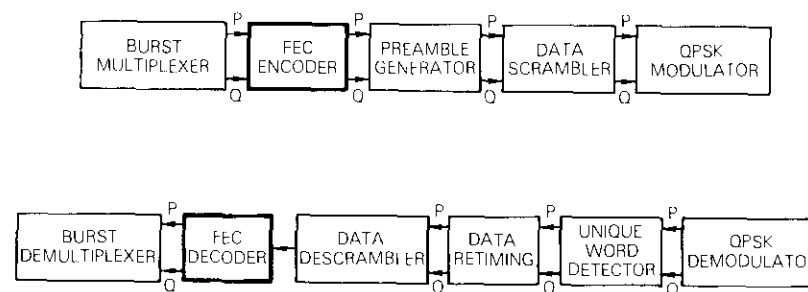


Figure 6. TDMA Terminal Interface for FEC Coding

therefore gated by a window equal to the length of the FEC code block and includes empty spaces for inserted parity bits at the encoder and deleted parity bits at the decoder output.

When interfacing FEC codecs to the TDMA control equipment, the received clock at the input to the FEC decoder must be maintained after the end of the burst to complete the decoding. This is accomplished by retiming the received data with an elastic buffer so that data to the FEC decoder are clocked by a continuous clock synchronous to the local transmit symbol clock.

Data acquisition unit

The data acquisition unit shown in Figure 7 provides automated data collection and test parameter control for measurements on TDMA bursts. Test mode settings on a control panel or CRT display console determine the type of measurement performed. Control signals from the TDMA terminal, along with a microcomputer-controlled measurement system, are used to collect the test data. The recorded data then go to a printer, or as an option, the data may be processed and plotted with the Tektronix 4051 graphic display system.

Burst mode measurements may be performed by observing looped-back TDMA bursts at the terrestrial interface port of the main traffic terminal. Timing signals from the TDMA terminal are used to synchronize the transmitted and received test patterns and to demultiplex appropriate parts of a burst. The PN generator in the data acquisition unit may be configured in the same manner as the built-in PN generator of the monitoring terminal, so that BER measurements may be performed on the link from the monitoring terminal to the main traffic terminal.

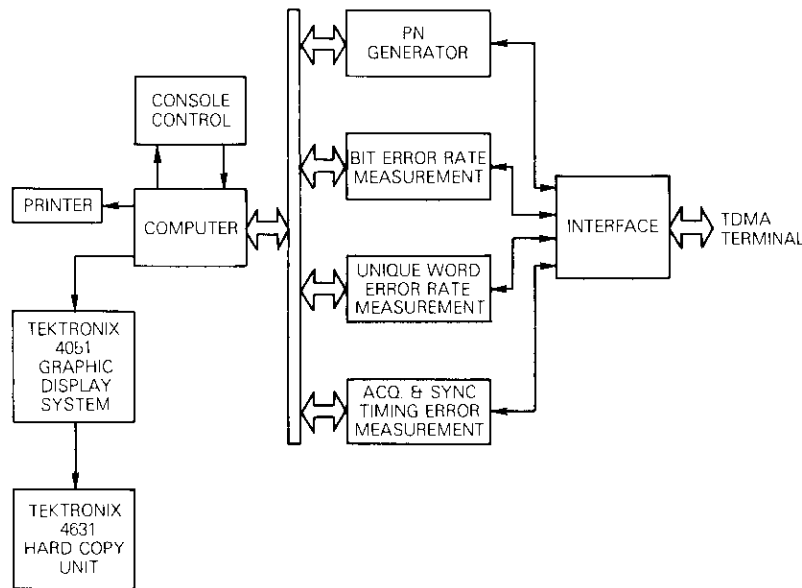


Figure 7. Data Acquisition Unit

BER and distribution of error-free interval measurements may be performed on any contiguous group of symbols within the traffic portions of a burst. A pulse occurring for each unique-word-missed detection is available directly from the TDMA terminal for unique word error rate measurements. Receive frame timing information and traffic burst unique word detection signals from the TDMA terminal may be used to determine the position error of each received traffic burst.

IF transmission path

The IF path unit adjusts the levels and combines the transmit outputs of the TDMA modems. The 140-MHz IF signals are either connected to the RF transmission path or looped back to the demodulators. The IF path also contains a wideband noise generator and dispersed-carrier generator for performing carrier-to-noise ratio measurements. A pseudorandom data generator provides a source that can be modulated and used as co-channel or adjacent channel TDMA interference. The modulated pseudorandom data are sent to up-converters tuned to satellite channel frequencies adjacent to the TDMA channel when TDMA adjacent channel interference is simulated. The modulated pseudorandom data can also be

combined with the TDMA signals at IF for TDMA co-channel interference simulation.

RF transmission path

The RF path setup is designed to facilitate the testing of TDMA signal transmission via a simulated INTELSAT V environment. The required test conditions include the following:

- a. variable signal levels and nonlinear amplifier backoff;
- b. up- and down-link thermal noise;
- c. three co-channel and two adjacent channel interferers;
- d. reception of TDMA bursts from different transponders;
- e. equalization of the up- and down-links and of the satellite filters.

The equalization of the up- and down-links was designed to meet the INTELSAT TDMA specification (see Figures 8a and 8b). INTELSAT had not yet specified the equalization requirements for the satellite filters when the INTELSAT V transponder filter equalizers were designed. The design of the link equalization was a compromise between feasibility and improvement in performance.

RF transmission path simulation

The RF path simulation setup described in Figure 9 consists of the following main parts:

- a. INTELSAT V simulator,
- b. interface section,
- c. HPA simulator,
- d. interferers.

The INTELSAT V simulator consists of RF hardware (e.g., TWTAs, input multiplexer, and output multiplexer) identical to the hardware used in the actual INTELSAT V communications subsystem.

The interface section is used to connect the TDMA IF signal to the INTELSAT V simulator. This section includes a long coaxial cable for the TDMA modem IF signal. The cable connects two remote parts of the COMSAT Laboratories building, in which the TDMA Test Bed facility and the INTELSAT V simulator are located. The interface section also includes all the fixed-amplitude and group delay equalizer sections required for compliance with the link equalization specifications. Variable transversal type equalizers were also used for fine tuning. A 140-MHz to 6-GHz up-

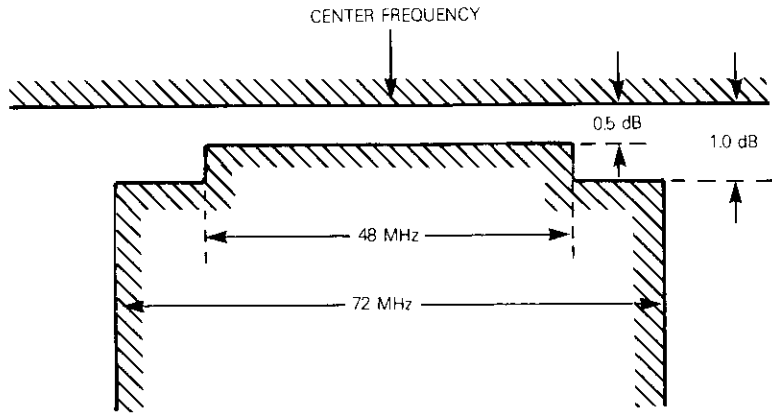


Figure 8a. INTELSAT TDMA RF Link Amplitude Response Limits

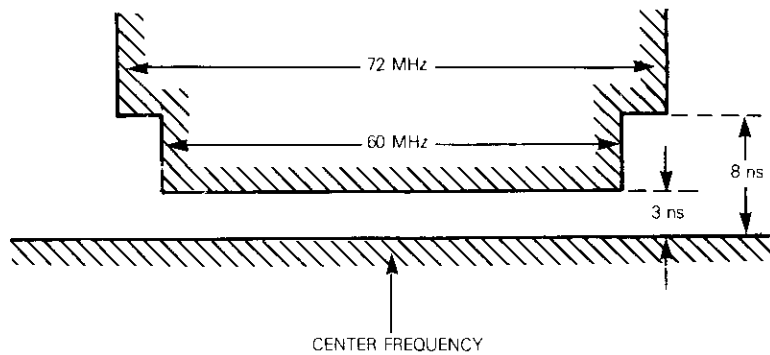


Figure 8b. INTELSAT TDMA RF Link Group Delay Response Limits

converter and 4-GHz to 140-MHz down-converter at the satellite output were also part of this section. Dual up- and down-converters with a switching capability between the two sets can be used for simulation of transponder hopping. When transponder hopping is used, each converter should be equalized separately.

The HPA simulator uses a 50-W helix TWTA located close to the INTELSAT V simulator.

The interferers are co-channel and adjacent channel TDMA types and can be coupled with FDMA/FM interferers.

The link amplitude and group delay response vs frequency are shown in Figures 10 and 11.

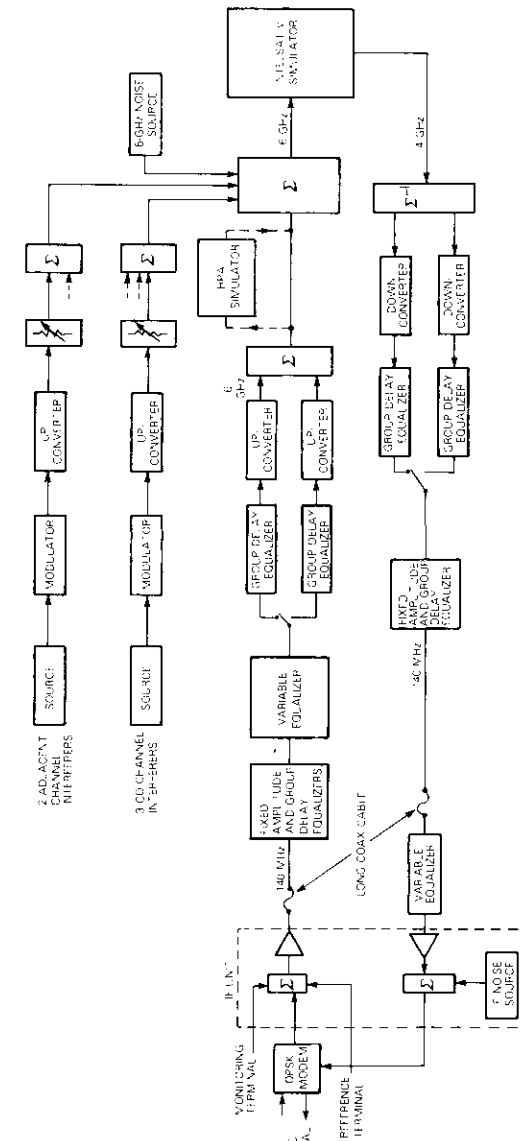
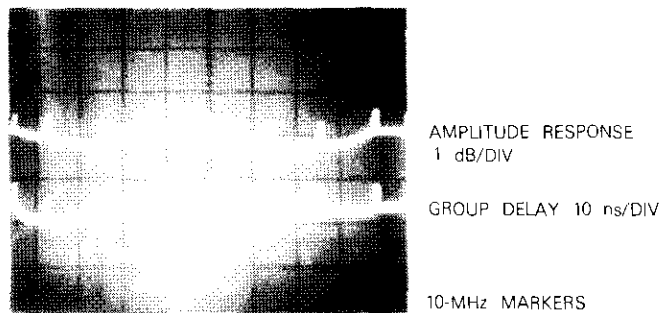
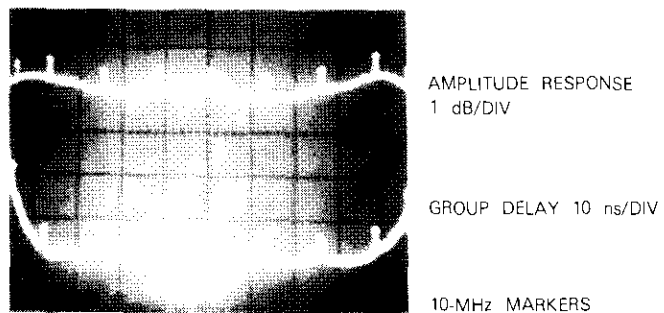


Figure 9. RF Path Simulator



a. FROM MODULATOR TO HPA OUTPUT



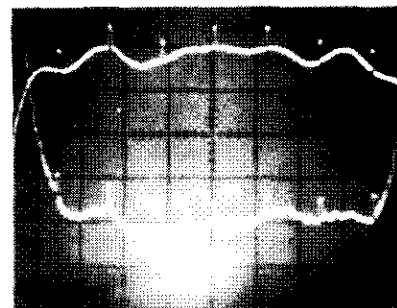
b. FROM MODULATOR TO SATELLITE TWTA INPUT INCLUDING INPUT MULTIPLEXER

NOTE: HPA SET AT 14-dB INPUT BACKOFF

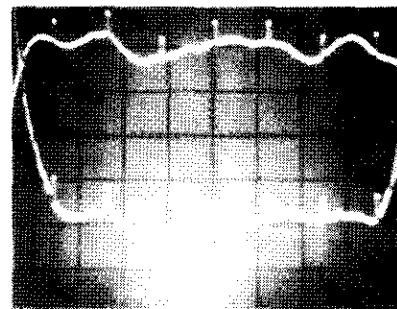
Figure 10. *Up-Link Response*

Synchronization techniques

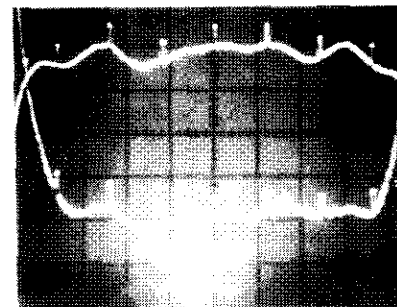
The TDMA Test Bed can simulate a 3-terminal TDMA network using either global beam loopback or spot beam feedback synchronization. The TDMA Test Bed operating as a global beam system simulates a reference station and two traffic terminals operating in a global beam transponder. Frame acquisition and synchronization at the traffic terminals are performed by each terminal observing the traffic burst from its own terminal looped through the satellite transponder. The traffic burst transmission



a. HPA AND TWTA AT SATURATION



b. HPA AND TWTA AT 14-dB INPUT BACKOFF



c. HPA AT 10-dB INPUT BACKOFF TWTA AT 2-dB INPUT BACKOFF

Figure 11. *RF Loop Response*

time is adjusted to maintain the looped-back received traffic burst in a fixed position with respect to the received reference burst. The TDMA Test Bed operating as a spot beam system shown in Figure 12 simulates a reference burst transmitted to two transponders with one transponder as a loopback transponder, allowing a traffic terminal to receive its own

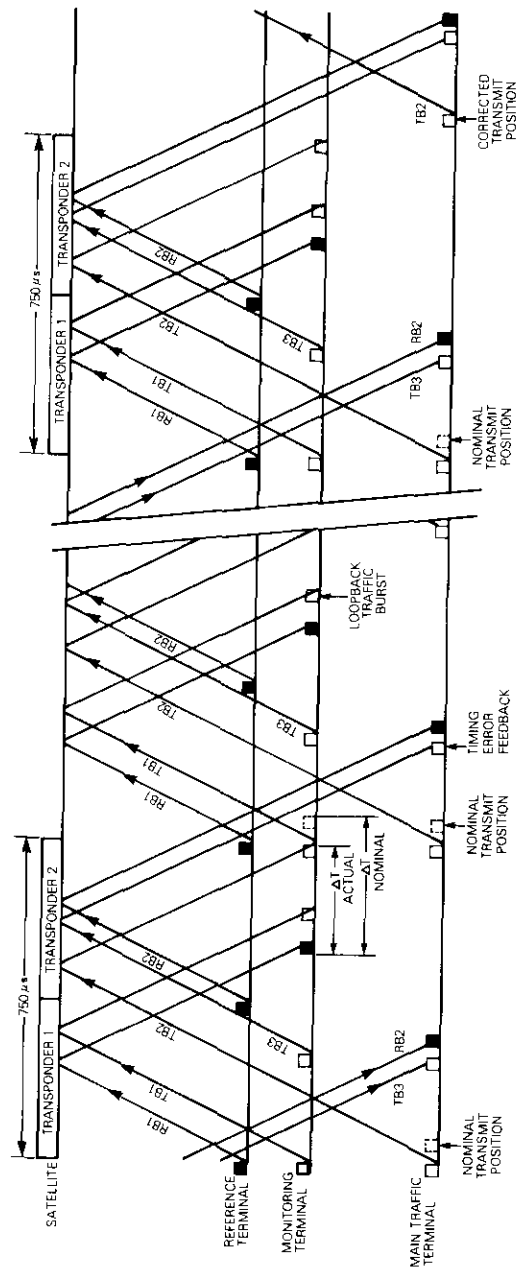


Figure 12. TDMA Network with Feedback Synchronization

transmitted bursts. The traffic terminal operating in the loopback transponder (monitoring terminal) acquires and maintains synchronization by using the global beam synchronization technique. The traffic terminal using the other transponder (main traffic terminal) cannot observe its own transmitted bursts (as is the case with INTELSAT V hemi and zone beam transponder operation) and hence requires an assisting station in the beam coverage area of the traffic burst destination to monitor its burst position and return a transmit burst position delay number via the feedback control signaling channel. TDMA synchronization with multiple spot beam transponders may be simulated with one transponder by programming the receive burst format of the traffic terminal to detect only the bursts from the desired transponder.

An external synchronization unit may be used to provide open-loop synchronization control for the traffic terminals. Under open-loop control, the open-loop acquisition and synchronization logic unit (OASLU) receives the burst transmission timing error that represents satellite ranging data from the two TDMA traffic terminals. Data from a third ranging station may be simulated in software by using a microprocessor associated with the OASLU. The OASLU then uses the 3-station ranging data to compute a transmit burst position delay number for each traffic terminal. An external transmit frame reference signal representing the relative burst position delay in the TDMA frame is sent to each traffic terminal from the OASLU. Under open-loop synchronization control, the traffic terminal burst position control logic normally used for closed-loop acquisition and synchronization can be easily bypassed by modifying the traffic terminal software. In this system, the software changes consist mainly of bypassing unused sections of the control program.

TDMA synchronization in a system with satellite-switched up-link to down-link transponder connectivity (*i.e.*, SS/TDMA), which may be used with the INTELSAT VI satellite, can be tested in part by using additional control equipment to synchronize TDMA frames to the transponder connectivity. A simplified test configuration for SS/TDMA synchronization is shown in Figure 13. A separate acquisition and synchronization unit (ASU) is used to control the frame period acquisition and synchronization of the TDMA terminals. The ASU uses the synchronization window synchronization technique in which a time slot, called the synchronization window, is available for ASU loopback transmission, so that the ASU can synchronize with the switch states of the transponder switching matrix on board the satellite [9]. The synchronization window and the loopback traffic interval are distinguished by their different durations.

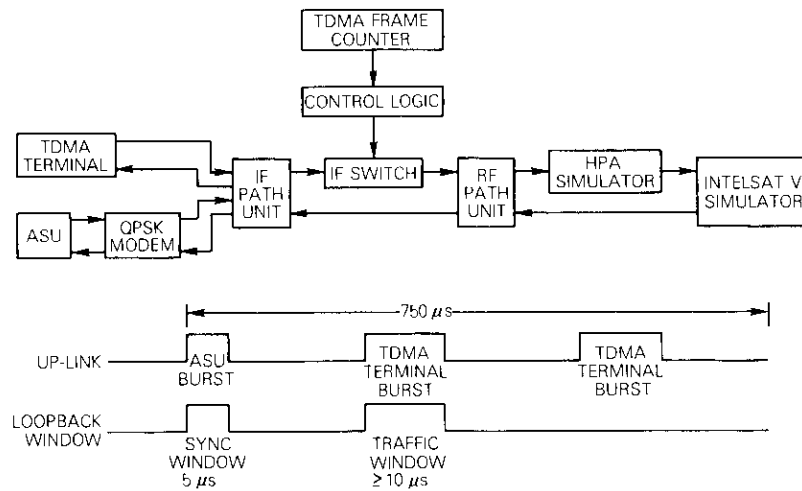


Figure 13. *Simplified SS/TDMA Synchronization Test Configuration*

The ASU detects its own transmitted bursts (metering bursts) and transmits a reference burst to each transponder. Any of the initial acquisition techniques available can be used because the ASU simply replaces the reference station. Synchronization to switching on board the satellite is simulated with an IF switch controlled by a TDMA frame counter, which generates timing for traffic windows and synchronization windows. The receive burst format of each traffic terminal is programmed to simulate spot beam operation.

Initial acquisition techniques

The acquisition control frame of 2^{17} frames is divided into 32 (*i.e.*, 2^5) identical time slots of 4,096 (*i.e.*, 2^{12}) frames each. Simultaneous acquisition attempts are avoided by having each TDMA traffic terminal perform initial acquisition within a unique preassigned interval by using an acquisition window of 3,699 frames for loopback control and 7,995 frames for feedback control.

The TDMA frame acquisition process consists of a coarse acquisition process and a fine acquisition process. In the coarse acquisition process, the burst transmission time relative to the received reference burst is determined within $\pm 4 \mu\text{s}$. This phase of the acquisition process uses a low-level acquisition signal significantly below the TDMA signal level, so that interference to any TDMA burst is negligible. The fine acquisition process determines the burst transmission time within ± 3 symbols rela-

tive to the received reference burst by adjusting the transmitted position of a burst consisting of only the preamble. The fine acquisition process is referred to as fast reentry acquisition, because this acquisition process is also used when the traffic terminal bypasses low-level acquisition and goes immediately to the fine acquisition process after traffic burst synchronization has been temporarily lost. The traffic burst position is expected to be within $\pm 4 \mu\text{s}$ of the assigned burst position when fast reentry acquisition takes place.

Initial frame acquisition for the main traffic terminal is performed with either PN sequence correlation or pulsed-carrier detection [8], [10]. The monitoring terminal acquires the TDMA frame by using only the pulsed-carrier acquisition technique. However, this terminal can assist the acquisition of the main traffic terminal and an additional traffic terminal by using either the pulsed-carrier or PN sequence correlation technique. In either acquisition technique, the transmitted signal strength is 20 to 30 dB less than the TDMA burst carrier level, so as not to degrade normal TDMA burst transmission. The IF acquisition signal with a frequency of 129.388 MHz is offset from the TDMA IF signal and is detected by a separate acquisition modem.

With pulsed-carrier acquisition, the acquiring station transmits one 6.2- μs carrier pulse per frame and, by shifting the transmitted pulse position 16 symbols each frame, sweeps the carrier pulse entirely across the frame. In a global beam system, the acquiring station opens a window during the assigned burst transmission slot and starts counting TDMA frames from the instant the swept carrier pulses are transmitted. The frame counter is stopped when the swept carrier pulse is detected within the window of the assigned burst position. The number in the frame counter, with a possible offset to account for the round-trip propagation delay, determines the acquired burst transmission time. In a spot beam system, the monitoring terminal determines the time of the received acquisition signal with respect to the received reference burst with the PN sequence or pulsed-carrier acquisition technique and sends the timing error to the acquiring station via the traffic burst control signaling channel. A 3-ms carrier pulse is transmitted by the acquiring station immediately preceding the narrow swept carrier pulses to allow the assisting station to determine the initial time of the swept carrier pulses. The acquisition receiver then starts counting the 6.2- μs swept carrier pulses immediately after detecting the wide carrier pulse. The acquisition signal is considered present if it is detected 14 times in 20 or less consecutive frames.

In the PN sequence correlation acquisition technique, a PN sequence is

transmitted at 170.66 kbit/s by the acquiring station, and biphas PSK is used. The acquisition signal is differentially demodulated and correlated with a local PN sequence, and a delay-locked loop detector determines the timing error. The characteristics of the PN acquisition modem are shown in Table 5, and the format of the PN acquisition signal is shown in Figure 14.

TABLE 5. CHARACTERISTICS OF PN SEQUENCE ACQUISITION

Acquisition Signal	$2^7 - 1$ PN sequence and all-zero pattern
PN Generator Polynomial	$x^7 + x + 1$
Acquisition Signal Bit Rate	170.66 kbit/s (352 TDMA symbols per PN code symbol; 320 TDMA symbols for acquisition all-zero pattern)
Modulation	2-phase PSK + CW for PN 0 phase
Signal duration	
CW Signal	1,200 TDMA frames
PSK Signal	2,499 TDMA frames
Carrier on/off Ratio	≥ 35 dB
Demodulator AGC Range	± 5 dB
PSK Demodulation	Differential detection
AFC Capture Range	± 50 kHz from nominal
Correlation	Baseband delay-locked loop
Burst Position Data Resolution	16 symbols

Fast reentry and steady-state synchronization

When the low-level acquisition process is complete, the traffic burst preamble is transmitted. In this fine acquisition process, called fast re-entry acquisition, the burst position error of the preamble burst is measured by the acquiring station in loopback operation and by the assisting station in feedback operation. The burst position is corrected at a rate of 1 symbol per frame for each burst position correction interval until the burst position is within ± 3 symbols of the assigned position, at which time the fine acquisition process is complete, and the traffic part of the

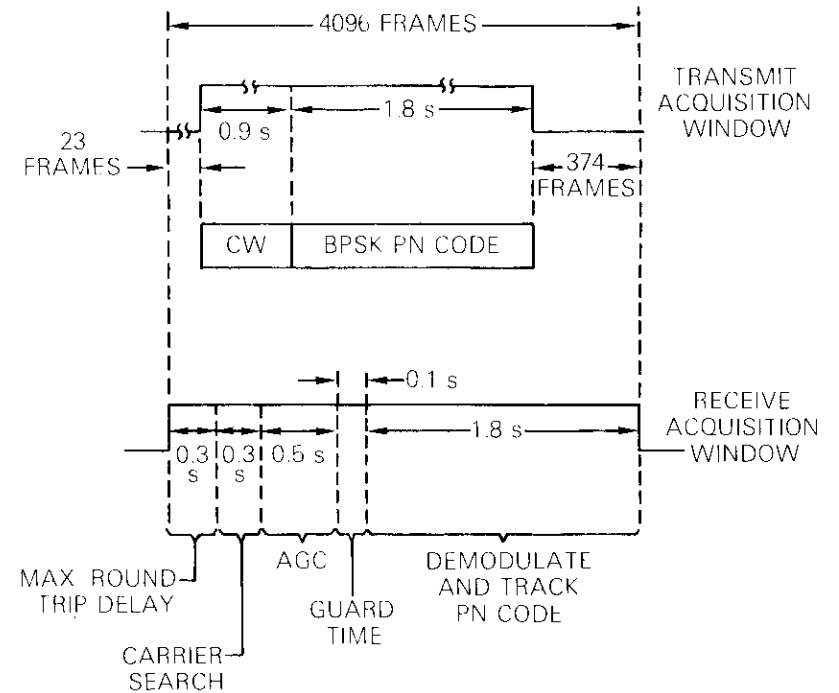


Figure 14. PN Acquisition Signal Format

burst is transmitted. Correction of the traffic burst position continues at a rate of 1 symbol per frame for each burst position correction interval to maintain the burst position within ± 1 symbols of nominal. The burst position correction interval consists of the round-trip propagation time (assumed to be 300 ms for loopback synchronization and 600 ms for feedback synchronization) plus the time to detect and average the burst position error of 256 received traffic bursts. The TDMA terminals may use internal timing for a short time and synthesize a unique word detection pulse if the true unique word of the TDMA burst is not detected. The traffic bursts detected with internal timing of the TDMA terminal are not used in the determination of the average burst position error.

Phase ambiguity resolution and multiframe synchronization

When differential encoding and decoding are used, the phase changes

are transmitted and differentially decoded after coherent detection, and the phase changes are, of course, invariant to the actual recovered carrier phase. When differential decoding is not used (*i.e.*, with CPSK), the four-fold ambiguity at the demodulator output must be resolved by some other means, such as unique word detection. That is, if the P and Q channel data to the modulator represented by the ordered pair (P,Q) are transmitted, the possible outputs of the demodulator are (P,Q), (Q,P), (\bar{P},\bar{Q}), and (\bar{Q},\bar{P}), where \bar{P} and \bar{Q} are the modulo-2 complement of the data on P and Q channels, respectively. Thus, the P and Q channel data at the input to the unique word detector may be inverted or interchanged (or both) from the transmitted data. The phase ambiguity of a fixed unique word can be removed by a unique word detector containing two correlators matched to the (P,Q) and (\bar{Q},\bar{P}) unique words, and four threshold detectors for deciding whether the true or inverted unique word pattern is received either in-phase or in phase-quadrature to the transmitted pattern.

The CPSK traffic burst control signaling channel data are transmitted in a 10-frame multiframe identified by detecting the unique word (Q,P), which is the traffic burst unique word (P,Q) with the unique word symbols on the P and Q channels interchanged. When differential encoding is used, the multiframe unique word is the inverted unique word (\bar{P},\bar{Q}). However, this technique is not used in the case of CPSK because the inverted unique word is one of the ambiguity states. The alternate unique word (Q,P) gives four different ambiguity states (Q,P), (P,Q), (\bar{Q},\bar{P}), (\bar{P},\bar{Q}), which can be resolved by a unique word detector, as shown in Figure 15, to obtain the multiframe timing.

The reference unique word is periodically altered in the same manner as the traffic burst unique word to obtain the multiframe timing for initial acquisition. The separate reference unique word detector is similar to that for the traffic burst, except that no errors are allowed in the reference burst detection.

BER and error-free interval measurements

Measurements at terrestrial interface module simulator

The bit-error rate with FEC coding is conveniently measured at the terrestrial interface module (TIM) interface. A data generator and error detector are used in place of an actual TIM. A switch on the panel of the FEC decoder card can be used to manually enable and disable error correction without physically changing the test configuration. In this case, the time intervals for inserted parity check bits are always included in the

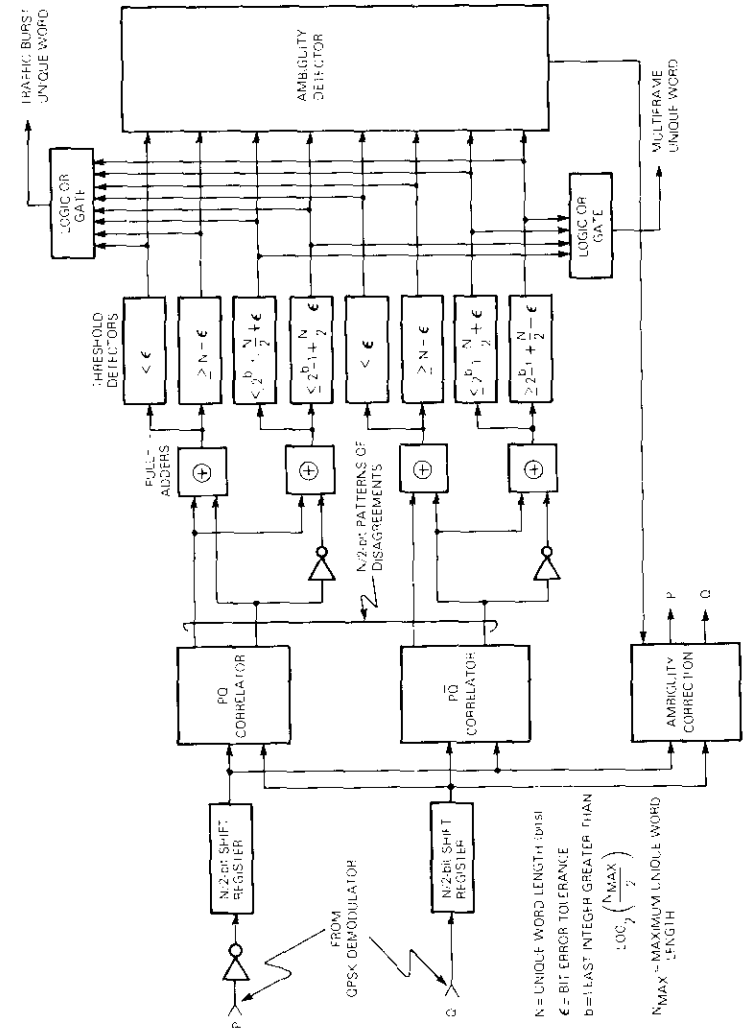


Figure 15. Unique Word Detector and Ambiguity Resolver for Variable-Length Unique Word

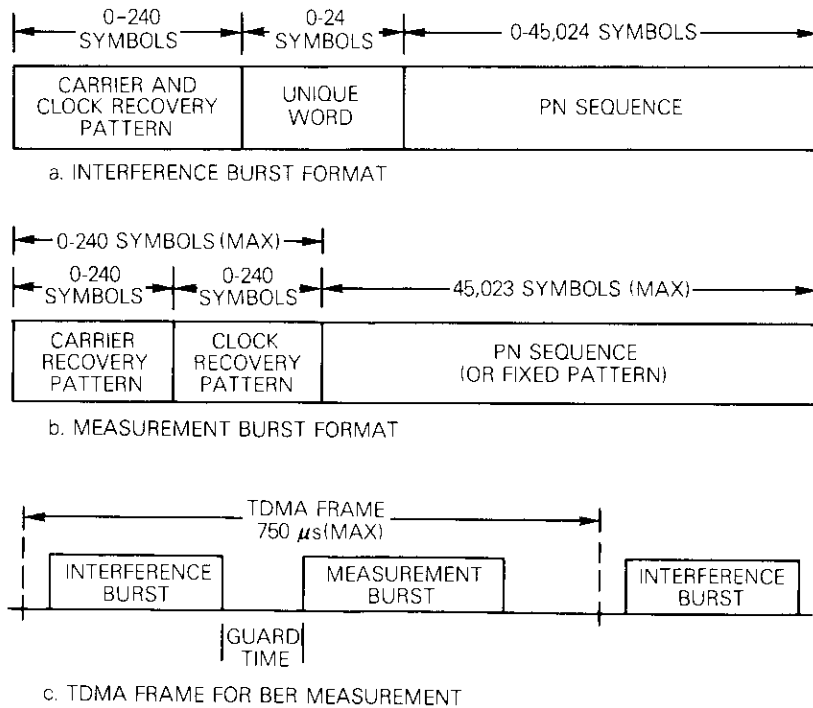


Figure 17. Burst Formats for Measurements at Modem Interface

ference burst. The coherence recovery patterns of all logic 1's, or alternating 1010 . . . , which are optimum for symbol timing recovery for differential and absolute encoding, respectively, are available for each burst. A preamble with an optimum QPSK carrier recovery pattern followed by an optimum clock recovery pattern is available for the BER measurement burst.

The measurement burst recovered carrier phase ambiguity is resolved by differential encoding and decoding.

A measurement window variable in length and position allows burst mode BER measurements on any section of the measurement burst. The transient BER during the unique word portion of the TDMA burst for different coherence recovery pattern lengths can therefore be easily measured. The amplitude balance of a QPSK modulator can also be measured for the interference burst or the measurement burst.

Order wire BER measurements

BER in the range 10^{-3} to 10^{-6} may be measured on the unused TDMA voice order wire channels. The main traffic terminal displays the 5-min. averaged BER on a display panel, and both the 5-min. averaged data and the 30-min. averaged data may be measured and stored for 2 days. The BER data stored in memory are available for printout at a test unit interface.

Unique word detection measurements

The probability of missed-unique-word detection, $P[\text{UW miss}]$, is given by

$$P[\text{UW miss}] = \sum_{i=E/2+1}^N \binom{N}{i} (\text{BER})^i (1 - \text{BER})^{N-i};$$

differential encoding

and

$$P[\text{UW miss}] = \sum_{i=E+1}^{2N} \binom{2N}{i} (\text{BER})^i (1 - \text{BER})^{2N-i};$$

CPSK

where N = unique word length in symbols
 E = bit-error tolerance
 BER = bit-error rate, including cycle skipping.

The number of unique-word-missed detections in 10^6 frames can be measured for the traffic burst or the reference burst from signals directly available from the TDMA terminals. Unique word detection measurements are most conveniently made by operating the TDMA terminals under open-loop synchronization control, so that TDMA bursts are always transmitted, regardless of the number of unique-word-missed detections. With open-loop control, false unique words can be measured by moving the transmit frame reference so that the received burst position is just outside the window normally used for detection of the unique word correlation pulse. Any correlation pulse within the unique word detection window is then a false detection.

Acquisition and synchronization measurements

The timing error of the low-level initial acquisition process is obtained by measuring the location of the initial acquisition detection signal with respect to the nominal traffic burst position. These data can be obtained

with an external counter. However, the acquisition timing error data are also stored in the memory of the control logic unit of the TDMA terminal at the end of the low-level acquisition process. The acquisition data in storage may be accessed by a peripheral device by manually interrupting the normal operational flow of the control program. Burst synchronization timing errors are obtained by measuring the location of the unique word with respect to its nominal position for each frame. The distribution of the synchronization timing errors is measured by counting the number of bursts received at each position within the unique word detection window over a 1,000-frame interval. Synchronization timing is also displayed on the front panel of the TDMA terminals, where the average burst position error during the burst position correction period is shown.

Signals are also available from the TDMA terminals for determining the acquisition time for the low-level and fast reentry acquisition processes. These signals may be used with external counters to determine the number of missed and false acquisition detections.

Conclusions

The TDMA Test Bed, as currently configured, can be used to support experiments in such areas as modem performance testing, INTELSAT V TDMA system simulation, and TDMA synchronization studies. The techniques for performing bit-error rate, unique word error rate, and synchronization performance measurements were discussed. Some features that may be used in future INTELSAT TDMA systems, such as frequency hopping and 14/11-GHz operation, were not implemented in this system.

A number of features in the INTELSAT TDMA system specification adopted in 1980, such as FEC coding and the RF system parameters, have been examined with this system and the simulated INTELSAT V satellite link.

References

- [1] Y. Umeda, T. Fujino, and H. Ito, "120 Mbps TDMA Terminal Equipment," *Proceedings*, Pacific Telecommunications Conference, 1981, pp. C2-34-C2-41.
- [2] T. Muratani et al., "Application of FEC Coding to the INTELSAT TDMA System," *Proceedings*, Fourth International Conference on Digital Satellite Communications, October 1978, pp. 108-115.
- [3] T. Watanabe, H. Saitoh, A. Ogawa, and J. Deal, "Space Diversity System for TDMA Satellite Links," *Proceedings*, Fourth International

- Conference on Digital Satellite Communications, October 1978, pp. 319-326.
- [4] C. Devieux, Jr., and M. E. Jones, "A Practical Approach for QPSK/TDMA Satellite Channel Filtering," *IEEE Transactions on Communications*, COM-29, No. 5, May 1981, pp. 556-566.
 - [5] L. Lundquist, M. Shum, and S. Fredricsson, "Pulse Shaping in Band-limited Digital Satellite Systems," *IEEE Transactions on Communications*, COM-26, No. 4, April 1978, pp. 478-484.
 - [6] C. J. Wolejsza and D. Chakraborty, "TDMA Modem Design Criteria," *COMSAT Technical Review*, Vol. 9, No. 2A, Fall 1979, pp. 413-464.
 - [7] M. Asahora et al., "Analysis of Carrier Recovery Adopting a Narrow-Band Passive Filter with AFC Loop," *Proceedings*, Third International Conference on Digital Satellite Communications, November 1975.
 - [8] J. J. Spilker, *Digital Communications by Satellite*, Englewood Cliffs, New Jersey: Prentice-Hall, Inc., 1977.
 - [9] R. A. Rapuano and N. Shimasaki, "Synchronization of Earth Stations to Satellite Switched Sequences," AIAA 4th Communications Satellite Systems Conference, Washington, D.C., 1972.
 - [10] H. Kurihara, A. Ogawa, and Y. Hirata, "A New Initial Acquisition Technique for PCM-TDMA Satellite Communication System," *Proceedings*, Third International Conference on Digital Satellite Communications, November 1975.

Appendix A. Determination of energy to noise ratio E_b/N_o

The bit energy to noise density ratio (E_b/N_o), which cannot be measured directly, is obtained from the expression

$$E_b/N_o = C/N \cdot B_n/R \quad (\text{A-1})$$

where

C = signal power

N = noise power in the bandwidth B_n

R = modulation bit rate (twice the symbol rate for QPSK).

The ratio C/N can be measured, and B_n/R is determined by the system parameters. For C/N measurements, the following statements should be considered (see Figure A-1):

- a. In the measurement of the signal power for an RF link at the demodulator input, the measured quantity includes the system noise N_s , which is

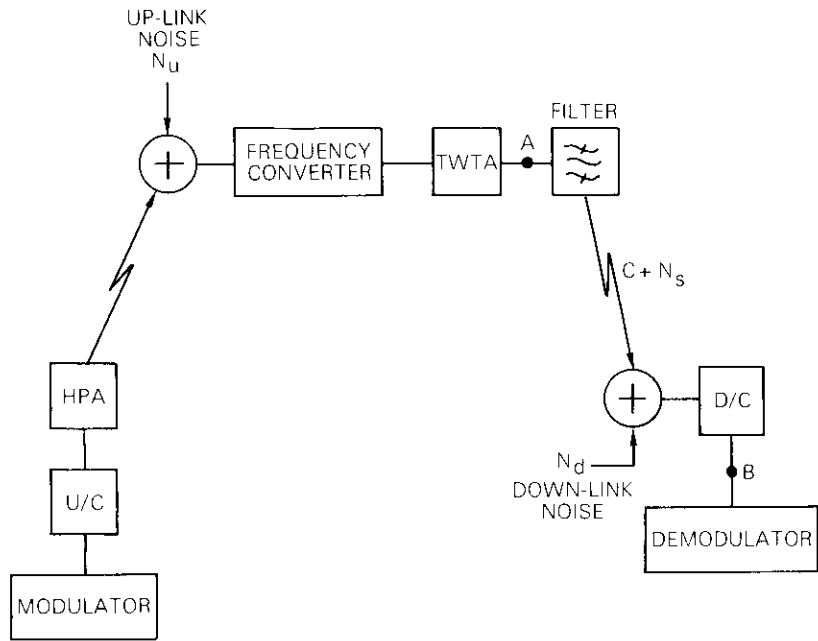


Figure A-1. Simplified RF Link

essentially the up-link noise (N_u) amplified by the satellite amplifiers and filtered. Because of the TWTA nonlinearity, this noise is signal-level dependent.

b. The measured signal power is different for modulated and unmodulated signals, mainly because of spectrum truncation by the system filters.

Several methods can be used to overcome the first difficulty [A-1]. All of them involve loading the link with a carrier and measuring the system noise vs carrier level while separating the noise from the carrier by filtering. The three possible filtering methods, namely offset carrier injection with center frequency bandpass filtering, offset bandpass filtering, and notch filtering, are shown in Figure A-2a, A-2b, and A-2c, respectively.

Each of the two alternatives for signal power measurement has its own advantages. Modulated carrier measurement obtains the real power level of the signal at the demodulator input, so that a real comparison with an ideal PSK demodulator can be made. On the other hand, the most important limiting resource in the satellite link is the saturated TWTA power. For that reason, the reference for a real comparison of BER performance for different transmission parameters (e.g., different filtering and different TWTA backoffs) should be the TWTA output (point A in Figure A-1) power and not the filtered signal at any point beyond that, where spectrum truncation might have

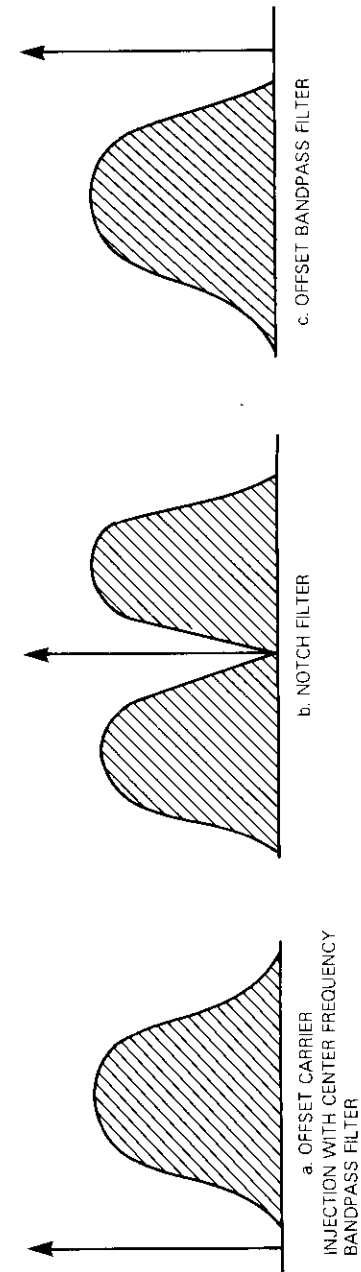


Figure A-2. Noise Measurement Methods for a Nonlinear Channel

taken place. Point A is not a convenient point for measurements because noise can be measured only at point B. A convenient way to overcome this difficulty is to use an unmodulated carrier power level, measured at point B, as an approximate measure of real signal power.

In the system described, offset carrier injection with center frequency bandpass filtering was used for noise measurement, and an unmodulated carrier was used for signal power measurement.

Reference

- [A-1] R. A. Harris, "Performance Criteria for Satellite Digital Transmission Systems," *ESA Journal*, Vol. 1, 1977, pp. 71-85.

Appendix B. Constant number and constant interval BER

The bit-error rate measurement made by observing a fixed number of errors is called the constant number BER measurement. In terms of N BER samples, the average constant number BER can be easily shown to be

$$\text{BER} = \frac{N}{\sum_{i=1}^N 1/(\text{BER})_i}$$

where $(\text{BER})_i$ is the i th sample of the bit-error rate. For QPSK, N includes the combined BER samples on P and Q channels.

The constant interval BER is obtained by observing the number of errors in a fixed time interval and is obtained from N BER samples by

$$\text{BER} = \frac{1}{N} \sum_{i=1}^N (\text{BER})_i$$

BER measurements at the TIM simulator and order wire BER measurements are performed by the constant interval method. BER measurements at the modem interface can be performed with either the constant number or constant interval method.

Clyde Burwell received B.S. and M.S. degrees in Electrical Engineering from The George Washington University in 1975 and 1982, respectively. Since joining COMSAT in 1975, he has been a Member of the Technical Staff in the Multiple Access Department where he was responsible for the system integration of the INTELSAT TDMA Test Bed and the development of TDMA performance test equipment. He has conducted TDMA system simulation experiments and also has been engaged in the design of TDMA terminals and digital transmultiplexers. He is a Member of IEEE.



Shabtai Gover received B.Sc. and M.Sc. degrees in Electrical Engineering from the Technion, Israel Institute of Technology, Haifa, Israel, in 1967 and 1976, respectively. Since 1967, he has been with the Armament Development Authority, Israel, working on the development of communication systems. During the years 1979 through 1981, while on a sabbatical leave from his job in Israel, he was an INTELSAT Assignee at COMSAT Laboratories in the Systems Simulation Department of the Transmission Systems Laboratory, where he worked on various projects involving the simulation of TDMA and FDMA transmission systems.

Experimental evaluation of adaptive threshold detection with estimated sequence processor performance*

D. CHAKRABORTY AND J. M. KAPPES

(Manuscript received June 22, 1982)

Abstract

The potential advantage of the 60-Mbit/s adaptive threshold detection with estimated sequence (ATDES) processor in improving the nonlinear channel performance of QPSK satellite communications has been demonstrated with an actual satellite configuration. The net improvement in a nominally equalized QPSK channel is about 2 dB at an error rate of 10^{-6} with the transponder operating at saturation and with the HPA operating in a linear region. The ATDES distortion memory is capable of correcting channel degradations resulting from variations in transponder operating points encountered in a working satellite system. Most importantly, the processor can correct channel degradation arising from varying degrees of up-path equalization mismatch, which is anticipated in a working TDMA environment. This paper reports on ATDES testing conducted at Paumalu Earth Station with the INTELSAT IV, F-4, satellite.

Introduction

Over the last few years, a considerable amount of experimental work has been performed in assessing the characteristics of a quaternary phase

*This paper is based upon work performed at COMSAT Laboratories under the sponsorship of the International Telecommunications Satellite Organization (INTELSAT).

shift keying (QPSK) channel through a band-limited satellite transponder using modems designed for linear channel operation with Nyquist filtering. The channel performance derived shows significant degradation (in terms of BER) as the power saturation of the nonlinear amplifiers is approached. The channel degradation is due primarily to the interaction of the transmission nonlinearities (the earth station HPA and the satellite TWTA) and the design of the channel filters for optimum operation in a linear channel.

QPSK modems operating at 120 Mbit/s have been designed to counteract the effect of nonlinear distortions [1]. The actual laboratory test results with these modems and with a simulator closely approximating an actual satellite channel (an early version of the INTELSAT V simulator) have shown that the performance of the nonlinear channel modems still needs considerable improvement when operation is very close to the HPA/TWTA saturation point [2].

A maximum likelihood sequence detection (MLSD) processor [3] using a dynamic programming algorithm (e.g., Viterbi algorithm) is a potential method for improving modem performance in a nonlinear satellite channel. Basically, the MLSD processor is a device that generates an error function by cross-correlating the received waveform with a locally generated candidate waveform over a restricted length of time to obtain a suitable measure (sufficient statistic) of the received waveform. The sufficient statistic acts as an input to the dynamic algorithm generator. The dynamic algorithm generates and continuously updates a history of candidate sequences and their associated correlation distances over the entire waveform and delivers optimally detected information bits as its output.

For a nonlinear channel, the principle of superposition fails, and the entire received waveform must be processed. The obstacle to optimum detection of a sequence of pulses in a nonlinear channel is processing complexity. The number of processing operations required in a straightforward ("brute force") approach increases exponentially with the length of the transmitted sequence. Furthermore, processing cannot begin until the entire sequence has been received.

At high speed (60–120 Mbit/s), the processing complexity and hardware size impose restrictions on the application of true MLSD. However, if it is assumed that in a digital satellite channel the detection of error is random, then a first-order approximation of MLSD theory results in a simplified hardware structure. The adaptive threshold detection with estimated sequence (ATDES) processor under examination is such a first-order approximation of MLSD that detects symbols with threshold detec-

tion [4]. In the ATDES processor, the intersymbol interference (ISI) from X trailing and X leading symbols is considered. The predecessors of the objective symbol are derived from the output of the final decision circuit, and the successors are estimated by the tentative decision circuit. Thus, ATDES eliminates the use of a dynamic algorithm generator. A 60-Mbit/s continuous mode ATDES processor was developed under an INTELSAT contract to demonstrate the proof of the principle [4].

The performance of the present 60-Mbit/s continuous mode processor was examined in a dynamic channel environment with an actual satellite channel. The dynamic nature of the TDMA channel arises from the fact that in an N -access system, uniform performance for all bursts received at a station requires that all N up-chains possess precisely the same equalization and flux density at the input of the transponder receiver. It is not realistic to expect that this condition can occur in a real system, and deviations are expected. The distortion memory of the ATDES processor optimized for a particular combination of earth station HPA and satellite TWTA backoff and channel equalization does not necessarily yield optimum performance for another set of HPA and satellite TWTA backoff combinations and channel equalization in an N -access TDMA environment.

The purpose of the tests was to examine the BER performance of the 60-Mbit/s continuous mode ATDES processor with a satellite link with N accesses.

Under INTELSAT sponsorship, a field test was conducted to evaluate the performance of the ATDES processor with the INTELSAT IV, F-4, satellite (transponder 10) and Paumalu I Earth Station. The test program included the following items:

- a. satellite loop calibration and E_b/N_o vs BER performance for the transponder at saturation, with and without ATDES (E_b/N_o calibrated with an unmodulated carrier);
- b. evaluation of ATDES distortion memory sensitivity at different transponder input backoffs with optimum tuning at saturation serving as a reference;
- c. channel performance improvement capability of the ATDES processor with added distortion in up-path chain simulating a multiple-access configuration.

Basic Concepts

The effect of band-limiting a PSK signal is demonstrated in Figure 1. In the signal space diagram for unfiltered QPSK modulation, as shown in

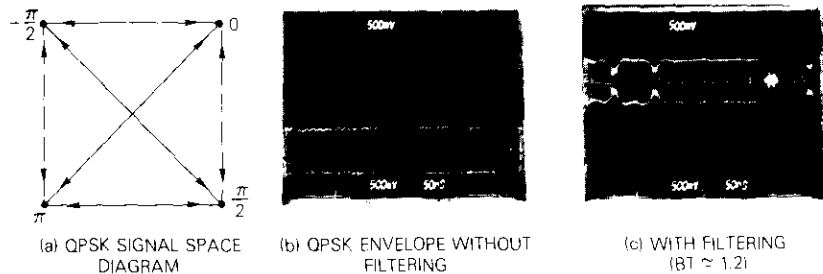


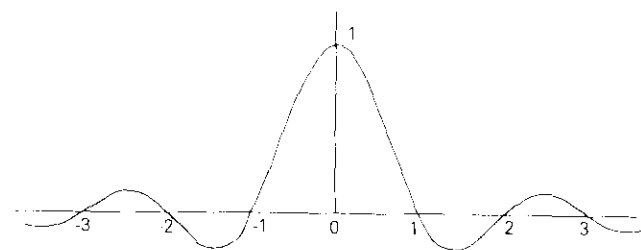
Figure 1. Effect of Band-Limiting PSK Signal

Figure 1a, the four possible phase positions (0° , $\pm 90^\circ$, and 180°) of the QPSK signal are represented by the dots of the square.

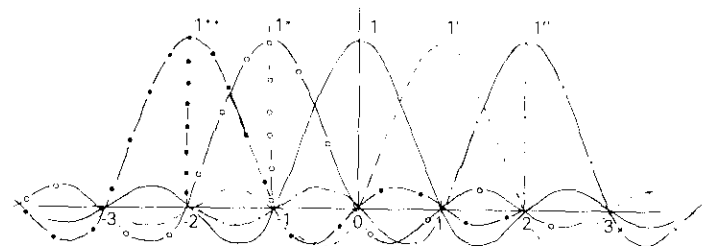
In the QPSK format, the signal can progress around the square in either direction, go across a diagonal, or remain at one corner, with no restrictions. The diagonal signal state transition gives rise to an instantaneous 100-percent amplitude modulation, because the signal amplitude vector momentarily travels from its peak amplitude through zero.

If the bandwidth of the transmission system is infinite, the phase transition time is zero. Therefore, the envelope of the modulated waveform is constant at each phase transition, as shown by Figure 1b. In a band-limited channel, however, the transition time is finite. The envelope then has a depression at phase transition, especially for a diagonal transition, where the envelope is always depressed close to zero, as shown by Figure 1c. These amplitude depressions, coupled with the AM-to-PM transfer effect present in the satellite TWT and earth station HPA devices, introduce additional unwanted phase distortion of the PSK signal and thereby give rise to a complex form of ISI.

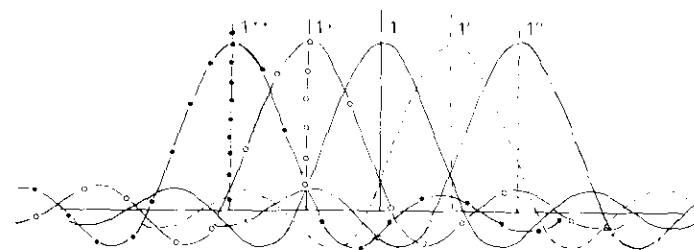
Consider the situation shown by Figure 2a, in which a single pulse (labeled 1 in the figure) is transmitted over a band-limited channel. Assume the channel is free from phase distortion (*i.e.*, that the phase-frequency relationship is linear) and hence is free from zero-crossing error (Nyquist filtering criteria—see Reference 5), *i.e.*, that at every sampling point (-3 , -2 , -1 and 1 , 2 , 3) except that under detection, the energy of the pulse is zero. If the superposition principle is applicable, the trailing and leading pulses (1^{**} , 1^* and $1'$, $1''$) will also be free from zero-crossing error, and ISI-free reception will result, as shown by Figure 2b. However, if the channel phase-frequency response is not linear, then the zero-crossing problem will influence a symbol detection process based on instantaneous sampling (*e.g.*, midbit sampling), as shown by Figure 2c. In



(a) THE WAVEFORM OF COSINE ROLL-OFF SPECTRUM (ROLL-OFF 30%)



(b) SUPERPOSITION OF ABOVE WAVEFORM WITH NO ZERO-CROSSING ERROR



(c) SAME AS ABOVE WITH ZERO-CROSSING ERROR

Figure 2. Principle of Intersymbol Interference

a linear, symmetric, and time invariant channel, this simple form of ISI can be virtually eliminated by a delay-equalizing network. In a nonlinear QPSK channel having AM/AM and AM/PM transfer characteristics, the

distortions of the signal vectors in four quadrants do not necessarily line up symmetrically. This asymmetrical distortion cannot be eliminated by phase-frequency linearization.

Examination of Figure 2c reveals that a sample at the center of a symbol interval is a weighted sum of amplitudes of pulses in several adjacent trailing and leading pulses. The mechanism of sample detection with due weighting of the adjacent pulses is MLSD. This technique is powerful in combating both linear and nonlinear distortion [3], [6].

Conceptually, then, the operations that the MLSD receiver must perform are shown in Figure 3. The received waveform is prefiltered to reduce adjacent channel energy, introduce noise whitening [6], and reduce the spread of the signal pulses. The resultant signal is then correlated (over trailing and leading symbols) with replicas of the possible received waveforms that can be derived from a candidate symbol generator, followed by a hardware model of the nonlinear devices. The resulting objective function is processed by an algorithm to select the sequence with the minimum path metric (derived from the mean square difference between a function representing the received sequence and one representing the assumed transmitted sequence) [3], [6], [7]. The implementation complexity of a structure that examines all possible sequences increases exponentially with the sequence length. The dynamic programming algorithm (Viterbi algorithm) [7] required to continuously update the channel memory with changing sequence pattern becomes extremely difficult to achieve at high speed (10-20 Mbit/s or more). The straightforward method has also been advocated [8]. In a continuous operating mode where convergence time is

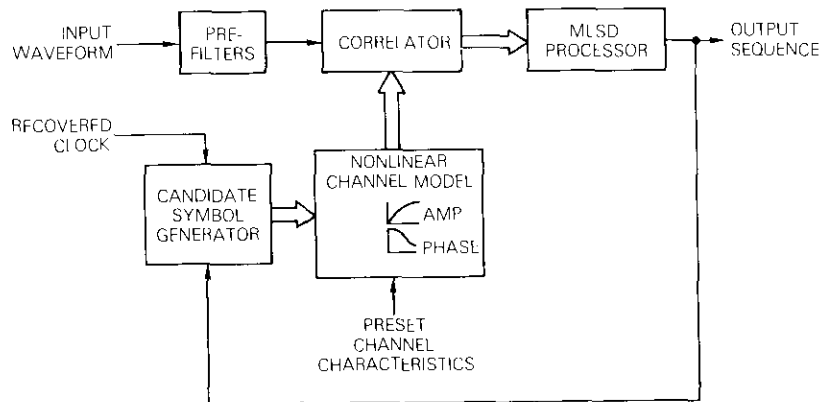


Figure 3. *MLSD Processor Concept*

of no significance, the straightforward [8] method can be substituted for the Viterbi algorithm [7].

In a digital satellite channel, the detection of error is random in nature. Hence, it is safe to assume that even in a complex ISI case with nonlinear scattering, there still exist optimum decision boundaries, as shown in Figure 4. The ATDES processor discussed here uses the principle of adaptively optimizing detection thresholds for minimum error. The

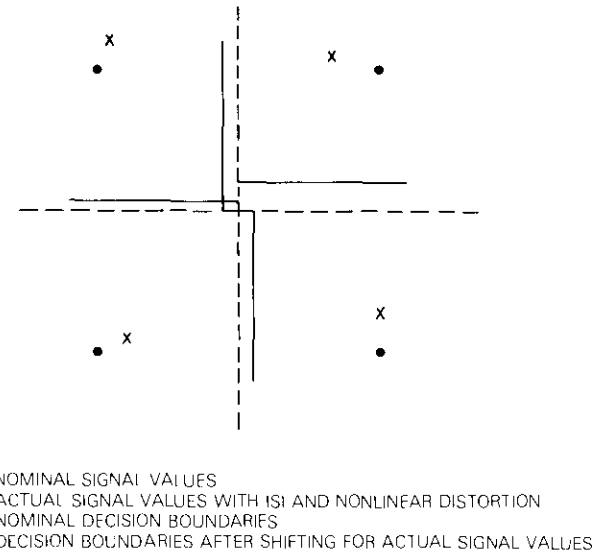


Figure 4. *Asymmetrical Decision Threshold Due to Nonlinear Distortion*

ATDES processor is a first-order approximation of MLSD. It represents a more practical, feasible way to obtain the benefit of MLSD. Figure 5 is a block diagram of the ATDES principle, where the ISI is considered from the one trailing and one leading symbol relative to an objective symbol in a BPSK channel [4]. Let the received sample b_0 (without ISI) be expressed as

$$b_0 = F(a_{-1}, a_0, a_1) + n_0 \tag{1}$$

where n_0 is the noise component. The optimum decision on b_0 is obtained by setting the decision threshold at d_0 , where

$$d_0 = \frac{1}{2} [F(a_{-1}, 1, a_1) + F(a_{-1}, -1, a_1)] \tag{2}$$

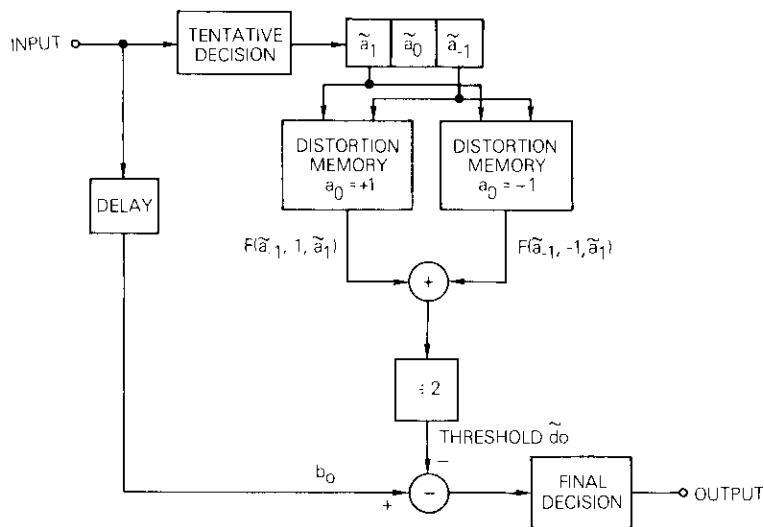


Figure 5. Basic ATDES Principle for BPSK

To obtain the optimum decision threshold, ATDES first estimates the actual received sequence $(\tilde{a}_{-1}, \tilde{a}_0, \tilde{a}_1)$ by a tentative decision circuit operating on the sign of the input and succeeded by a shift register. Then the suboptimum threshold \tilde{d}_0 for b_0 is obtained by

$$\tilde{d}_0 = \frac{1}{2} [F(\tilde{a}_{-1}, 1, \tilde{a}_1) + F(\tilde{a}_{-1}, -1, \tilde{a}_1)]$$

where $F(\tilde{a}_{-1}, 1, \tilde{a}_1)$ and $F(\tilde{a}_{-1}, -1, \tilde{a}_1)$ are based on the tentatively estimated sequence and are extracted from the distortion memory. If the estimated sequence $(\tilde{a}_{-1}, \tilde{a}_1)$ is correct, the suboptimum threshold becomes the optimum threshold; \tilde{d}_0 is subtracted from the received sample b_0 ; and the final decision is made on the sign of the difference.

Similarly, the ATDES principle for QPSK is illustrated in Figure 6, where the received sequence is expressed in complex form as

$$\tilde{a}_k = \tilde{p}_k + j\tilde{q}_k \quad (3)$$

In hardware implementation [4], the analog input signal is converted into digital form by high-speed (30 Msymbol/s) A/D converters with 8-bit resolution. The degradation due to the quantization noise was found to be less than 0.01 dB at a signal-to-noise ratio of 10 dB. The distortion memory

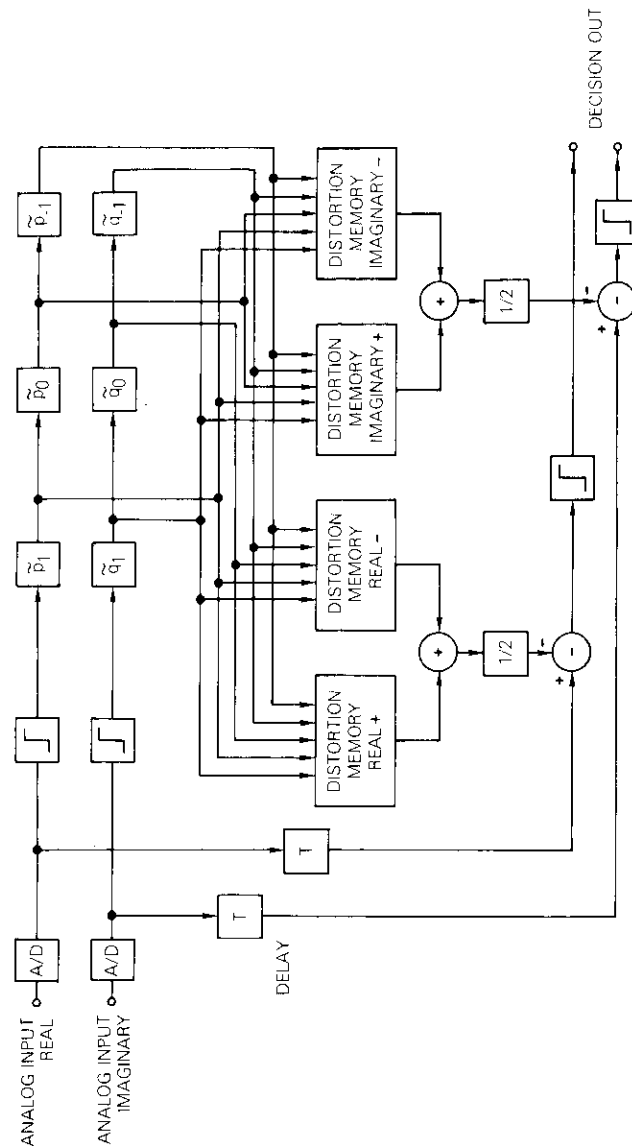


Figure 6. ATDES Principle for QPSK; $\tilde{a}_k = \tilde{p}_k + j\tilde{q}_k$

consists of RAM in which the distortion of the received signal corresponding to every N -symbol sequence is stored.

Figure 7 is a block diagram illustrating the principle of overall ATDES processing.

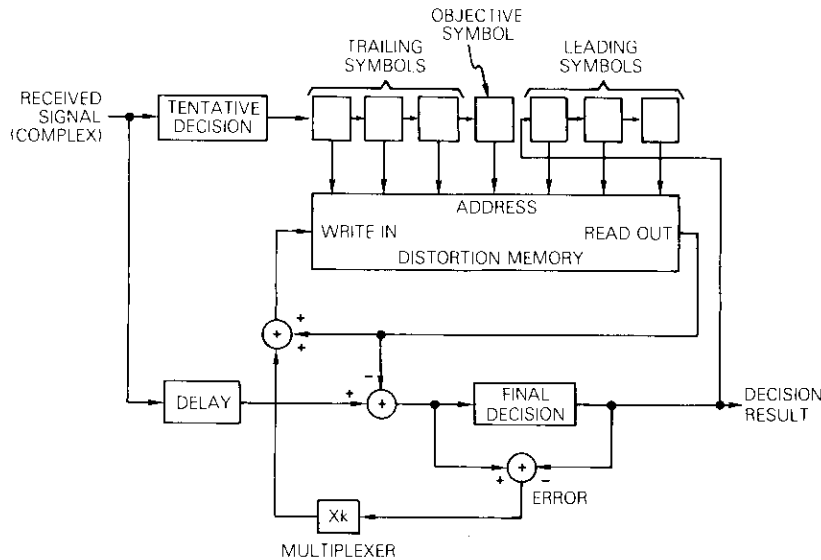


Figure 7. ATDES Processor Principle

The accuracy of detection increases with X , the number of trailing and leading symbols included in the correlation. On the other hand, the hardware complexity and time of convergence also increase with X . For example, with 5-symbol correlation, the number of sequences to be considered is 4^5 . To make the system manageable and at the same time to substantially retain the characteristics of MLSD, the 60 Mbit/s continuous mode ATDES processor under discussion uses 5-symbol correlation (the symbol to be detected with two leading and two trailing symbols). The prototype processor is designed for continuous mode operation, and hence the convergence time was not taken into account. A straightforward algorithm was used for channel adaptation.

The average distortion of a given 5-symbol pattern is stored in the distortion memory circuit, which is then subtracted from the delayed received signal. In this way, the scheme for decision with adaptive thresh-

old control is obtained. The contents of the distortion memory circuit are updated by averaging the received ISI corresponding to each sequence pattern. The predecessors of the objective symbol are derived from the output of the final decision circuit, and the successors are estimated by the tentative decision circuit.

Therefore, the essential functions of the ATDES processor are the following:

- a. finding the receive symbol pattern around the objective symbol to be detected from the decision circuit output,
- b. extracting the error signal from the decision output and the detected symbol pattern from the distortion memory,
- c. averaging the error signal with the proper weight,
- d. entering the average value into the distortion memory as a new set corresponding to the detected-symbol pattern.

A detailed description of the ATDES hardware is given in Reference 4.

Experimental procedure

The salient features of the 60-Mbit/s QPSK modem used in this experiment are the following:

Transmit Filters	Low-pass, $\sqrt{40\%}$ Nyquist + $(x/\sin x)$ shaping
Receive Filters	Low-pass, $\sqrt{40\%}$ Nyquist
Modulation	QPSK with and without differential encoding
Mode of Operation	Continuous
Demodulation	Coherent detection
Carrier Recovery	X4 and narrowband filtering
Clock Recovery	Half-symbol delay type

Figure 8 is a simplified block diagram of the Paumalu I Earth Station and INIELSAT IV, F4, configuration. The 12-kW HPA output is calibrated as a function of the input drive with a 6-GHz vane attenuator. The earth station transmit e.i.r.p. (HPA output at the feed plus the antenna gain at 6.320 GHz) as a function of the precision vane attenuator setting was then calibrated.

The amplitude and group delay responses of the station loop (up-converter, 1FL amplifier, 1,500-ft waveguide run, IPA, HPA, 6/4-GHz translator, LNA, 1,500-ft waveguide run, and down-converter) were equalized with fixed equalizers.

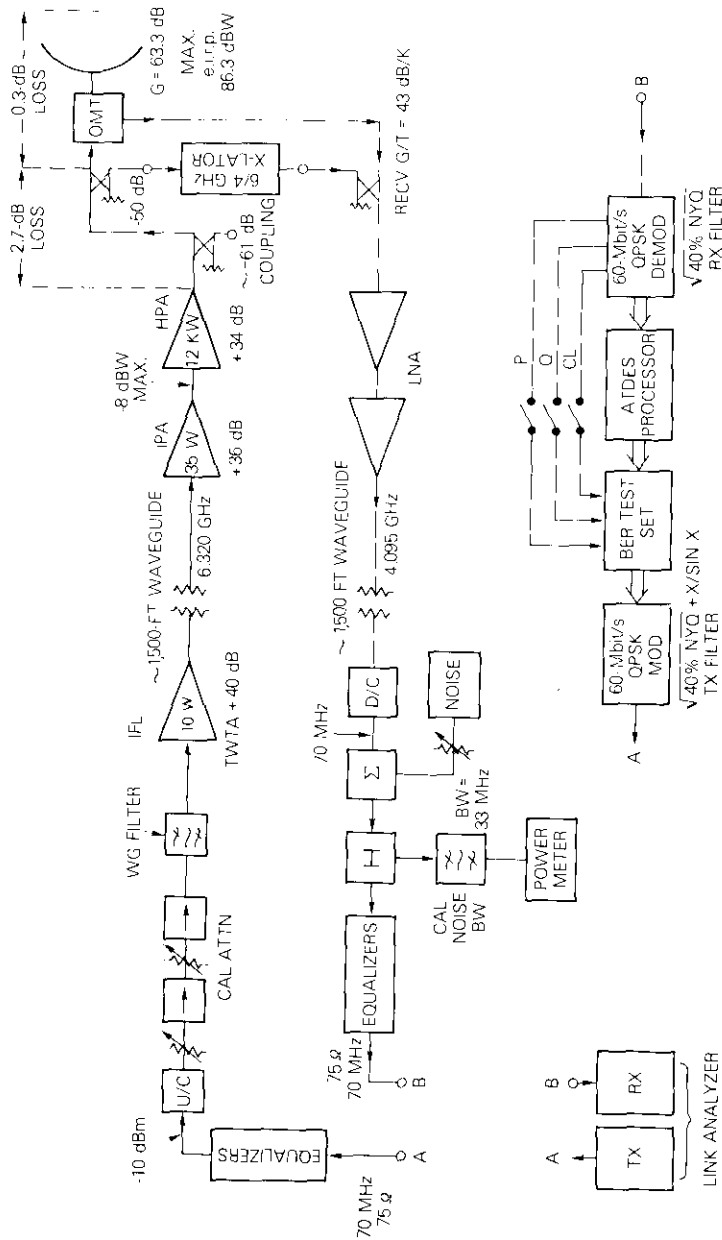


Figure 8. Schematic of Paumalu I Earth Station and INTELSAT IV, F4, System

Satellite loop measurements

The predicted parameters of the INTELSAT IV, F-4 (Transponder 10), and Paumalu I Earth Station link are the following:

Up-Path Loss from Paumalu at 6.320 GHz	199.9 dB
Down-Path Loss to Paumalu at 4.095 GHz	196.7 dB
Up-Path Aspect Correction from Paumalu	-1.5 dB
Down-Path Aspect Correction to Paumalu	-1.6 dB
Spacecraft Beam Center Gain-to-Noise-Temperature Ratio (G/T)	-13.1 dB/K
Spacecraft Beam Center Saturated e.i.r.p.	27 dBW
Earth Station Transmit Antenna Gain at 6.320 GHz	63.3 dB
Earth Station Receive G/T at 4.095 GHz and at 53° Elevation	43 dB/K

The single carrier (CW) power transfer curve of the spacecraft TWTA was generated as a function of the calibrated vane attenuator setting, and the measured curve is shown in Figure 9. The measured earth station e.i.r.p. required for the spacecraft TWTA saturation was found to be 86.3 dBW.

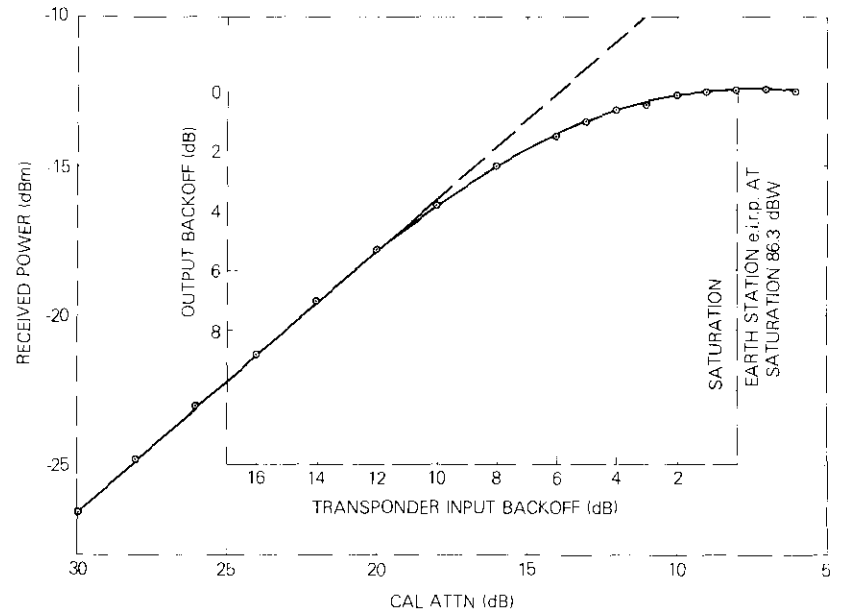


Figure 9. Satellite Transponder TWTA Power Transfer Curve

The link C/N vs input backoff characteristics were measured by the carrier (CW) shift technique,* and the measured curve is shown in Figure 10.

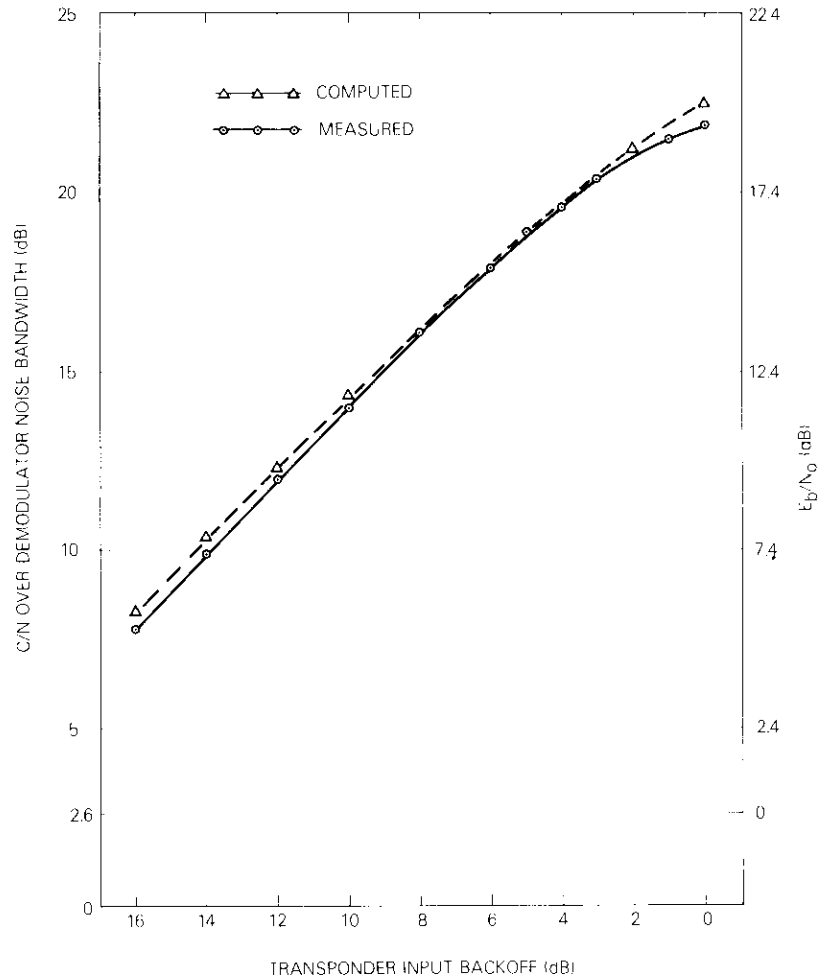


Figure 10. Link C/N and E_b/N_o vs Transponder Input Backoff

*In a carrier shift technique, the carrier (CW) plus the noise is measured through a narrowband filter centered in the transponder band. Later the carrier is shifted from the band center, and the noise power is measured. From these two sets of measurements, system C/N is evaluated by appropriate translation of narrowband filter bandwidth and the transponder bandwidth.

The computed C/N curve based on the link parameters and earth station e.i.r.p. is also shown for comparison.

The satellite link amplitude and group delay characteristics with and without equalization are shown in Figure 11, where the fixed equalizers used in the up-path and down-path are also identified. The measured

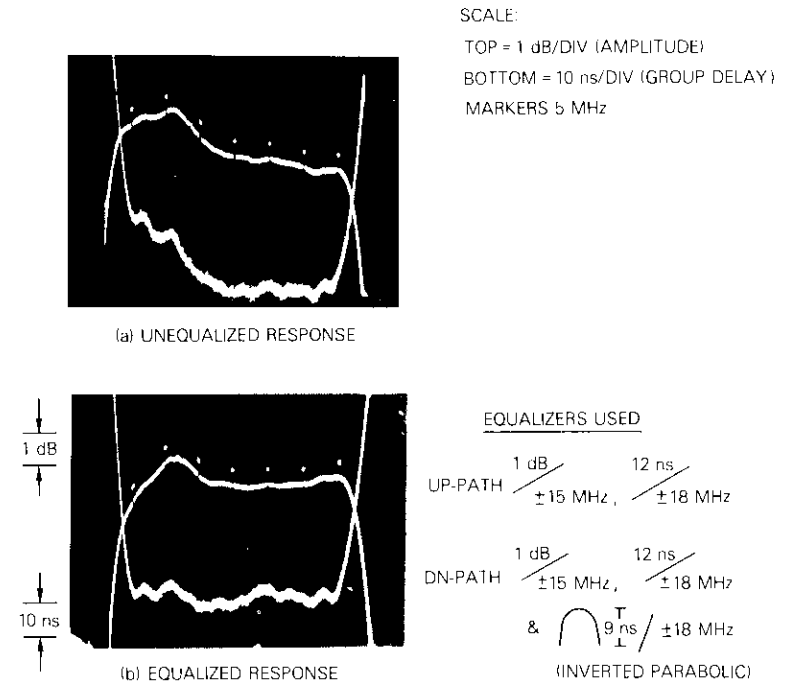


Figure 11. Satellite Loop Amplitude and Group Delay Response (6-dB TWTA Input Backoff)

E_b/N_o vs BER curves with and without ATDES for unequalized and equalized satellite loops and for the transponder operating at saturation are shown in Figure 12. [$E_b/N_o = C/N - 10 \log(R/B_N)$, where C is the unmodulated carrier power, N is the noise power, R is the bit rate, and B_N is the noise bandwidth of the noise-measuring filter.] The C/N ratio was adjusted by adding a known level of noise prior to the demodulator (see Figure 8). E_b/N_o was then determined from C/N and a correction factor that arises from the fixed-link noise.

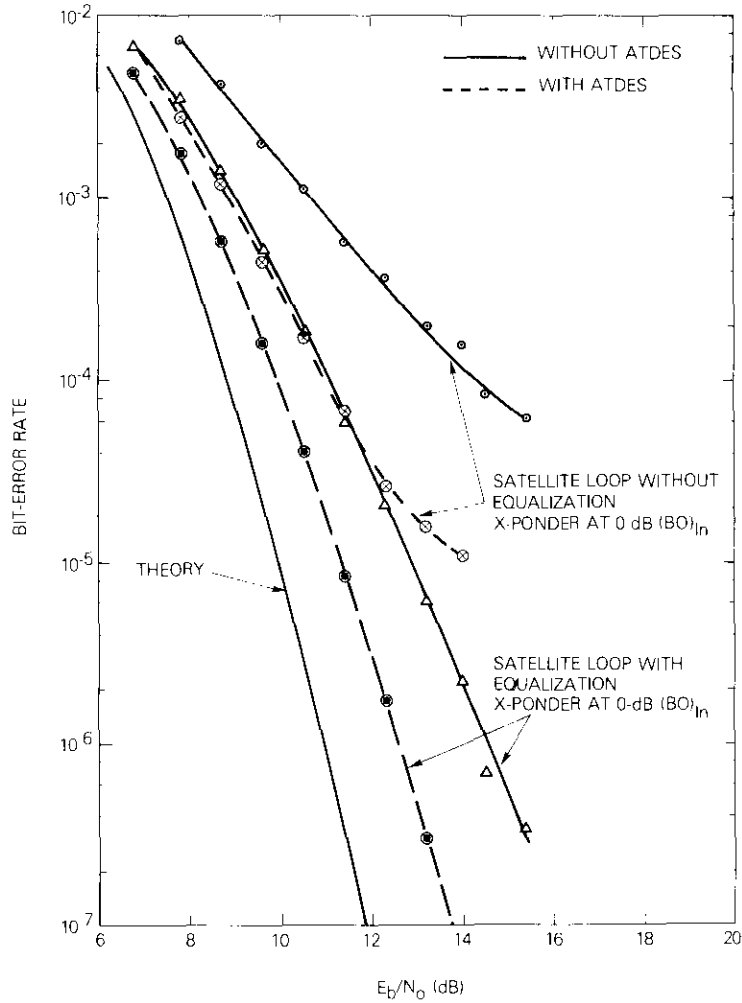


Figure 12. *Satellite Loop Performance With and Without ATDES—BER vs E_b/N_0*

ATDES distortion memory sensitivity study

As mentioned before, the present ATDES processor is designed for correlation with two trailing and two leading symbols, and the distortion memory built in the processor has a finite range of correction (to be determined). It is, therefore, important to examine the effect of variation

of the nonlinear operating point of the transponder TWTA with the ATDES tuned to a particular input backoff. This examination was conducted by measuring the E_b/N_0 vs BER performance of the channel with the ATDES optimally tuned at 0-dB transponder input backoff and comparing the results with the channel performance for 2- and 4-dB input backoffs. The measured data are shown in Figure 13. The closeness of the data points at

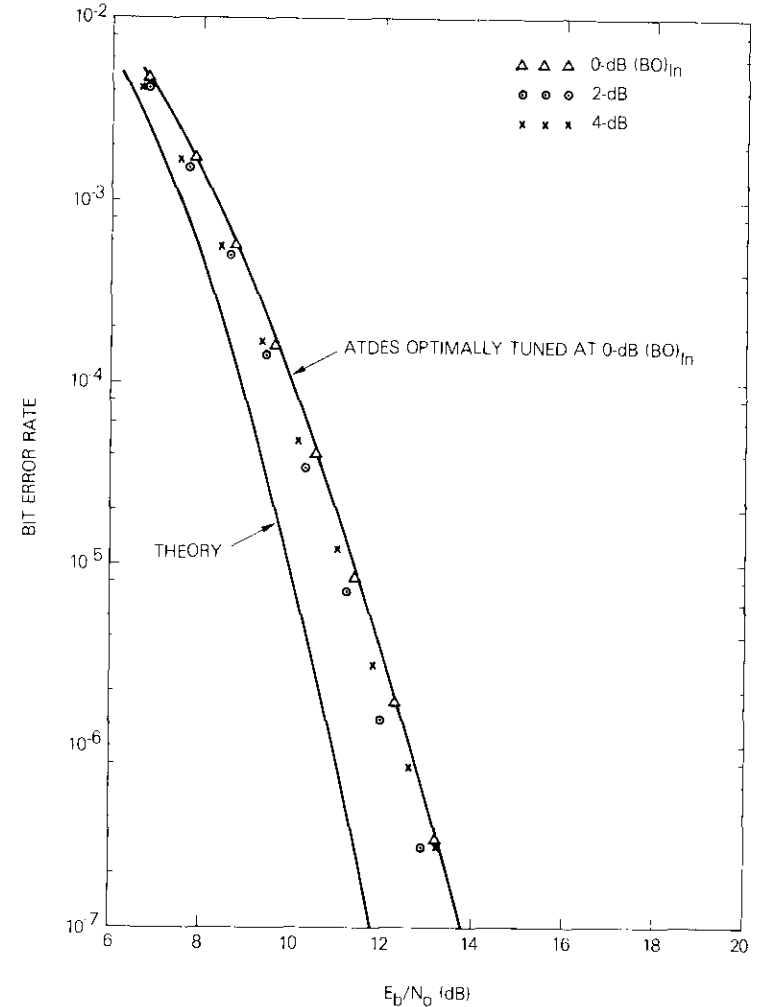


Figure 13. *ATDES Distortion Memory Sensitivity Study—BER vs E_b/N_0*

0-, 2-, and 4-dB input backoff operation as shown in Figure 13 indicates that the distortion memory is capable of improving the channel performance within the range of transponder operation expected in a 4/6-GHz band TDMA operating environment. In practice, the 2- and 4-dB performance curves (Figure 13) are somewhat better than the 0-dB curve. This improvement is attributed to the milder effect of the transponder nonlinearity at 2- and 4-dB input backoffs.

Channel sensitivity study as a function of up-path equalization perturbation

In an ideal N -access TDMA configuration outlined in Figure 14, the N th access down-chain equalization should match the $N - 1$ accessing up-path equalizations for optimum system performance. However, in an actual operating environment, this ideal situation will not exist because of finite

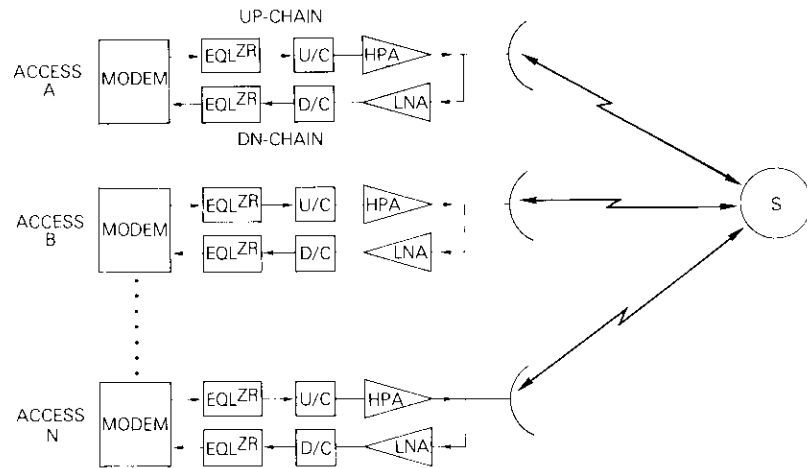


Figure 14. *N-Access TDMA Configuration*

variation in up-path equalizations. For example, access A may achieve optimum equalization between A and B , but the same condition may not hold between, for example, A and C or A and D , because of the difference in up-path equalizations. This condition has been simulated in the present experiment by inserting various distortions in the up-path while keeping the down-path equalization the same as in the case of nominal equalization achieved during the satellite loopback test. A parametric study has been conducted with the following additional distortion inserted in the up-path:

$a.$ -1,- 2-, and -3-dB amplitude linear slopes over ± 18 MHz. The perturbations in the overall link equalization are shown in Figure 15, where the nominal equalization characteristics of the

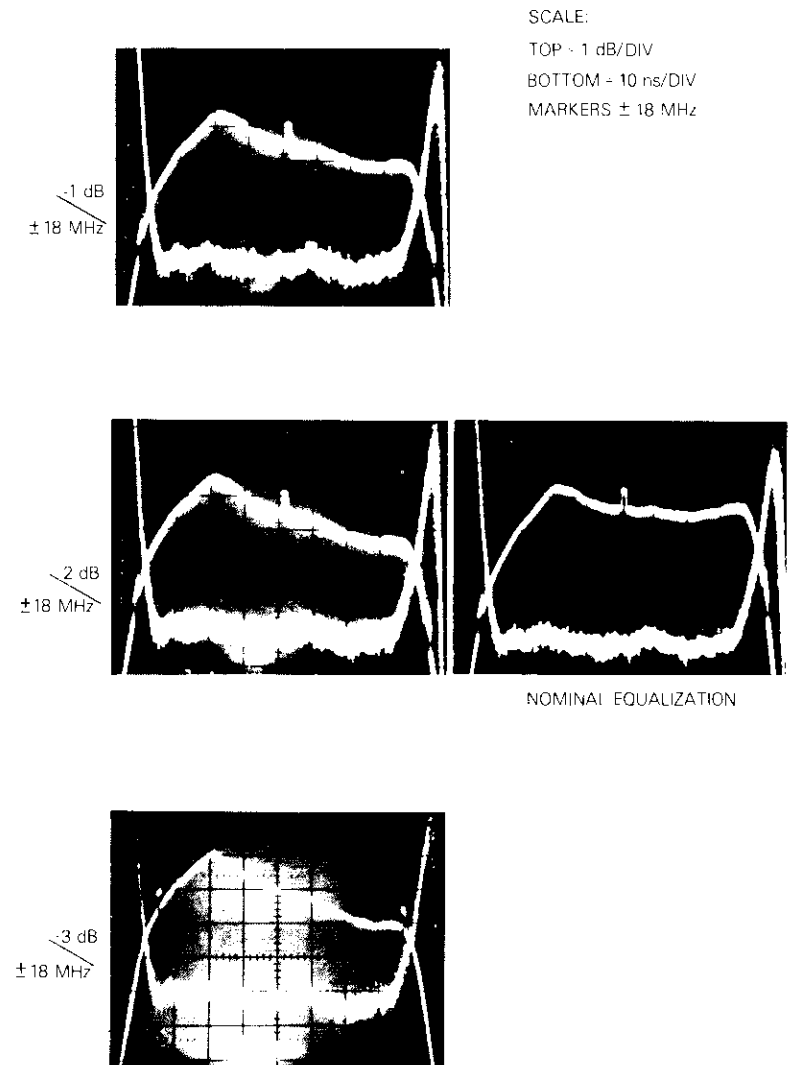


Figure 15. *Link Equalization Perturbation Due to Amplitude Distortion Added in Up-Path*

channel are also shown for comparison. The corresponding E_b/N_o vs BER curves with and without ATDES are shown in Figure 16. The results will be discussed later.

b. -18-, -24-, and -33-ns linear delay distortions over ± 18 MHz. The corresponding equalization characteristics and E_b/N_o vs BER

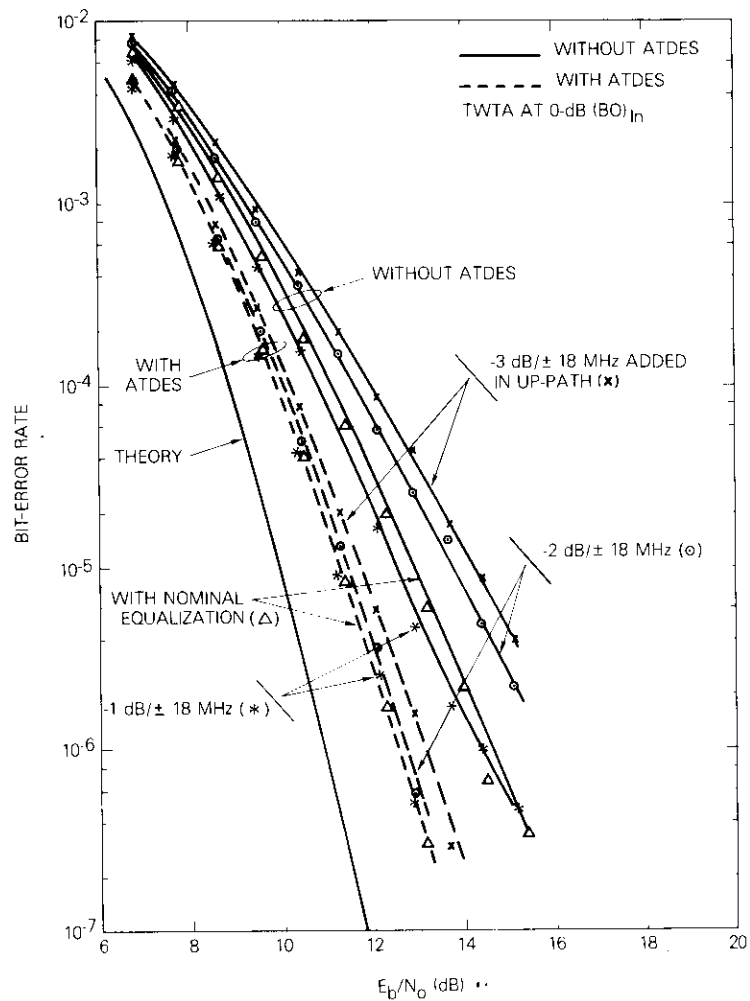


Figure 16. Channel Sensitivity Study With and Without ATDES—Amplitude Slope as Parameter

curves with and without ATDES are shown in Figures 17 and 18, respectively.

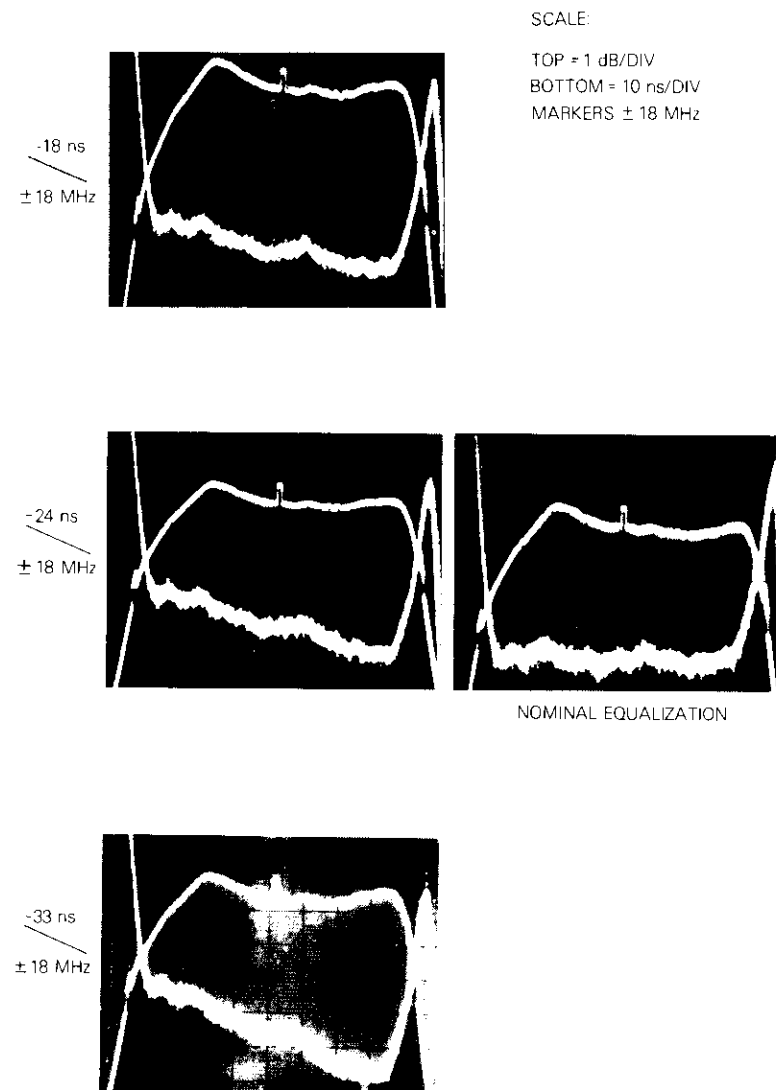


Figure 17. Link Equalization Perturbation Due to Linear Delay Distortion Added in Up-Path

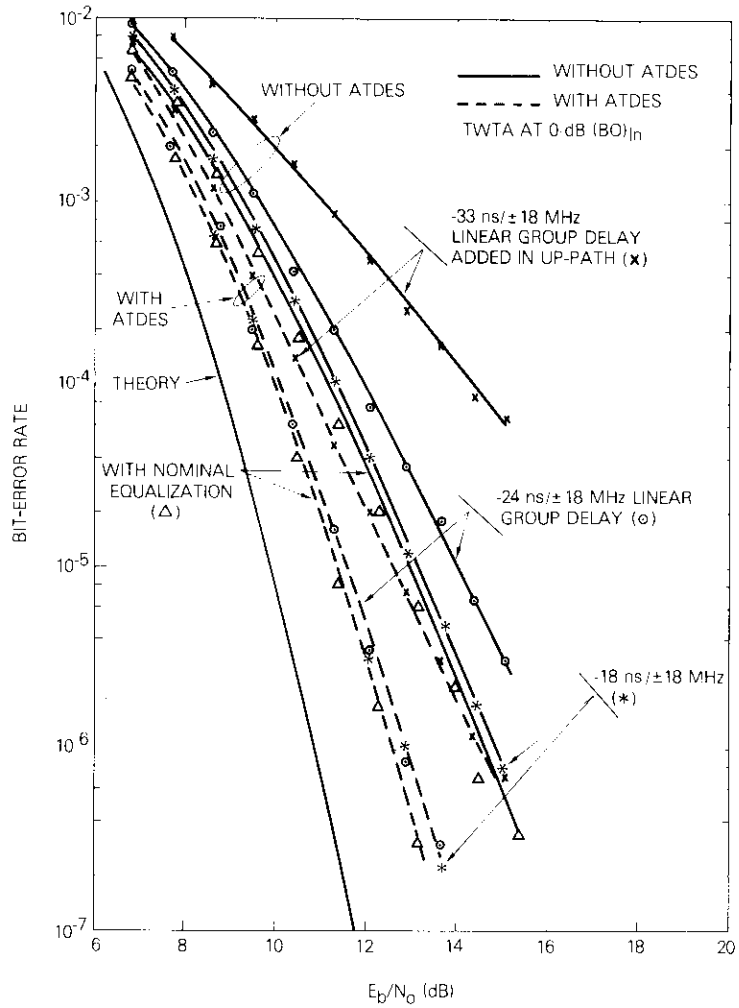


Figure 18. Channel Sensitivity Study With and Without ATDES—Linear Group Delay Distortion as Parameter

c. 12-, 18-, and 24-ns parabolic delay distortions over ± 18 MHz. The corresponding equalization characteristics and E_b/N_o vs BER curves are shown in Figures 19 and 20, respectively.

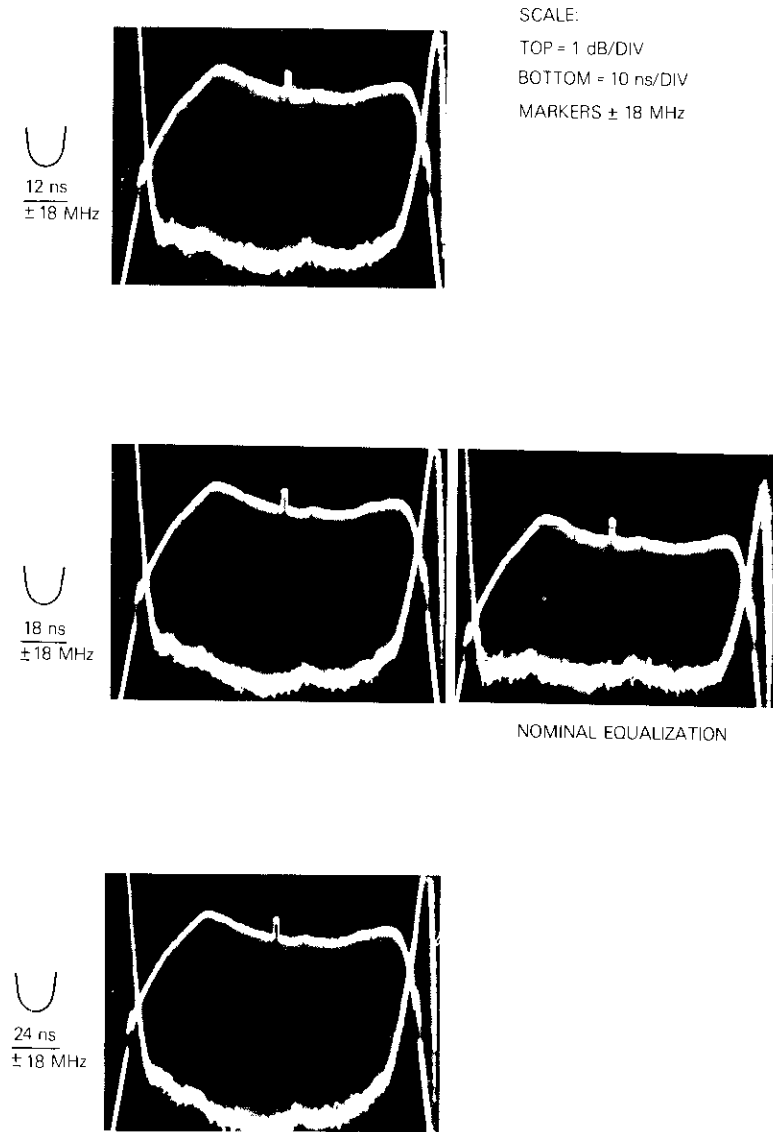


Figure 19. Link Equalization Perturbation Due to Parabolic Delay Distortion Added in Up-Path

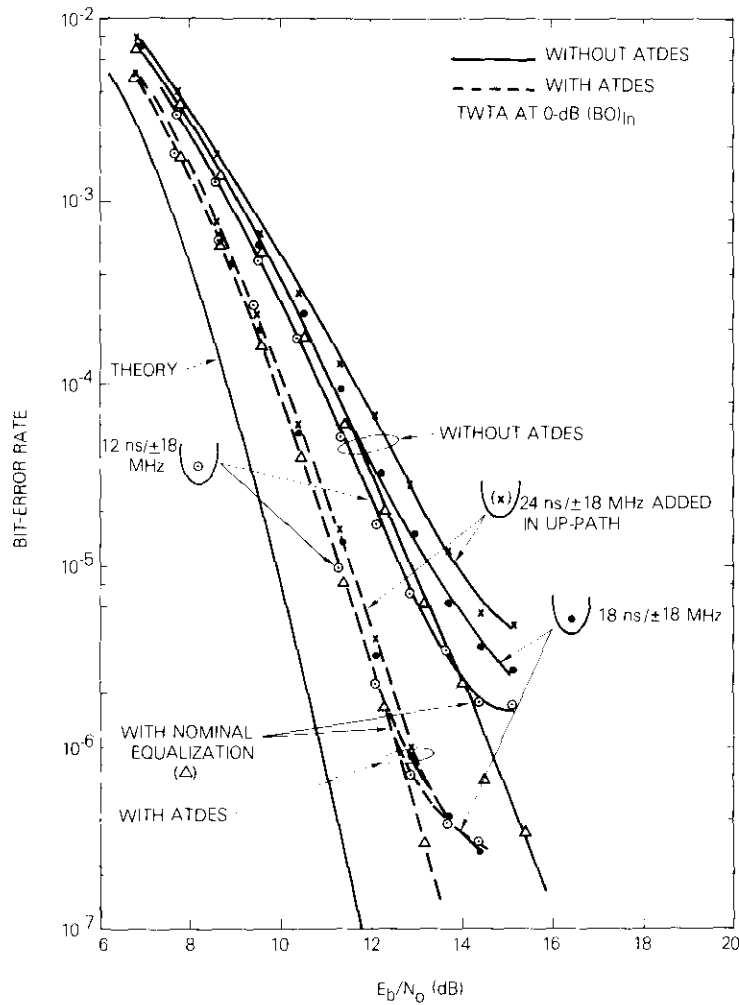


Figure 20. Channel Sensitivity Study With and Without ATDES—Parabolic Delay Distortion as Parameter

Discussion of the experimental results

The earth station e.i.r.p. requirement was well within the linear operating region of the HPA.

The measured C/N curve agreed well with the computed curve (see Figure 10) for the actual up-path e.i.r.p.

The nominal link equalization achieved resulted in about 1-dB amplitude variation and approximately 6-ns group delay variation over the Nyquist band (± 15 MHz at 60-Mbit/s QPSK), which is considered acceptable in a practical environment (refer to Figure 11). The resulting BER curves shown in Figure 12 demonstrated a significant performance improvement over the unequalized channel performance. In the channel sensitivity study, without ATDES, the -1-dB amplitude distortion curves (see Figure 16) slightly improved the channel performance over the nominal equalization curve. The result indicates that in certain cases there is a possibility that the up-path equalization and modem tuning of a specific accessing station may improve the channel performance marginally, compared to the satellite loopback performance of another accessing earth station configuration. However, with ATDES, the performance improvement was optimum with the nominal link equalization. Similar results were observed with the linear and parabolic delay distortion cases as shown in Figures 18 and 19, respectively. In most cases, the channel performance without ATDES demonstrated degradation with the insertion of up-path distortions. On the other hand, ATDES almost entirely corrected these degradations.

Conclusions

The 60-Mbit/s continuous mode ATDES processor under examination amply demonstrated its potential benefit in a practical satellite environment. The ATDES processor improved the nominally equalized satellite channel E_b/N_o by about 2 dB at an error rate of 10^{-6} . The distortion memory of the processor is capable of correcting the channel degradation within the expected variation in the operating point of the satellite transponder resulting from a multiple access working environment. Most importantly, the ATDES processor can correct varying degrees of up-path equalization mismatches anticipated in a TDMA working environment.

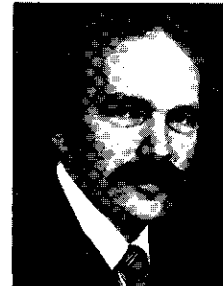
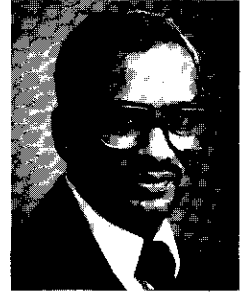
Acknowledgments

Thanks are due to S. J. Campanella and T. Dobyms for their interest in this project. Acknowledgment is made to INTELSAT R&D for supporting this program. The ATDES processor was developed by Nippon Electric Company, Ltd., Tokyo, Japan, under an INTELSAT contract.

References

- [1] D. Chakraborty, T. Noguchi, S. J. Campanella, and C. J. Wolejsza, "Digital Modem Design for Nonlinear Satellite Channels," Fourth International Conference on Digital Satellite Communications, Montreal, Canada, October 23-25, 1978, *Proc.*, pp. 123-130.
- [2] D. Chakraborty and M. E. Jones, "Laboratory Simulation Results of 120 Mbit/s QPSK Nonlinear Channel Modems," Fifth International Conference on Digital Satellite Communications, Genoa, Italy, March 23-26, 1981.
- [3] D. Chakraborty, "Maximum Likelihood Sequence Detection in Nonlinear Satellite Channels," *IEEE Communications Magazine*, November 1981.
- [4] Y. Furuya, F. Akashi, and S. Murakami, "A Practical Approach Toward Maximum Likelihood Sequence Estimation for Band-Limited Nonlinear Channels," Fifth Conference on Satellite Communications, Genoa, Italy, March 23-26, 1981.
- [5] W. R. Bennett and J. R. Davey, *Data Transmission*, New York: McGraw-Hill, 1965, Chapter 5.
- [6] G. D. Forney, Jr., "Maximum Likelihood Sequence Estimation of Digital Sequences in the Presence of Intersymbol Interference," *IEEE Transactions on Information Theory*, IT-18, May 1972, pp. 363-378.
- [7] G. D. Forney, Jr., "The Viterbi Algorithm," *Proc. IEEE*, Vol. 61, March 1973, pp. 268-278.
- [8] G. F. Herrmann, "Performance of Maximum-Likelihood Receiver in the Nonlinear Satellite Channel," *IEEE Transactions on Communications*, COM-26, No. 3, March 1978, pp. 373-378.

Dayamoy Chakraborty received a Ph.D. in microwave physics from the University of Surrey, England, in 1967. Since 1968, he has been employed by COMSAT. From 1968 to 1971, he was involved with the satellite system optimization study and the analysis of transmission deviations. Dr. Chakraborty transferred to COMSAT Laboratories in 1971 and has been involved in developing high-speed digital satellite communications systems. Currently as a Senior Staff Scientist in the Digital Communications Laboratory, he directs research in nonlinear satellite channel model design, maximum likelihood sequence estimation, and digital link technology. Prior to joining COMSAT, he was employed by the British Post Office, Research Department, Dollis Hill, London. Dr. Chakraborty is the author of numerous publications on microwave techniques and communications technology, and is a senior member of IEEE and a corporate member of IEE.



Mark Kappes received a B.S.E.E. and an M.S.E.E. from the University of Illinois in 1971. Since joining COMSAT Laboratories in 1979, Mr. Kappes has been a member of the technical staff in the Modulation Techniques Department. His work has involved the design of QPSK modems as well as various types of equalizers required for high bit rate TDMA systems. Previously, Mr. Kappes was employed by Watkins Johnson, where he was responsible for the design of low-noise, high dynamic range receivers, and special-purpose demodulators.

CTR Notes

4-GHz high-efficiency broadband FET power amplifiers

S. CHOU AND C. CHANG

(Manuscript received August 11, 1982)

Introduction

Traveling wave tubes (TWTs) have been used extensively as high-power amplifiers in communications satellite transponders over the past two decades. Although design improvements such as the double-tapered helix, the multistage depressed-electrode collector, and the impregnated matrix dispenser cathode have significantly increased the efficiency and life span of TWTs, their inherent nonlinear phase-amplitude transfer characteristics and limited life remain important drawbacks. Hence, solid-state field effect transistor (FET) amplifiers are needed to replace TWTs in communications satellites.

Considerations of the allocation of additional bandwidth for future satellite services will depend critically on the realization of high-efficiency broadband solid-state power amplifiers (SSPAs). The measured broad bandwidth and high efficiency of this amplifier make it attractive as a building block for an SSPA chain, which would serve as a complete replacement for the TWT.

Su Min Chou is senior staff scientist in the Microwave Communications Laboratory, COMSAT Laboratories. C. Chang is on sabbatical at COMSAT Laboratories from Taipei Earth Station, Republic of China.

This note describes the development and performance of a 4-GHz high-efficiency broadband FET power amplifier module. A single-device amplifier operating over a 700-MHz bandwidth centered at 4 GHz provided a gain of 6 ± 0.25 dB and an RF output power of 3.2 W with a power-added efficiency of 48.6 percent. With an added broadbanding circuit, a bandwidth of 1 GHz, a gain of 5.5 ± 0.2 dB, and an efficiency of 40.5 percent were achieved.

Amplifier design and fabrication

Existing commercially available devices have been used because of their performance and acceptability for spaceflight. A 7.2-mm multicell FET device (Fujitsu FLC30), designed to provide 2.5-W output power, 6-dB gain, and 31-percent power-added efficiency, was chosen.

Device characterization was performed on an automatic network analyzer to obtain the small signal S-parameters with a short section of 50 Ω microstrip transmission line printed on 25-mil-thick alumina. The S-parameters are shown in Figure 1. The measured values show good agreement with the manufacturer's data.

At a high power level, the FET is nonlinear, and the optimum load impedance for maximum output power varies with input level. This nonlinearity presents many problems and complications to the designer of high-power FET amplifiers. Methods such as load-pull technique, large signal S-parameter measurement, and the large signal FET model are generally employed. The tedious nature of the work and the question of the accuracy involved for such methods have always been troublesome to the design engineer. It has been possible to simplify the design of a high-power amplifier module because of the following:

- a. The input impedance of the specific FET that was used in the COMSAT design is nearly independent of the input level. Only the output impedance varies significantly with power level.
- b. Adjusting the load impedance for maximum power and minimum intermodulation under large signal conditions does not affect the broadband performance of the amplifier.

The amplifier design was first based on the measured small signal S-parameters of the FLC30 FET. The gain and broad bandwidth characteristics were computed and optimized with use of the SUPERCOMPACT CAD program. Figure 2 is a schematic of the single-ended amplifier, showing the main elements. Broader bandwidth was achieved by adding two open stubs to the input matching circuit. Figure 3 shows an example of the predicted small signal gain-frequency response.

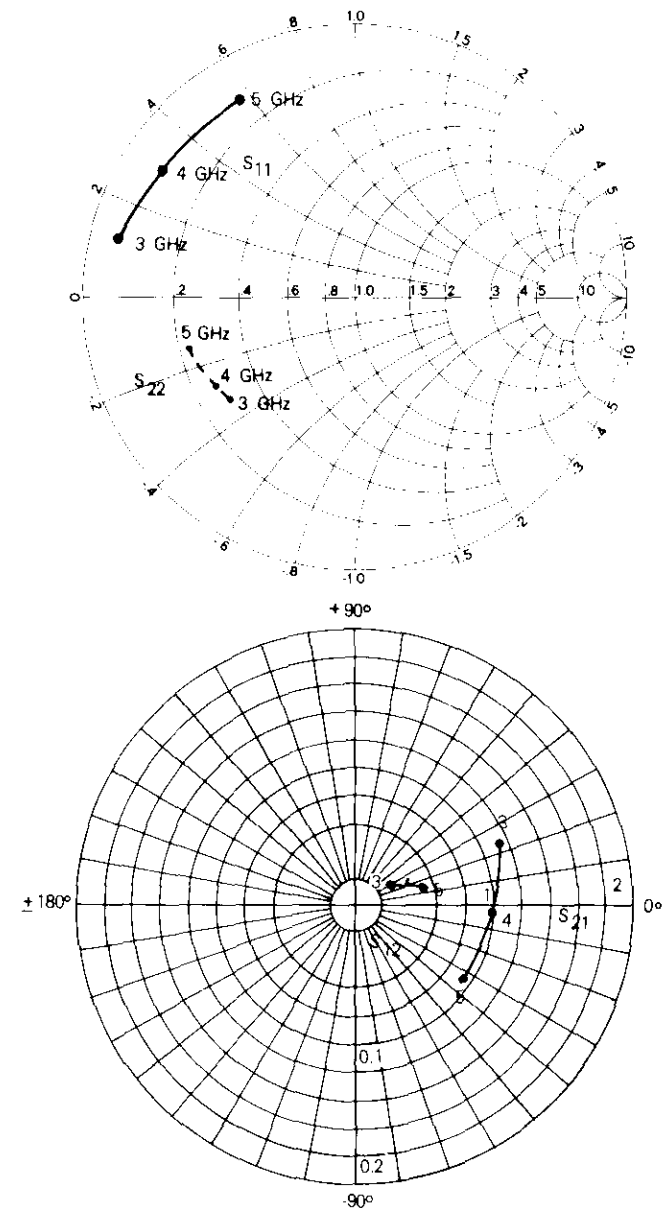
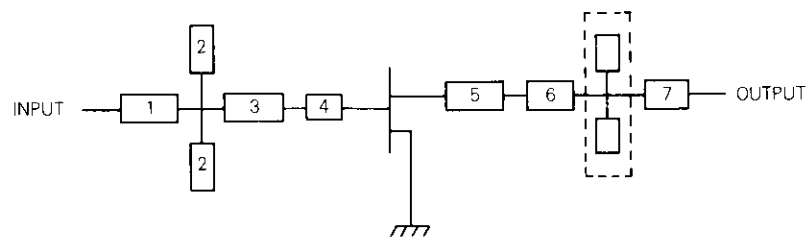


Figure 1. S-Parameters Used for Amplifier Design



ELEMENT NO.	IMPEDANCE (ohms)	LENGTH AT 4 GHz
1	23.6	90°
2	52	43°
3	50	90°
4	13	40°
5	29	30°
6	20	85°
7	50	--

Figure 2. Schematic of the Input and Output Matching Networks

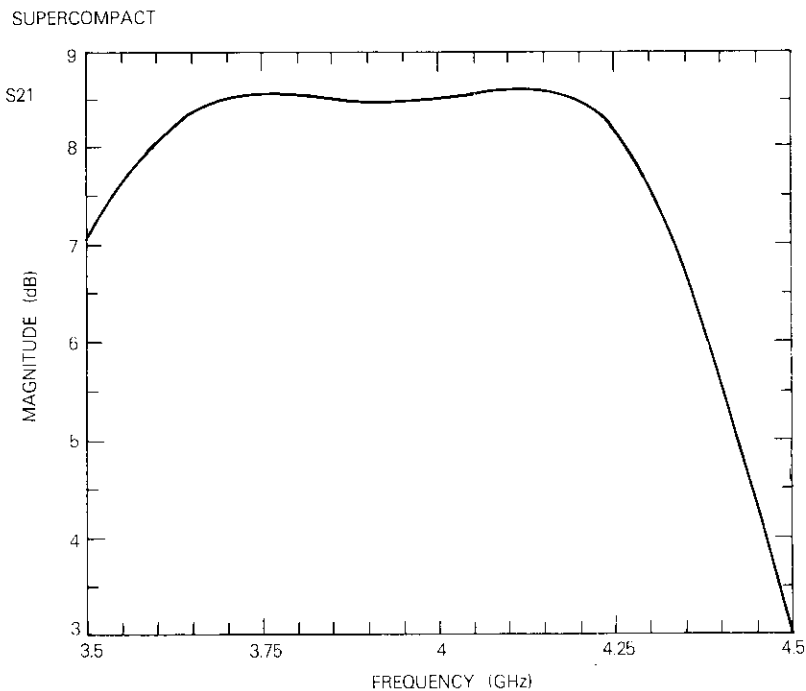


Figure 3. Example of Computed Prediction of Small Signal Gain-Frequency Response

Input and output circuits were then realized in a microstrip transmission line on 25-mil-thick alumina substrates. The device was mounted on the metal ridge of a substrate carrier between the input and output circuits to provide a good heat sink. After small signal tuning, a fairly constant gain of 8.6 ± 0.25 dB was measured for frequencies from 3.6 to 4.3 GHz. As the input drive level was increased, gain compression was observed. At a selected high input power level (the intended operating level), additional tuning was performed on the output matching circuit. Broadband transfer characteristics, minimized intermodulation, and maximized output power were simultaneously maintained. Tuning was completed by adding a small stub in the output matching network, indicated in Figure 2 as the region enclosed by dashed lines. This final tuning had very little effect on bandwidth. Any small gain deviation resulting from tuning for optimum load impedance was easily compensated by slightly readjusting the input network stub.

When higher power is required, it is necessary to combine several output modules in parallel. Figure 4 is a photograph of a balanced amplifier using two low-loss (0.1 dB per pass) Lange hybrids for power dividing and recombining.

Amplifier performance

Six single-ended amplifier modules were fabricated, tuned, and tested. Two are high-gain, 17.5-percent bandwidth design, and the other four are lower gain, 25-percent bandwidth design. The performance characteristics of each design indicate excellent repeatability if the same type packaged FETs are employed.

For the higher gain modules, a typical gain-frequency response is shown in Figure 5 for three different input power levels. (The voltage between the drain and the source, V_{ds} , was 10 V.) The 0.5-dB bandwidth is 700 MHz (3.6 to 4.3 GHz). The output power and the corresponding power-added efficiency vs input power of this module at 4 GHz is shown in Figure 6. At the maximum efficiency of 48.6 percent, the amplifier produces 6-dB gain and 3.23-W output power. Figure 7 displays the relationship between output power, power-added efficiency, and drain current. For different output power levels, the amplifier can be operated at a bias condition selected for maximum efficiency.

A broadband power combined amplifier module, using Lange hybrids, was fabricated and tested. The measured gain-frequency responses of

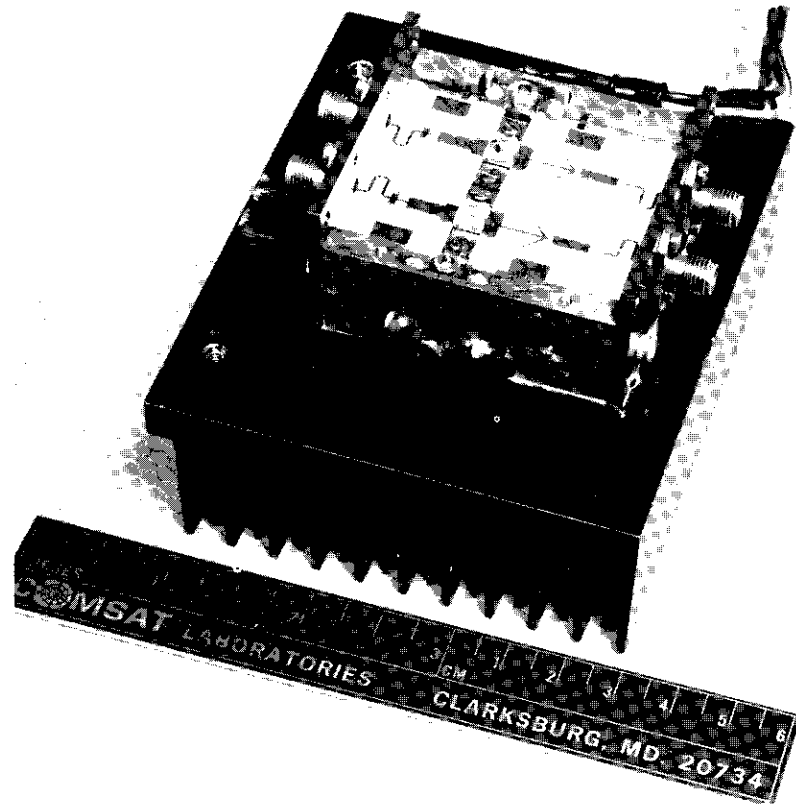


Figure 4. *Balanced Amplifier Module*

three input power levels are shown in Figure 8. The 0.5-dB bandwidth is 900 MHz with 6.6-dB small signal gain. Figure 9 displays output power, efficiency, and intermodulation vs input power at 4 GHz. The third-order intermodulation products were measured with the conventional two-signal method. The injected carriers were equal in power and 5 MHz apart in frequency. The amplifier module delivers 5-W RF power at the maximum efficiency of 36 percent. Typical phase variations vs input drive level are shown in Figure 10.

Table 1 summarizes the performance characteristics of two single-ended amplifiers and one balanced amplifier.

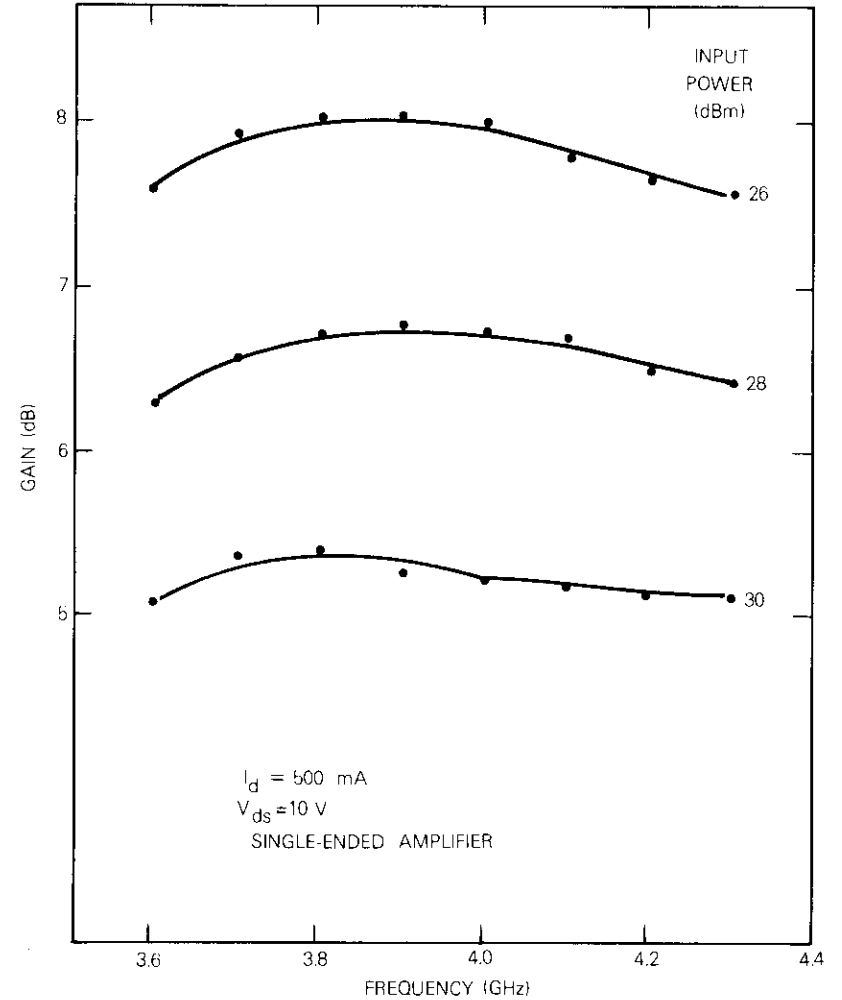


Figure 5. *Measured Frequency Response of Single-Ended Amplifier*

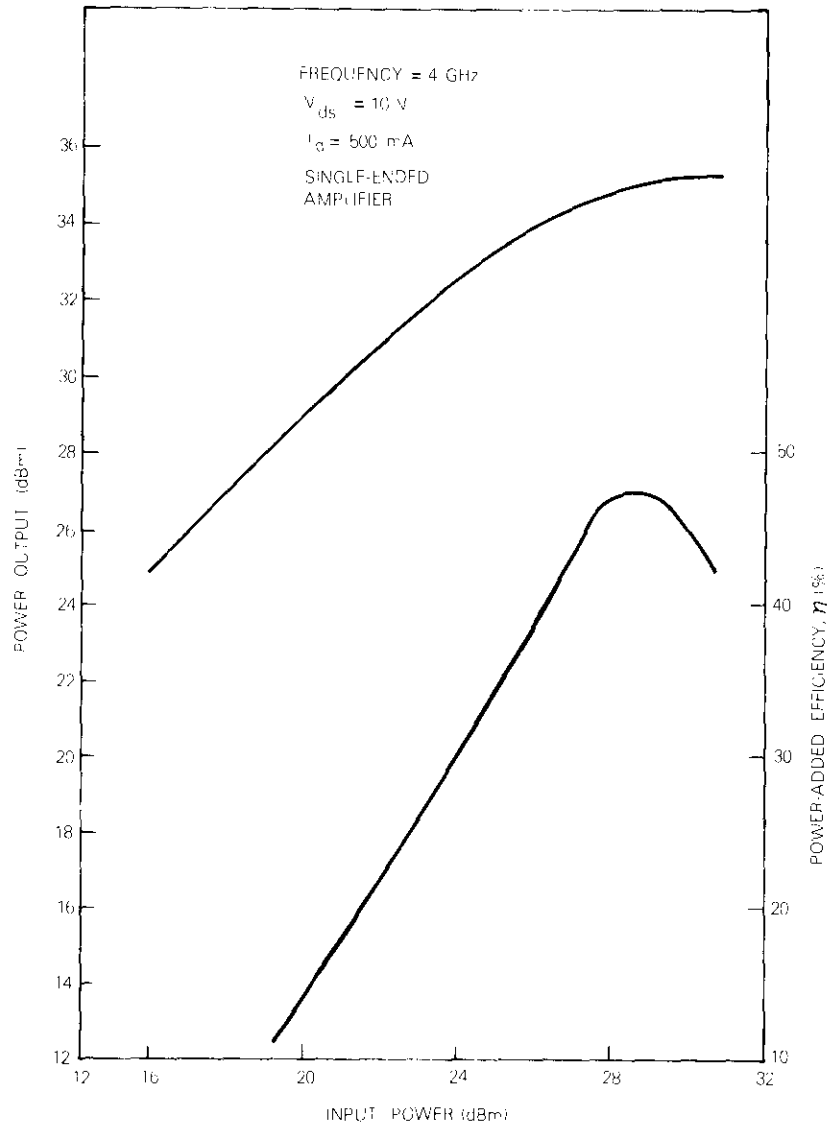


Figure 6. Output Power and Power-Added Efficiency vs Input Power of Single-Ended Amplifier at 4 GHz

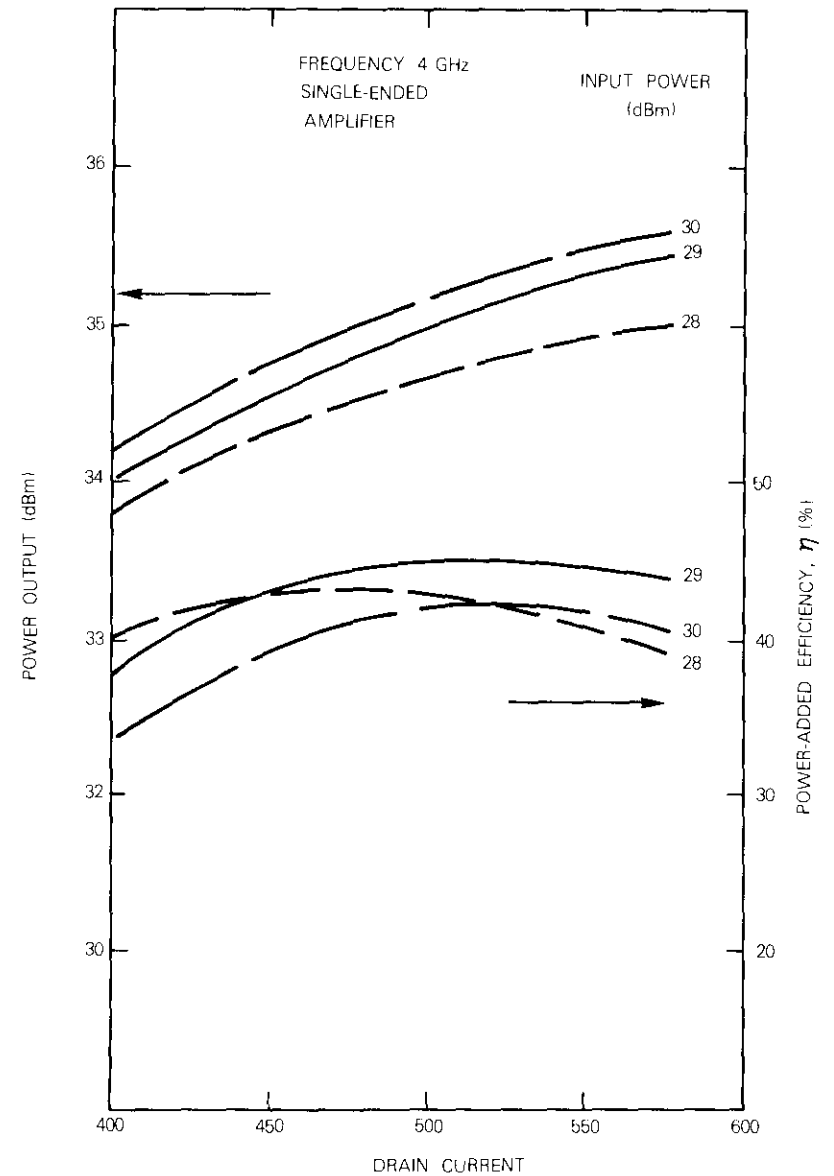


Figure 7. Output Power and Efficiency vs FET Drain Current of Single-Ended Amplifier at 4 GHz

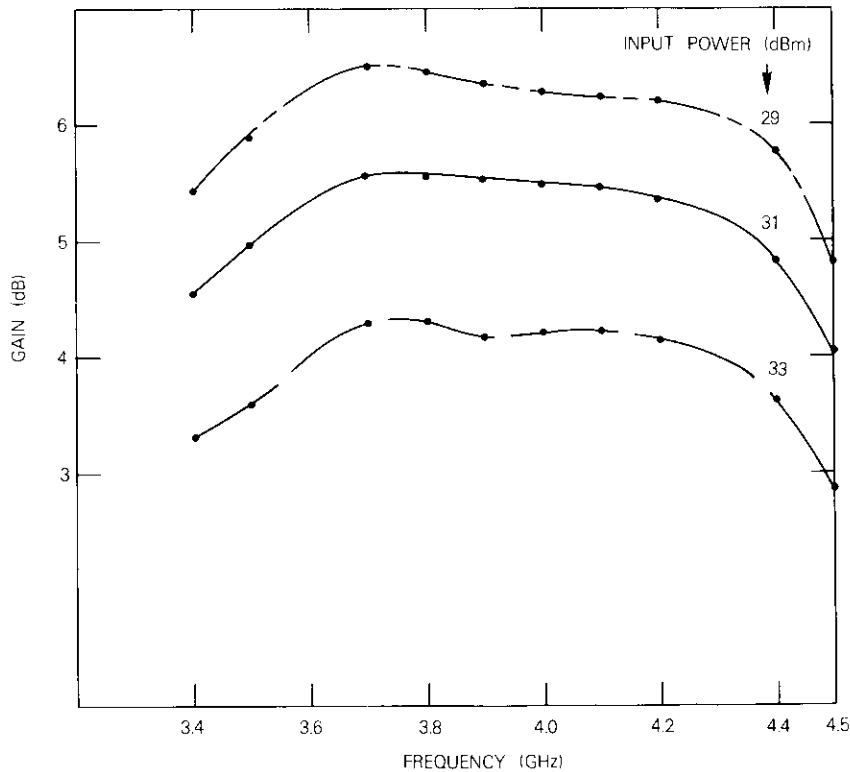


Figure 8. Measured Frequency Response of Balanced Amplifier

Conclusions

Improved bandwidth and efficiency have been achieved in the development of GaAs multicell FET amplifiers. High-performance single-ended and balanced amplifiers can be used as building blocks for an SSPA, which could serve as a desirable replacement for TWTAs. The design approach used in this work has proved to be simple and adequate.

Acknowledgments

The authors wish to thank C. Mahle, F. Assal, W. Getsinger, R. Mott, and A. Berman for their assistance and encouragement; R. Kessler for his enthusiastic support; and M. Urcuyo for assembling the FET amplifier.

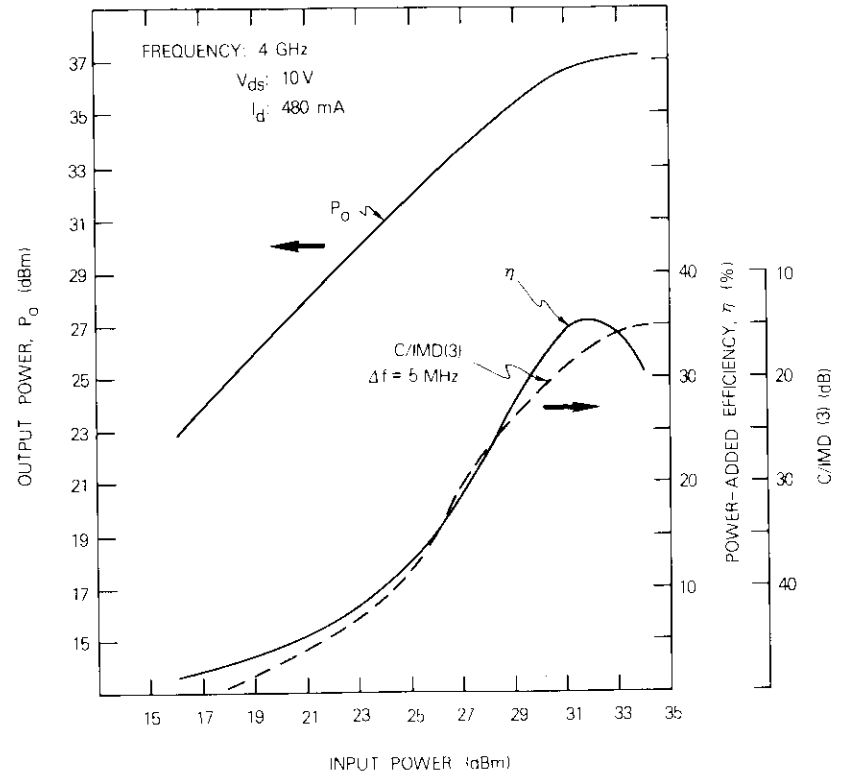


Figure 9. Output Power, Efficiency, and Intermodulation [C/IMD(3)] vs Input Power of Balanced Amplifier at 4 GHz

References

- [1] F. Sechi, H. Huang, and V. Riginos, "High Efficiency MESFET Linear Amplifier Operations at 4 GHz," *Digest of Technical Papers, IEEE International Solid State Circuits Conference*, 1977, pp. 164-165.
- [2] P. T. Ho, "A CWC-Band FET Amplifier Using Serial Power Combining Techniques," *MIT Microwave Symposium Digest*, 1978, pp. 142-144.
- [3] Y. Arai, S. Muri, and T. Sakane, "High Power GaAs FET Amplifier for TWT Replacement," *Fujitsu Scientific and Technical Journal*, Vol. 15, No. 3, September 1979, pp. 63-92.

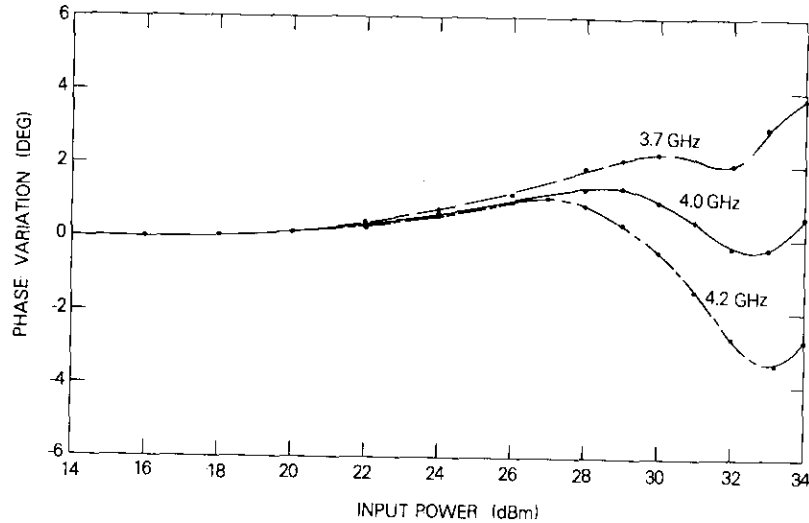


Figure 10. Phase Characteristics of Balanced Amplifier

- [4] B. Geller and F. Assal, "Impact of MMIC Development on Communications Satellites," *Proceedings, International Conference on Communications, 1982*, pp. IE.1.1-IE.1.5.
- [5] S. Chou, C. Chang, and F. Assal, "High Efficiency Broadband FET Power Amplifier for C-Band TWTA Replacement," *Proceedings, International Conference on Communications, 1982*, pp. IE.2.1-IE.2.4.

TABLE 1. PERFORMANCE CHARACTERISTICS OF TWO SINGLE-ENDED AMPLIFIERS AND ONE BALANCED AMPLIFIER*

CHARACTERISTIC	SINGLE-ENDED AMPLIFIERS		BALANCED AMPLIFIER
	MODULE A	MODULE B	
Bandwidth (MHz)	1,000	700	900
Frequency (GHz)	3.4-4.4	3.6-4.3	3.5-4.4
Small Signal Gain (dB)	7.0 ± 0.2	8.6 ± 0.25	6.71 ± 0.25
Output Power (1-dB compression point) (dBm/W)	33.5/2.24	34.2/2.63	36.2/4.17
Maximum Output Power (dBm/W)	34.77/3.0	35.2/3.31	37.4/~5.5
Power-added Efficiency (percent)	40.5	48.6	36
Output Power at Maximum Efficiency (dBm/W)	34.5/2.82	35.1/3.24	36.95/4.95

*Fujitsu FLC30 FET used in single-ended amplifier; two FLC30 FETS used in balanced amplifier.

Summary of INTELSAT VI communications performance specifications

A. GH AIS, J. MARTIN, D. ARNSTEIN, AND H. LEWIS

Introduction

This note outlines significant technical parameters specified for the INTELSAT VI spacecraft presently under construction at the Hughes Aircraft Company. Characteristics relating to the potential use of the payload are emphasized and other aspects of the spacecraft are also briefly described.

A previous CTR paper [1] described the INTELSAT V satellite communications and payload characteristics. A broad overview of INTELSAT operations and planning including a description of many of the INTELSAT VI characteristics was presented in Reference 2. More recently, a paper on the technology innovations for INTELSAT VI appeared [3], which described the capability of succeeding generations of INTELSAT satellites.

General characteristics of INTELSAT VI spacecraft

INTELSAT VI (see Figure 1 for on-orbit configuration) will be a spin-stabilized, active repeater communications satellite for use in geosynchronous equatorial orbit. The spacecraft will have a capacity of approximately 80,000 one-way telephone channels plus two television channels.

A. Ghais is Director, Satellite Communications Systems, World Systems Division; J. Martin is a Spacecraft Consulting Engineer; D. Arnstein is Manager, Communications Systems Analysis; and H. Lewis is a Systems Coordination Analyst.

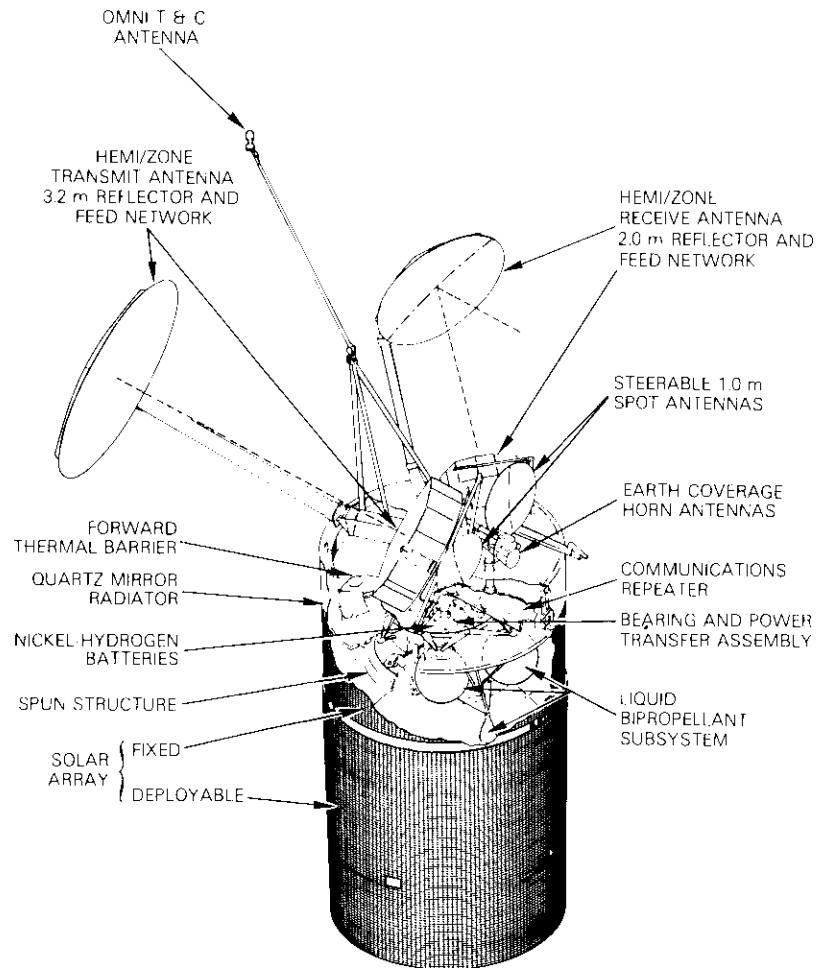


Figure 1. *On-Orbit Configuration*

A single satellite design will be employed to satisfy INTELSAT communications requirements in the Atlantic, Pacific, and Indian Ocean regions. The mass and size of the satellite will permit it to be placed into a synchronous transfer orbit by the Ariane 4 launch vehicle or into low earth parking orbit by the Space Transportation System (STS). For spacecraft launches that use the STS, the contractor will provide all equipment required to transfer the spacecraft from the parking orbit to the desired

synchronous transfer orbit. The mass of the spacecraft and its STS interface support equipment will not exceed 13,772 kg. When the satellite is configured for launch by Ariane 4, its mass plus that of the flight adapter will not exceed 3,740 kg.

The spacecraft is to be designed to meet all specification requirements without interruptions for 10 years in orbit. Accordingly, nickel-hydrogen batteries will be the energy storage device for supplying power to the spacecraft during an eclipse. The batteries will be sized to support the spacecraft during ground testing and through the launch sequence until the solar array is able to support the spacecraft bus, and subsequently, through the biannual eclipse season for the design life of the spacecraft. After 10 years in orbit, the predicted power output of the solar array in the worst-case conditions of distribution losses, battery charging, thermal control, motor drive variations, operation of all transponders in worst-case power modes, etc., will be at least 110 percent of the load requirement. This is in addition to a 5-percent design load margin which is allowed to decrease to zero when the actual loads are known by measurement.

Sufficient propellant will be provided to satisfy the translation velocity and rotational impulse required by the spacecraft to attain initial geostationary orbit and during the entire in-orbit operation.

The rotational position of the despun platform will be determined to an accuracy better than 0.02° within 3 hours of continuous observation. It is expected that orbit control maneuvers will be performed to keep the spacecraft longitude within $\pm 0.1^\circ$ of its assigned orbital location and the plane of its orbit within $\pm 0.1^\circ$ of the equatorial plane.

Reliability requirements more stringent than those of previous generations of spacecraft have been imposed on INTELSAT VI to ensure continuous availability throughout its lifetime. Specifications require the probability of survival for the complete spacecraft to be at least 0.99 after 2 months, with more than 65 percent of the RF channels operational in each coverage area. It must be higher than 0.75 after 7 years in orbit, and greater than 0.63 after 10 years, including eclipse operation. Any part, subassembly, or assembly (except the propulsion stages) which, upon failure, can cause loss of one or more of the RF channels in any coverage area, will have an estimated probability of survival of 0.99 or greater. If the 10-year estimate of such an item is less than 0.99, a redundancy or alternative operational mode will be incorporated into the system. Spacecraft items which are subject to known wearout or deterioration will be designed, fabricated, and selected to attain the performance life requirement. Their mean design life for operation in orbit will be at least 15 years,

and the probability of failure due to wearout before 7 years must be less than 1 percent; for 10 years, it must be less than 10 percent.

In the multiple-access mode, the satellite will be capable of connecting many earth station pairs simultaneously. Possible types of transmission modes are as follows:

- a. analog transmission, such as FDM/FM/FDMA voice and FM monochrome or color television;
- b. digital transmission, such as PCM/QPSK/TDMA and SCPC/QPSK/FDMA;
- c. combinations of any of the above transmission modes.

The frequency bands used by this satellite will be at 6 and 14 GHz (up-link receive) and at 4 and 11 GHz (down-link transmit). Frequency reuse through beam isolation and orthogonal polarization will be employed at 6/4 and 14/11 GHz.

Beam coverages, channelization, and connectivity requirements

One of the most prominent features of INTELSAT VI is its sixfold use of part of the 6/4-GHz frequency band through orthogonal circular polarization between co-frequency beams in the same coverage areas, and spatial beam isolation between eastern and western hemisphere beams. The specification also calls for twofold use of a part of the 6/4-GHz bands by employing orthogonal circular polarization in the global beams, twofold reuse in part of the "new" WARC bands using spatial isolation, and twofold use of the 14/11-GHz frequency band through spatial isolation and orthogonal linear polarization.

The spacecraft will have a useful bandwidth of 3,200 MHz. Two 150-MHz, six 72-MHz, and two 77-MHz channels are assigned to 14/11 GHz. Twenty-six 72-MHz, two 41-MHz, and a maximum of ten 36-MHz channels are assigned to 6/4 GHz. Four of the 6/4-GHz, 36-MHz channels, as well as the two 41-MHz channels, provide permanent global coverage. Additional bandwidth of up to 72 MHz may be switched to global coverage. Finally, considering the availability of the hemi, zone, spot, and global (both polarizations) coverages, up to 1,389 MHz of bandwidth can be assigned to earth stations in the geographic areas of highest traffic density.

A broad definition of required payload capabilities can be determined from the specification requirements for beam coverages, transponder channelization, and interconnectivity. These requirements generally define a spacecraft concept and allow for a preliminary evaluation of its

potential applications and use. The following subsections address each of these topics.

FREQUENCY BANDS AND BEAM COVERAGES

The INTELSAT VI baseline spacecraft communications subsystem operates in two frequency band pairs: 6/4 GHz (5,850–6,425 MHz up-link and 3,625–4,200 down-link) and 14/11 GHz (14,000–14,500 up-link, and 10,950–11,200 and 11,450–11,700 down-link). These bands provide 10 distinct coverage areas, eight at 6/4 GHz and two at 14/11 GHz. Table 1 summarizes the coverages and their associated polarizations. Figures 2 through 4 show the 6/4-GHz coverage areas for the three ocean regions. The specific beam requirements differ according to the region in which the spacecraft is used, and coverages are specified in terms of a set of earth station locations. The coverages can be switched from those appropriate for one ocean region to another by ground command.

As shown in Figure 5, at 14/11 GHz, transmit and receive beam coverage requirements in the East are represented by an elliptical area with a major axis of 2.8° and a minor axis of 1.4° (minor axis inclined 22.9° clockwise from true north), as seen from the satellite. Coverage requirements in the West are represented by a circular area of diameter of 1.3° in satellite coordinates. Both beams will be steerable

TABLE 1. INTELSAT VI COVERAGE BEAMS AND POLARIZATION PERFORMANCE

FREQUENCY BAND (GHz)	COVERAGE	POLARIZATION	
		UP-LINK	DOWN-LINK
6/4 ^a	Global A	LHC ^b	RHC ^b
	Global B	RHC	LHC
	West Hemispheric	LHC	RHC
	East Hemispheric	LHC	RHC
	Zone 1	RHC	LHC
	Zone 2	RHC	LHC
	Zone 3	RHC	LHC
	Zone 4	RHC	LHC
14/11	East Spot	Linear ^c	Linear
	West Spot	Linear	Linear

^aPolarization Performance (voltage axial ratio for transmit and receive beams) is ≤ 1.05 , global; and ≤ 1.09 , hemispheric and zone.

^bLHC is left-hand circular, and RHC, right-hand circular.

^cThe polarization of the east spot coverage will be orthogonal to that of the west spot coverage.

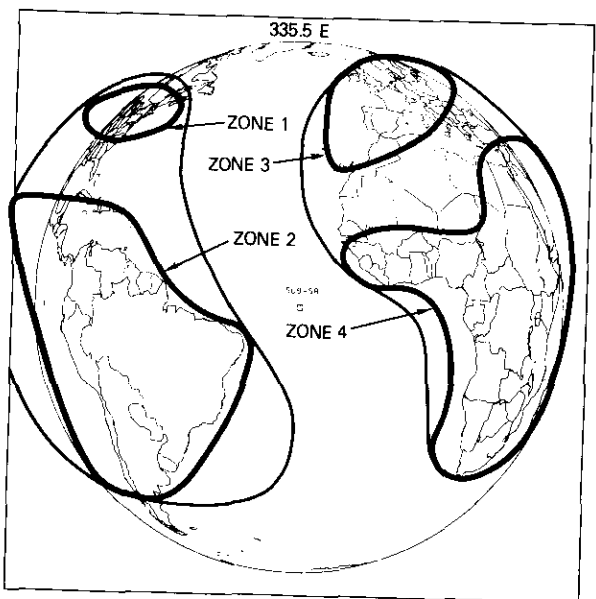


Figure 2. INTELSAT VI Hemi and Zone Antenna Coverage Contours for the AOR from Primary Satellite Location

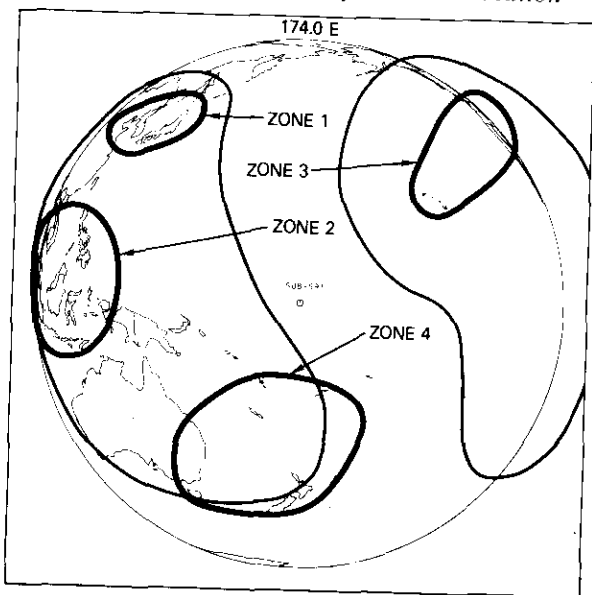


Figure 3. INTELSAT VI Hemi and Zone Antenna Coverage Contours for the POR from Primary Satellite Location

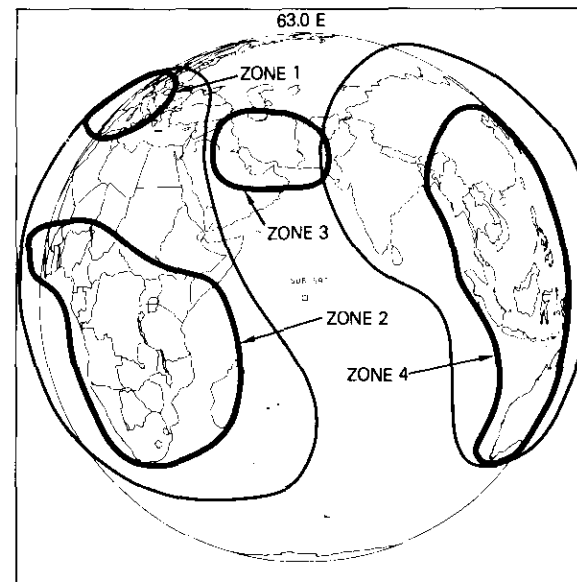


Figure 4. INTELSAT VI Hemi and Zone Antenna Coverage Contours for the IOR from Primary Satellite Location

by ground command and controllable with a resolution of 0.01° or less. They will have a full range of steerability over the earth disc. The east spot beam will be required to meet operational specifications over the entire range of steerability, whereas the performance of the west spot beam will be allowed to degrade below the specified levels when the beam is pointed toward the eastern half of the globe.

TRANSPONDER CHANNELIZATION PLAN

The required interconnections of the receive coverage areas to the transmit coverage areas are accomplished at the transmission channel level. A transmission channel is established by connecting a receiver accessible from one of the reception coverage areas at either 6 or 14 GHz to transmitters associated with the same or any other transmission coverage area at either 4 or 11 GHz. A transmission channel is defined by its bandwidth and allocation as shown in the transponder channelization plan of Figure 6. Each 500-MHz frequency band is subdivided into 12 nominal 40-MHz segments numbered from 1 through 12. When a

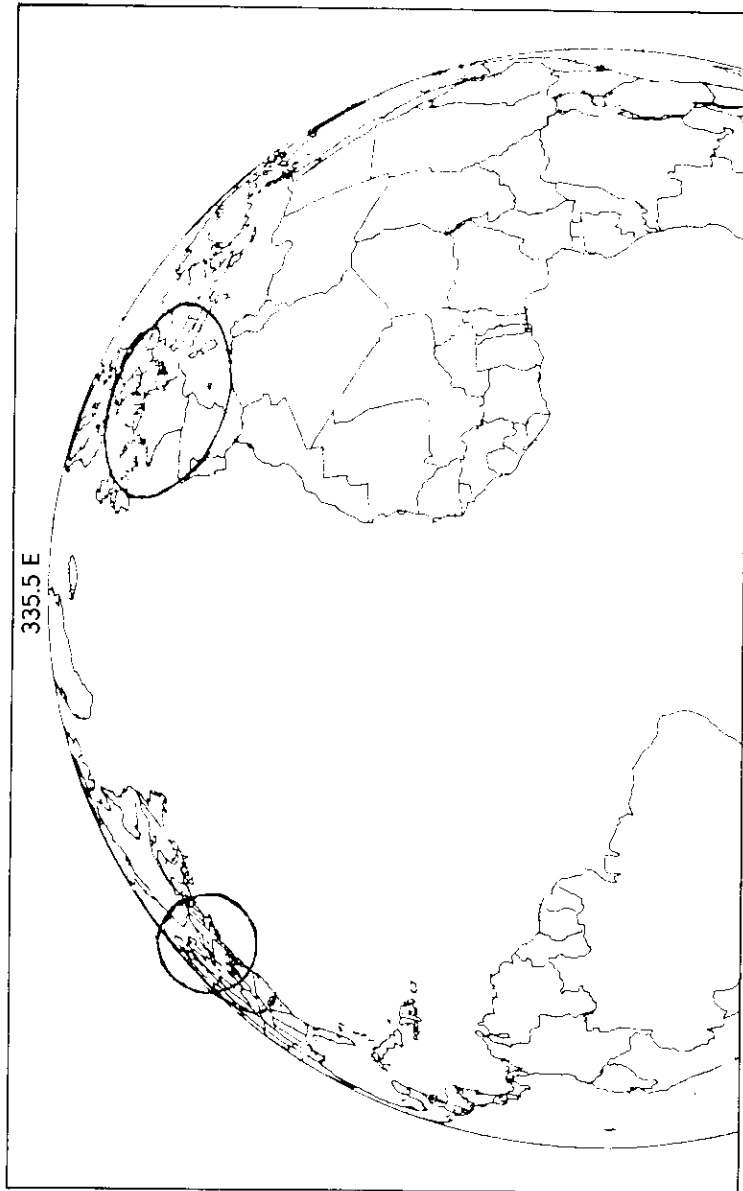


Figure 5. INTELSAT VI 14/11-GHz Antenna Coverage Contours in the AOR from Primary Satellite Location

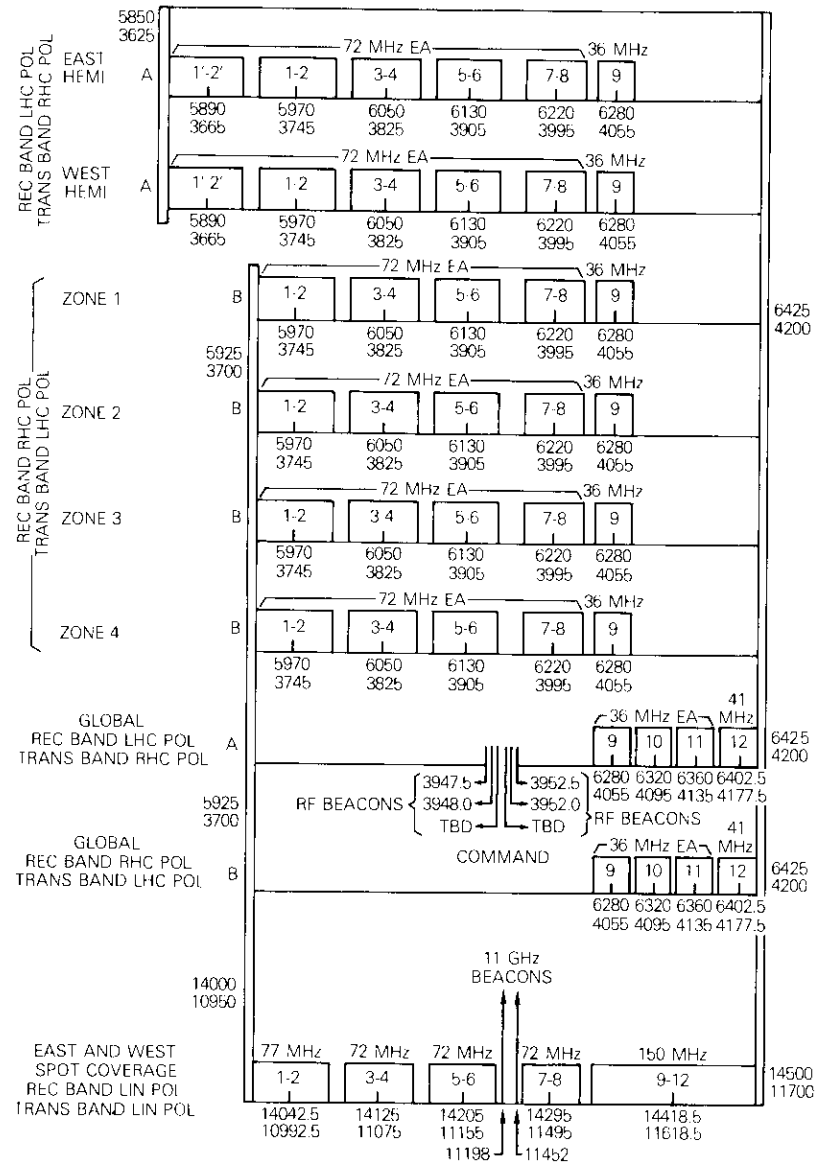


Figure 6. Transponder Center Frequencies, Bandwidths, and Polarization for INTELSAT VI

channel extends over more than one of these segments, it is indicated by a multiple channel number, for example, channel (1-2) or channel (9-12). With the use of the new frequency bands allocated by WARC 1979 on a worldwide basis, this channel numbering scheme proved inadequate. Thus, the transponders in the new frequency bands have been numbered with the prime notation (channel 1'-2') to distinguish them from the transponders in the pre-1979 WARC bands.

TRANSPONDER CONNECTIVITY

Static and dynamic interconnection capabilities will be provided to achieve the required signal paths from the receive to the transmit coverages. A means of achieving these interconnections is illustrated by the signal flow diagram of Figure 7. As shown, a $K \times K$ switch can provide all combinations of input and output interconnections by ground command.

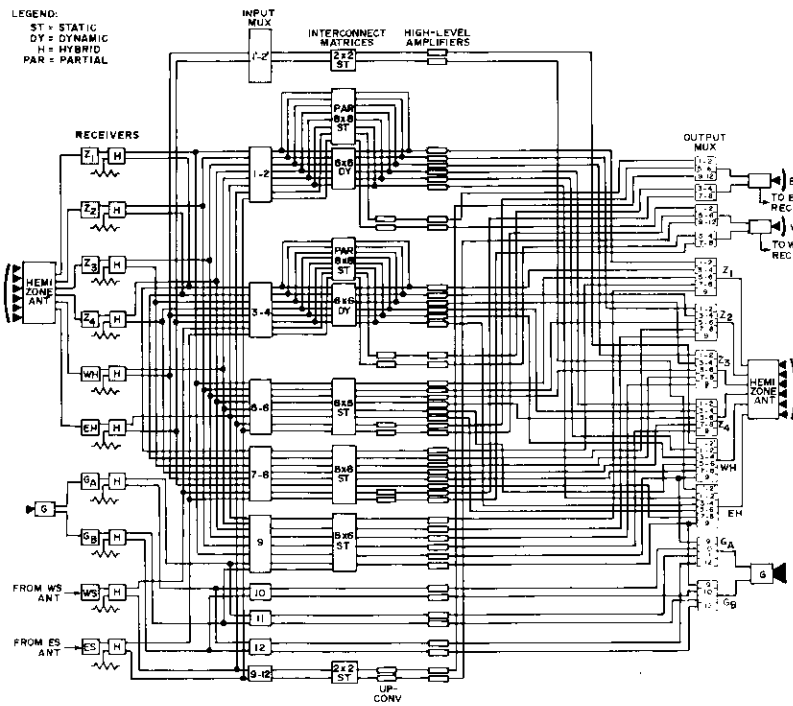


Figure 7. INTELSAT VI Simplified Signal Flow Diagram

In all cases, each input will be connected to only one output. The only exception is in channel (1'-2'), where the up-link in one hemispheric beam may be connected to the down-links in both hemispheric transponders. Static interconnections will remain fixed for relatively long periods until changed by a new set of ground commands. It will be possible, for instance, to establish the static interconnections shown in Table 2.

Dynamic interconnections to support SS-TDMA operation will be established by a dynamic switch and will vary cyclically according to a controllable sequence over a 2-ms period. The interconnection requirements for

TABLE 2. STATIC INTERCONNECTION REQUIREMENTS

RECEPTION COVERAGE	VIA CHANNEL NUMBERS	TRANSMISSION	
		COVERAGE	FREQUENCY BAND (GHz)
6-GHz Frequency Band			
Global A	(9), (10), (11), (12)	Global A	4
Global B	(9), (10), (11), (12)	Global B	4
East Hemi	(1'-2'), (1-2), (3-4), (5-6), (7-8), (9)	East or West Hemi	4
East Hemi	(1-2), (3-4), (5-6), (7-8)	East or West Spot	11
East Hemi	(1-2), (3-4), (5-6), (7-8), (9)	Zone 1, 2, 3, or 4	4
West Hemi	(1'-2'), (1-2), (3-4), (5-6), (7-8), (9)	East or West Hemi	4
West Hemi	(1-2), (3-4), (5-6), (7-8)	East or West Spot	11
West Hemi	(1-2), (3-4), (5-6), (7-8), (9)	Zone 1, 2, 3, or 4	4
Zone 1	(1-2), (3-4), (5-6), (7-8), (9)	East or West Hemi	4
Zone 1	(1-2), (3-4), (5-6), (7-8), (9)	Zone 1, 2, 3, or 4	4
Zone 1	(5-6), (7-8)	East or West Spot	11
Zone 2	(1-2), (3-4), (5-6), (7-8), (9)	East or West Hemi	4
Zone 2	(1-2), (3-4), (5-6), (7-8), (9)	Zone 1, 2, 3, or 4	4
Zone 2	(5-6), (7-8)	East or West Spot	11
Zone 3	(1-2), (3-4), (5-6), (7-8), (9)	East or West Hemi	4
Zone 3	(1-2), (3-4), (5-6), (7-8), (9)	Zone 1, 2, 3, or 4	4
Zone 3	(5-6), (7-8)	East or West Spot	11
Zone 4	(1-2), (3-4), (5-6), (7-8), (9)	East or West Hemi	4
Zone 4	(1-2), (3-4), (5-6), (7-8), (9)	Zone 1, 2, 3, or 4	4
Zone 4	(5-6), (7-8)	East or West Spot	11
14-GHz Frequency Band			
East Spot	(1-2), (3-4), (5-6), (7-8), (9-12)	East or West Spot	11
East Spot	(1-2), (3-4), (5-6), (7-8)	East or West Hemi	4
East Spot	(5-6), (7-8)	Zone 1, 2, 3, or 4	4
West Spot	(1-2), (3-4), (5-6), (7-8), (9-12)	East or West Spot	11
West Spot	(1-2), (3-4), (5-6), (7-8)	East or West Hemi	4
West Spot	(5-6), (7-8)	Zone 1, 2, 3, or 4	4

the dynamic switch are applicable to channels (1-2) and (3-4) at 6/4 GHz only and are shown in Table 3.

Overall communications performance requirements

The performance requirements summarized in this section apply to each transmission channel, including receive antennas, receivers, high-level amplifiers, and transmit antennas. The specified requirements will permit the use of any of the allowed transmission modes and can be conveniently grouped into three categories: link performance, linearity characteristics, and miscellaneous.

LINK PERFORMANCE PARAMETERS

The primary performance parameters of the communications subsystem are given in Table 4 and the antenna beam isolation in Table 5. Together they determine the link power budgets and the associated communication capacities for the various operational modes.

TABLE 3. DYNAMIC INTERCONNECTION REQUIREMENTS

RECEPTION AT 6 GHz COVERAGE	VIA CHANNEL NUMBERS	TRANSMISSION AT 4 GHz COVERAGE
East Hemi	(1-2), (3-4)	East or West Hemi Zone 1, 2, 3, or 4 Broadcast, 2 to 6 Beams
West Hemi	(1-2), (3-4)	East or West Hemi Zone 1, 2, 3, or 4 Broadcast, 2 to 6 Beams
Zone 1	(1-2), (3-4)	East or West Hemi Zone 1, 2, 3, or 4 Broadcast, 2 to 6 Beams
Zone 2	(1-2), (3-4)	East or West Hemi Zone 1, 2, 3, or 4 Broadcast, 2 to 6 Beams
Zone 3	(1-2), (3-4)	East or West Hemi Zone 1, 2, 3, or 4 Broadcast, 2 to 6 Beams
Zone 4	(1-2), (3-4)	East or West Hemi Zone 1, 2, 3, or 4 Broadcast, 2 to 6 Beams

TABLE 4. PRIMARY PERFORMANCE PARAMETERS OF COMMUNICATIONS SUBSYSTEMS

a. Receive System G/T (dB/K)			
	Extra High Gain	High Gain	Low Gain
6 GHz			
Global	-14.0	-14.0	-14.0
Hemispheric	-9.2	-9.2	-9.5
North Zones	-2.0	-2.0	-3.0
South Zones	-7.0	-7.0	-7.5
14 GHz			
East Spot	+1.0	+1.0	+1.0
West Spot	+5.0	+5.0	+5.0
b. e.i.r.p. (dBW)			
	Channel 9	Other Channels	
4 GHz			
Global	23.5	26.5	
Hemispheric or Zone	28.0	31.0	
11 GHz			
East Spot	41.1		
West Spot	44.4		
c. Saturation Flux Density (dBW/m ²)			
	Extra High Gain	High Gain	Low Gain
Up-Link Beam			
6 GHz			
Channels 1-8	-82.1	-77.6	-67.1
Channels 9-12	-82.1	-77.6	-70.1
14 GHz			
East Spot/All Channels	-84.0	-78.0	-73.0
West Spot/All Channels	-87.3	-81.3	-76.3

NONLINEAR CHANNEL PERFORMANCE

The specifications applying to the input sections common to more than one transmission channel are summarized in Table 6, and those applicable to the individual transmission channels are summarized in Table 7. In both cases, the maximum total phase shift, minimum intelligible cross-talk ratio, and minimum carrier to intermodulation (C/I) ratio have been specified as functions of the illumination flux density. In addition, the

TABLE 5. TRANSMIT AND RECEIVE ANTENNA BEAM ISOLATION (dB)

11- and 14-GHz Spot Beams						
Angle Between Beam Centers (θ)						Isolation (dB)
$8.0^\circ \leq \theta$						33
$6.5^\circ < \theta < 8.0^\circ$						27
$3.5^\circ \leq \theta \leq 6.5^\circ$						25
4- and 6-GHz Hemi and Zone Beams						
	Z1	Z2	Z3	Z4	EH	WH
Atlantic Ocean Region						
Z1	—	27	27	30	30	27
Z2	27	—	30	27	30	27
Z3	27	30	—	27	27	30
Z4	30	27	27	—	27	30
EH	30	30	27	27	—	27
WH	27	27	30	30	27	—
Indian Ocean Region						
Z1	—	27	27	30	30	27
Z2	27	—	27	30	30	27
Z3	27	27	—	27	27	27
Z4	30	30	27	—	27	30
EH	30	30	27	27	—	27
WH	27	27	27	30	27	—
Pacific Ocean Region						
Z1	—	27	30	30	30	27
Z2	27	—	30	27	30	27
Z3	30	30	—	30	27	30
Z4	30	27	30	—	27	27
EH	30	30	27	27	—	27
WH	27	27	30	27	27	—
4- and 6-GHz Global Beams						
Coverages						Isolation (dB)
Global A to Global B						32

maximum allowable AM-to-PM (AM/PM) transfer coefficient has been specified for each transmission channel.

ADDITIONAL MISCELLANEOUS SPECIFICATIONS

In addition to the communications parameters included in the above categories, the performance characteristics summarized in Table 8 are of general interest; they are essential to the operation of the INTELSAT VI communications payload.

TABLE 6. NONLINEAR PERFORMANCE SPECIFICATIONS APPLICABLE TO INPUT SECTIONS COMMON TO MORE THAN ONE TRANSMISSION CHANNEL

a. Single-Carrier Performance			
Flux Density Illuminating Spacecraft (dBW/m ²)		Total Phase Shift (deg)	Intelligible Crosstalk Ratio (dB)
6 GHz	14 GHz		
-62.6	-68.5	1.5	-175 + 20 log f_m^*
-71.6	-77.5	0.2	-193 + 20 log f_m^*
b. Two-Carrier Performance			
Flux Density Illuminating the Spacecraft with two Equal Amplitude Carriers (dBW/m ²)			C/I (dB)
6 GHz	14 GHz		
-65.6	-71.5		26
-70.6	-76.5		36
-75.6	-81.5		46

*The modulating frequency, f_m , is expressed in Hz.

TABLE 7. NONLINEAR PERFORMANCE SPECIFICATIONS APPLICABLE TO EACH TRANSMISSION CHANNEL

a. Phase Linearity of Each Transmission Channel				
Relative Flux Density ^a (dB)	Output Transmission Phase Shift (deg)		AM/PM Transfer Coefficient (deg/dB)	
	TWTA	SSPA	TWTA	SSPA
0	46	20	8.0	2.0
-3	38	14	9.0	2.0
-6	28	7	9.0	2.0
-9	18	3	8.0	2.0
-12	12	1	5.0	1.0
-14	9	1	3.0	1.0
<-14	—	—	3.0	1.0

b. Intelligible Crosstalk Ratio^b

Relative Flux Density (dB)	Channel Bandwidth (MHz)	Location of Modulated Carrier Center Frequency ^c	
		Within the Center 70% of the Usable Bandwidth	Over 100% of Usable Bandwidth
0 to -14	36, 41	-171 + 20 log f_m	-149 + 20 log f_m
<-14		-177 + 20 log f_m	-155 + 20 log f_m
0 to -14	72, 77, 150	-173 + 20 log f_m	-151 + 20 log f_m
<-14		-179 + 20 log f_m	-157 + 20 log f_m

(continued)

TABLE 7. NONLINEAR PERFORMANCE SPECIFICATIONS
APPLICABLE TO EACH TRANSMISSION CHANNEL (continued)

c. Amplitude Linearity			
Relative Flux Density ^d Per Carrier (dB)	Maximum Intermodulation-to-Carrier Ratio ^e (dB)		
	TWTA	SSPA	
- 3.0	-10	-12	
-10.0	-15	-25	
-17.0	-26	-38	

^aFlux density illuminating the spacecraft relative to the flux density which produces single-carrier saturation.

^bThe intelligible crosstalk ratio requirement is 10 dB less than the values indicated for channels using solid-state power amplifiers (SSPA).

^cThe modulation frequency, f_m , is expressed in Hz.

^dFlux density illuminating the spacecraft for each of two equal-amplitude carriers below the flux density which produces single-carrier saturation.

^eMaximum level of third-order intermodulation product relative to the level of each of the RF carriers, measured at the output of each transmission channel.

TABLE 8. ADDITIONAL COMMUNICATIONS
PARAMETER SPECIFICATIONS

Spurious Power Output (in the transmit bands at the input of any transmit antenna)	
In any 1.0-MHz Band	-55 dBW
In any 4.0-kHz Band	-60 dBW
Repeater Isolation	
All Channels	≥ 50.0 dB
Hemispheric and Zones Channels, (1-2) and (3-4), Including the Effects of the Dynamic Switch	≥ 47.0 dB
Long-Term Frequency Stability (GHz)	
Over Lifetime, Including Initial Tolerances and Eclipse Effects	
6/4	± 10 Parts in 10^6
6/11	± 4 Parts in 10^6
14/4	± 2 Parts in 10^6
14/11	± 7 Parts in 10^6
Over 1 Month, Excluding Eclipse Effects	
6/4	± 10 Parts in 10^7
6/11	± 4 Parts in 10^7
14/4	± 2 Parts in 10^7
14/11	± 7 Parts in 10^7

TABLE 8. ADDITIONAL COMMUNICATIONS
PARAMETER SPECIFICATIONS (continued)

Gain Stability (over any day, at the center of each transmission channel)	1 dB Peak-to-Peak
Overdrive Capability (without subsequent degradation of performance or lifetime)	20 dB ^a
Switching Time Outage	< 25 ms ^b
11-GHz Beacons Frequency	
First Beacon	11.198 GHz
Second Beacon	11.452 GHz
Polarization ^c	Voltage Axial Ratio ≤ 1.03
Frequency Stability	3 Parts in 10^6
c.i.r.p.	≥ 6 dBW over Earth Coverage
Stability	
Over any Operating Day	1 dB Peak-to-Peak
Over Operating Lifetime	2 dB Peak-to-Peak

^aAbove the single or multicarrier flux illumination values.

^bThis value will be relaxed to 100 ms for K-band waveguide switches.

^cRight-hand circular.

References

- [1] J. C. Fuenzalida, P. Rivalan, and H. J. Weiss, "Summary of the INTELSAT VI Communications Performance Specifications," *COMSAT Technical Review*, Vol. 7, No. 1, Spring 1977, pp. 311-326.
- [2] E. I. Podraczky and J. L. Dicks, "International System Development," *Innovations in Telecommunications*, Part B, Proceedings of a symposium held in Kuwait in April 1981, sponsored by the Kuwait Foundation for the Advancement of Sciences, J. T. Manassah, Ed., Academic Press, New York, N.Y. 10003, 1982.
- [3] S. B. Bennet and D. J. Braverman, "INTELSAT VI Technology," 33rd Congress of the International Astronautical Federation, September 27-October 2, 1982, Paris, France, sponsored by AIAA, New York, N.Y. 10104.

Translations of Abstracts in this issue

Balayage de faisceau de l'antenne grégorienne à alimentation excentrée

V. KRICHEVSKY ET D. F. DIFONZO

Sommaire

Cet article décrit les solutions analytiques permettant d'obtenir les lieux géométriques des sources à direction constante de faisceau (CBDFL) et le lieu géométrique optimal d'emplacement de source (OFPL) dans le cas des antennes grégoriennes à alimentation excentrée. Une analyse de «mode d'émission» est utilisée pour suivre le parcours des rayonnements de la source vers un réflecteur secondaire ellipsoïdal dont le pourtour limite est défini d'emblée. Le parcours des rayonnements est alors suivi jusqu'au réflecteur principal dont le pourtour limite peut être déterminé après avoir tenu compte des contributions de tous les emplacements de source. Les emplacements optimaux de la source sont définis par le point d'intersection des lieux géométriques des sources à direction constante de faisceau, d'une part, et du lieu géométrique optimal d'emplacement de sources, d'autre part. On a constaté que, dans les cas étudiés, la forme canonique du lieu géométrique optimal d'emplacement de source était une ellipsoïde.

Les solutions sont décrites sous forme d'expressions analytiques; leur rendement est donc supérieur, du point de vue des calculs, à celui d'autres méthodes telles que l'équilibrage des champs de région focale ou l'examen visuel des parcours graphiques des rayonnements dans la région focale. L'analyse sur ordinateur du balayage de faisceau dans le cas de plusieurs configurations grégoriennes types à alimentation excentrée confirme que cette méthode permet d'obtenir les meilleurs emplacements de source des points de vue gain, symétrie de diagrammes, et profondeur du zéro. Les résultats permettent d'évaluer l'application de ce type d'antenne aux satellites de télécommunications et aux stations terriennes à faisceaux multiples.

Dépolarisation des signaux de balise COMSTAR à 19 GHz

PRABHA N. KUMAR

Sommaire

La dépolarisation est l'une des données importantes qu'il faut connaître lors de la conception d'un système de télécommunications faisant appel à la réutilisation des fréquences pour augmenter la capacité en voies du système. La mesure quan-